Università degli Studi della Basilicata

Dottorato di Ricerca in
"Ingegneria per l'innovazione e lo sviluppo sostenibile"

Improving the efficiency of fluid machinery through waste-heat recovery

Settore Scientifico-Disciplinare
"ING-IND/08

Coordinatore del Dottorato:
Prof. Aurelia Sole

Dottorando:
Dott. Antonio Cantiani

Relatore:
Prof. Annarita Viggiano

Correlatore:
Prof. Vinicio Magi
Dott. Emanuele Fanelli

Ciclo XXXIV

Summary

Chapter 1
Introduction

1.1 The role of energy efficiency on climate change mitigation policies

The increasing awareness of the impact of anthropic activities on climate change has led to the instauration of specific policies that aim to reduce greenhouse gases (GHG) emissions and to reach a sustainable economic development. The Kyoto protocol (adopted in 1997) has been the first worldwide joint attempt to limit the GHG emissions and stabilize their level to concentrations that will prevent dangerous interference with the climate system [1]. The reduction targets on GHG set by the Kyoto protocol averaged at about 5.2% for industrialized countries during the first commitment period (2008-2012) [2].

The effects of GHG emissions regulations on the economy should also be carefully considered, since they could lead to an economic decline [3] and an increase in the cost of living, thus increasing the poverty threshold. Furthermore, companies could find it more convenient to import semi-finished products from developing countries, which do not impose GHG mitigation policies, rather than meeting the imposed GHG emissions targets. This effect, which goes under the name of *carbon leakage* [4], would defy the purpose of the GHG mitigation policies, since it would only allow the developed countries to meet their GHG production targets relocating their production to developing countries.

The deep interaction between GHG emissions and economic growth led to the adoption of more sophisticated approaches to mitigate emissions, such as the transition to a circular economy and the improvement of energy efficiency. Both of these concepts rely on the idea of reducing GHG emissions as a consequence of the reduction of waste materials and energy, which will also result in a more sustainable development. The circular economy is opposed to the idea of linear economy, where the lifecycle of a product starts from its production and ends as it is disposed as waste (Figure 1.1), and aims to recycle and reuse products, minimizing the inputs of new resources for their production (Figure 1.2). The concept of circular economy can be applied not only to goods production, but also to processes: for example, the heat deriving from the cooling system of a supercomputer (which is usually in the order of MW [5]) could be used for domestic heating and/or power generation [6]. This practice is usually referred to as

cogeneration and consists in the simultaneous production of mechanical power (often converted into electrical energy) and useful heat.

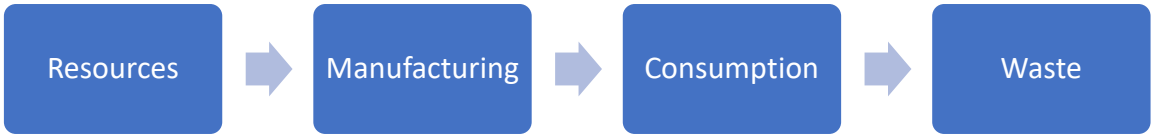

Figure 1.1: Linear economy model.

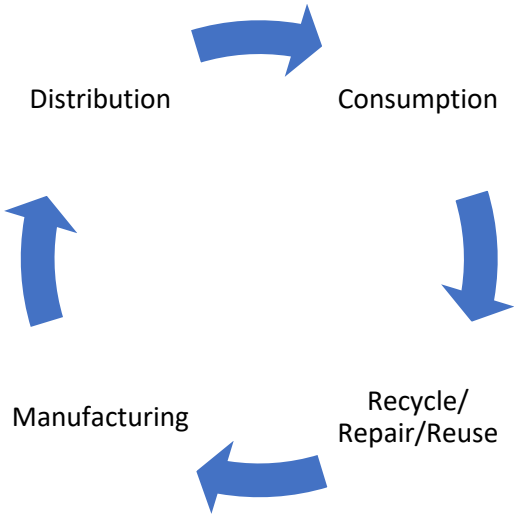

Figure 1.2: Circular economy model.

Improving energy efficiency of anthropic activities aims to reduce energy consumption by reducing energy losses, either increasing the effective energy usage or re-using waste energy. One of the first attempts to improve energy efficiency could be traced back to the European Union's 20-20-20 climate and energy targets. These targets, set in 2007 and enacted in legislation in 2009 [7], aimed to cut GHG emissions by 20% (respect to 1990 levels), to produce 20% of EU energy from renewable sources and to improve energy efficiency by 20% within the year 2020. With the directive 2012/27/EU [8], the European Union highlighted the importance of energy efficiency both to reach the pollutant emissions reduction targets and to boost economic growth. This directive aimed to establish a common framework to promote energy efficiency within the Union to achieve the target of 20% energy efficiency improvement by 2020. The directive is prevalently directed towards efficiency in buildings, since they represent about 40% of the Union's final energy consumption, but also addresses efficiency in energy and goods production plants. In particular, as regards energy production, the directive puts emphasis on the preferential use of high efficiency energy production plants and co-generative plants. According to the directive 2012/27/EU, shifting to a more efficient economy should also accelerate the spread of innovative technological solutions and

improve the competitiveness of the European industry, boosting economic growth and creating high skills jobs in several sectors related to energy efficiency.

The European Union's 20-20-20 climate and energy targets have been replaced by the European Green Deal, which aims to further cut European GHG emissions by at least 55% by 2030 and to become the world first climate-neutral continent by 2050. One of the key elements of the European Green Deal policies is the boosting of energy efficiency, confirming its central role in the future climate change mitigation policies.

We can conclude that current trends in climate change mitigation policies suggest a central role for energy efficiency both in the short and long term. Maximizing the efficiency of a process means reducing to the minimum the amount of resources needed, resulting in a more sustainable economy and a lower environmental impact with minimum influence on social-welfare.

1.2 The efficiency of fluid machinery

Fluid machines are devices that transform energy stored by a fluid into mechanical energy, or vice versa. In general, the efficiency (ε) of a machine is defined as the fraction of energy utilized (E_{ut}) with respect to the energy input (E_{in}) given to the machine, according to the following equation:

$$\varepsilon = \frac{E_{ut}}{E_{in}}. \qquad \text{Eq. (1.1)}$$

Ideally, one would like to completely convert the input energy into useful energy, therefore resulting in unitary efficiency. Experimental evidence has suggested that in the real world it is not possible to build such a machine: not all the energy given as input to a machine can be converted into useful energy. At first glance, this may seem caused by the imperfection of the machine (friction between its moving parts), the fluid (not ideal) and the thermodynamic transformation (non-reversible). *Carnot's theorem* proved that even an ideal machine with no friction, working with an ideal gas and that only performs reversible thermodynamic transformations will have an efficiency lower than unity.

The Carnot cycle, shown in Figure 1.3, consists of two isothermal and two adiabatic reversible transformations. It can be proved that its efficiency (ε_{car}), defined as the work obtained divided by the heat provided to the cycle, only depends on the temperatures of the two isothermal transformations according to the following equation:

$$\varepsilon_{car} = \frac{T_1 - T_2}{T_1}. \qquad \text{Eq. (1.2)}$$

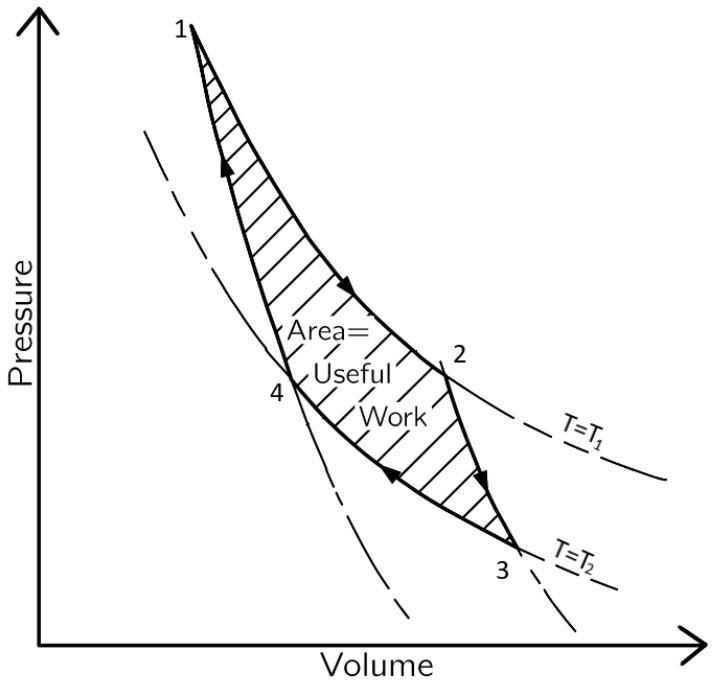

Figure 1.3: The Carnot cycle: 1-2 = isothermal expansion; 2-3 = adiabatic expansion; 3-4 = isothermal compression; 4-1 adiabatic compression. All transformations are reversible.

Since T_1 is greater than T_2, the efficiency of the Carnot cycle is always lower than 1, and it can reach one only if T_2 approaches absolute zero. We can therefore conclude that even an ideal machine cannot fully transform the energy input into work, and a real machine will have an efficiency lower than the Carnot efficiency. The efficiency of energy usage has an upper limit, and even with any future technological development we can only strive towards reaching the Carnot efficiency, not unitary efficiency.

In fluid machines the difference between input energy and energy utilized is usually referred to as energy losses. These energy losses are divided in contributions due to different effects, in order to have a better understanding of their relative importance. If we consider, for example, an internal combustion engine, the energy input is proportional to the fuel mass present into the combustion chamber and the energy utilized is the work output. The energy losses can be categorized as follows:

- *Combustion efficiency (ε_{comb})*: the combustion process of any fuel involves a high number of chemical reactions and intermediate species. For various reasons, a real combustion process will not completely oxidate all the intermediate species, resulting in a lower energy output respect to what would result from an ideal combustion. We can therefore define a combustion efficiency, as the ratio between the heat generated by the real combustion process and the heat that would be generated by an ideal combustion of the same fuel mass. This energy loss would be zero for an ideal combustion process.

- *Cooling losses (Q_{cool})*: the in-chamber temperature increase due to combustion would increase the engine components temperature to values that would lead to components failure. Therefore, in order to work properly, the engine must be kept within a certain temperature range. Thus, a cooling system is needed, which from an energetic point of view, takes energy from the combustion chamber and discharges it into the environment. This energy loss would be zero for an adiabatic engine.

- *Pumping losses (W_{pump})*: during the intake of fresh air, the in-chamber pressure is lower than ambient pressure, due to the pressure drop through the valves. For the same reason, during the exhaust of burned gases, the in-chamber pressure is higher than ambient pressure. Therefore, the engine will perform work on the fluid in order to complete the intake and exhaust processes. This energy loss would be zero if the pressure drop across the valves was zero.

- *Friction (Q_{fric})*: all the engine moving parts (crankshaft, piston, valves, ecc.) will dissipate energy in the form of heat due to friction. This loss would be zero for a frictionless engine.

- *Utilities (Q_{ut})*: in order to work, an engine needs a certain number of supplementary machines, such as a water pump for the cooling system, an oil pump for lubrication, a fuel pump, etc. These machines will partially use the engine work output. This energy loss would be zero for an engine which could work without auxiliary machines.

- *Exhaust gases energy (Q_{exh})*: the exhaust gases will retain part of the energy resulting from combustion, which is then released into the environment.

With these definitions of energy losses, we could calculate the engine efficiency as:

$$\varepsilon = \frac{Q_{comb\_id} * \varepsilon_{comb} - Q_{cool} - W_{pump} - Q_{fric} - Q_{ut} - Q_{ext}}{Q_{comb\_id}}, \qquad \text{Eq. (1.3)}$$

where Q_{comb_id} is the heat released by the ideal combustion. The numerator of Eq. (1.3) represents the work obtained from the engine.

We could, in theory, build an engine where the combustion process is perfect, the engine is adiabatic and the materials can work at any temperature, hence not needing a cooling system, that can perform intake and exhaust with no pressure drops across the valves, where the moving parts are frictionless and needs no utilities to work. Still such an engine would not have unitary efficiency, since the exhaust gases will inevitably carry out part of the combustion energy.

Carnot's theorem sets an upper limit on the efficiency a particular fluid machine can reach. Therefore, in the improvement of fluid machines efficiency we are not aiming to have unitary efficiency, but to reach a value close to Carnot's efficiency. This can be

done by reducing energy losses: in the case of an internal combustion engine one can try to improve combustion efficiency, reduce the cooling losses using specific technologies and materials, reduce the pressure drop across valves, reduce friction between moving parts and reduce the energy used by auxiliary components.

A complementary approach to improve energy efficiency is energy recovery. The idea of energy recovery is to re-use waste energy of a machine, which would otherwise be released into the environment. In the case of an internal combustion engine, it is possible to use the exhaust gases energy as inputs for another machine. A classical approach is to use this energy with a turbocharger, in order to increase the engine intake pressure. More recent approaches use this energy in Stirling engines or Organic Rankine Cycles (ORCs) [9,10].

It is possible to classify energy recovery techniques into two categories:

- *Closed loop energy recovery*: the energy recovered is reintroduced into the same machine and reconverted by the same thermodynamic cycle (for example turbocharged internal combustion engines);

- *Open loop energy recovery:* the energy recovered is used as input energy by a different machine (for example coupling an ORC to an internal combustion engine).

It should be pointed out that, since the energy recovered is at a higher entropy state, the energy recovery efficiency will inevitably be very low.

Fluid machines are present in several sectors, from transportation to buildings heating/cooling, to energy production. The improvement of their efficiency could result in a drastic reduction in GHG gases emissions. The implementation of energy recovery techniques can be a valid approach to improve the overall efficiency of existing machines. In the present thesis, two different energy recovery approaches will be studied, optimized and compared. The first technique is a *closed loop energy recovery* applied to internal combustion engines, through the use of supercritical water direct injection, which aims to recover exhaust gases energy and cooling losses. The second technique is an *open loop energy recovery* using Organic Rankine Cycles.

The present thesis is divided into two parts:

- in the first part the energy recovery approach based on direct supercritical water injection and applied to internal combustion engines is going to be discussed, starting with the description of a quasi-dimensional model of the energy recovery system, which is then used to optimize the injection parameters, both parametrically and by means of a genetic algorithm; subsequently, a CFD model is presented, aiming to understand the jet structure with different injector architectures using the ECFM combustion model; finally, the EDC combustion

model is implemented, in order to assess the effects of water injection on combustion;

- in the second part a quasi-dimensional model of an ORC unit is presented, with a particular focus on the scroll expander; firstly, the scroll expander model is presented and validated against experimental data; subsequently, the models for the remaining components of the ORC unit are described in details and the whole unit is validated against experimental data; finally, the model is used to estimate the potential energy recovery obtainable from the exhaust gases of an internal combustion engine.

The thesis ends with conclusions and suggestions for further developments of the two energy recovery techniques.

References

[1] https://unfccc.int/resource/docs/convkp/kpeng.pdf

[2] https://ec.europa.eu/commission/presscorner/detail/en/MEMO_05_49

[3] Babiker, M., Reilly, J. M., & Jacoby, H. D. (2000). The Kyoto Protocol and developing countries. *Energy Policy*, *28*(8), 525-536, doi: 10.1016/S0301-4215(00)00033-1.

[4] Barrett, S. (1998). Political economy of the Kyoto Protocol. *Oxford review of economic policy*, *14*(4), 20-39, doi: 10.1093/oxrep/14.4.20.

[5] https://www.top500.org/lists/green500/list/2020/11/

[6] Romero, M., Hasselqvist, H., & Svensson, G. (2014). Supercomputers keeping people warm in the winter. In 2nd International Conference on ICT for Sustainability (ICTS), AUG 24-27, 2014, Stockholm, SWEDEN (pp. 324-332). Bokförlaget Atlantis, doi: 10.2991/ict4s-14.2014.40

[7] https://ec.europa.eu/clima/policies/strategies/2020_en

[8] DIRECTIVE 2012/27/EU OF THE EUROPEAN PARLIAMENT AND OF THE COUNCIL "on energy efficiency, amending Directives 2009/125/EC and 2010/30/EU and repealing Directives 2004/8/EC and 2006/32/EC", Official Journal of the European Union.

[9] Jadhao, J. S., & Thombare, D. G. (2013). Review on exhaust gas heat recovery for IC engine. International Journal of Engineering and Innovative Technology (IJEIT), 2(12).

[10] Karvonen, M., Kapoor, R., Uusitalo, A., & Ojanen, V. (2016). Technology competition in the internal combustion engine waste heat recovery: a patent landscape analysis. Journal of Cleaner Production, 112, 3735-3743, doi: 10.1016/j.jclepro.2015.06.031.

Part I

Supercritical water direct injection

Transportation still mostly relies on internal combustion engines. Their efficiency is one of the factors that determines their environmental impact and their appeal on the market. Thanks to technological improvements internal combustion engines have experienced a strong improvement in terms of efficiency and reliability through the years. In addition, in recent times, the ever more stringent regulations on vehicles pollutant emissions have put more pressure on manufacturers to improve efficiency and reduce pollutant emissions. To this end, heat recovery could play a major role. The classical energy recovery approach in internal combustion engines is to use a turbocharger to partially recover exhaust gases energy. In newer approaches exhaust gases energy is recovered employing Stirling cycles, piezoelectric generation or Organic Rankine Cycles (ORCs). In this chapter an innovative approach for exhaust gases energy recovery and wall heat transfer energy recovery through the use of supercritical water injection is being described, analyzed and optimized.

Chapter 2

Improving internal combustion engines efficiency

2.1 Waste heat recovery in internal combustion engines

Transportation still relies almost entirely on fossil fuels powered vehicles, even when it comes to light duty vehicles and passenger cars. The transition to a fully electric human and goods transportation is mainly limited by battery technology and the de-carbonization of the electric energy generation, which, in some cases, may even make electric vehicles less eco-friendly than fossil fuel powered vehicles [1]. The projections to 2050 show that the energy demand of the transportation sector will increase by about 42%; as regards electric vehicles, their energy consumption share is going to more than quadruple, but it will still account for less than 10% of the total transportation energy demand [2]. Therefore, the research towards more efficient internal combustion engines can still make a great difference on the environmental impact of the transportation system. On the other hand, international politics goes towards more stringent standards on pollutant emissions, which are forcing automotive manufacturers to constantly try to develop more and more efficient and eco-friendly engines. An increase of the engine efficiency leads to a reduction of GHG emissions, together with a decrease in fuel consumption, which makes the engine more appealing on the market.

The main energy losses in internal combustion engines are represented by cooling losses and exhaust gases energy, which amount to more than 60% of combustion heat [3]. Turbocharging has been one of the first attempts to recover exhaust gases energy. The first patents date back to 1906, and this technology has been widely used on vehicle engines since the late 1960s [4]. In this approach, the high enthalpy exhaust gases are expanded into a turbine, converting part of their energy into work, which is then used by a compressor to increase the pressure at the intake manifold. The pressure increase will result in a higher power output. Turbocharging does not inherently provide a net improvement in terms of efficiency, but it allows the downsizing of internal combustion

engines maintaining the desired power and torque output, while having a lower displacement engine, therefore reducing mechanical and thermal losses [5] and energy consumption of auxiliary [6]. It is therefore possible to improve internal combustion engines efficiency by coupling turbocharging with engine downsizing.

Through the years different technologies have been developed to recover exhaust gases waste heat. The common concept is to couple the internal combustion engine with another thermodynamic cycle, which takes waste heat as input and converts it into useful work. The main approaches include the use of Inverted Brayton Cycles (IBC), thermoelectric generators, Rankine Cycles (RC), Organic Rankine Cycles (ORC), Stirling engines.

Di Battista et. al. [7] developed a model able to assess the potential exhaust gases energy recovery achievable using an inverted Brayton cycle on a turbocharged diesel engine. The exhaust gases coming from the engine, after flowing through the turbocharger turbine, the catalyst and the particulate filter are directed into the IBC turbine, where they expand from ambient pressure to a value below ambient pressure. The exhaust gases are then cooled using a heat exchanger, then compressed by a dedicated compressor mounted on the same shaft of the IBC turbine. The suction produced by the compressor is what allows the turbine to expand the exhaust gases below ambient pressure. A schematic of the cycle is presented in Figure 2.1. The authors concluded that, under realistic operating conditions, the energy recovery is no more than 2.5%.

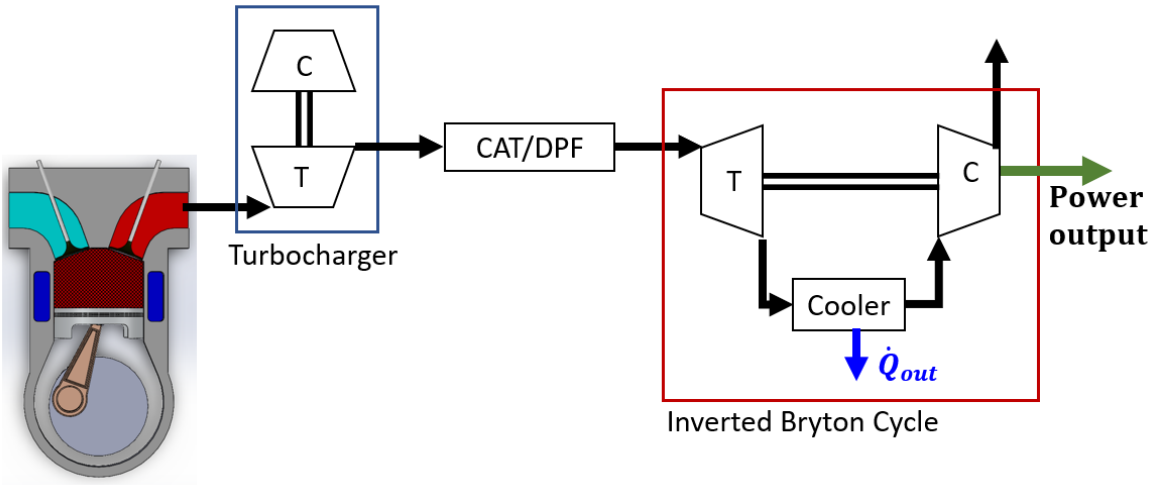

Figure 2.1: Coupling between turbocharged internal combustion engine and inverted Brayton cycle. In this configuration the Inverted Brayton Cycle is bottomed to the turbocharger, catalyzer and particulate filter.

Thermoelectric generators convert waste heat directly into electrical energy thanks to the Seebeck effect. They are a promising waste heat recovery technology due to their silent operation and high reliability. They require no moving parts or additional mechanical components, but only a heat sink to transfer the waste heat to be recovered.

The studies [8,9] have concluded that the use of thermoelectric generators in internal combustion engines could reduce fuel consumption up to 5%.

The thermodynamic process used in waste heat recovery through Rankine cycles is similar to the process used in large-scale steam power plants: a high-pressure liquid (pressurized using a pump) is evaporated introducing heat into the system (in the case of internal combustion engines exhaust gases heat is used), power is then generated by expanding the vapor. The expander can be either a turbine or a volumetric expander, the former returns better performances in high specific power plants, while the latter is to be preferred for small and medium scale plants. The low-pressure vapor is then condensed before being pressurized by a pump. Rankine cycles and organic Rankine cycles operate according to the same thermodynamic cycle, what makes them different is the working fluid, which is water for conventional Rankine cycles, while an organic fluid is used for ORCs. The use of organic fluids allows to perform the expansion to lower enthalpy states without incurring in condensation and to evaporate them using low temperature heat sources, due to their lower boiling temperature. A schematic of a Rankine cycle coupled with an internal combustion engine is presented in Figure 2.2. Thermodynamic studies have shown that using ORCs to recover waste heat can increase the power output of an internal combustion engine up to 10% [10-12]. These studies have considered industrial scale reciprocating engines, where the overall dimensions of the ORC system are not problematic. In vehicle applications, RC and ORC development mainly focused on truck engines, due to the relatively large amount of waste heat available, the large number of cruising hours and the lower impact of the system size [13].

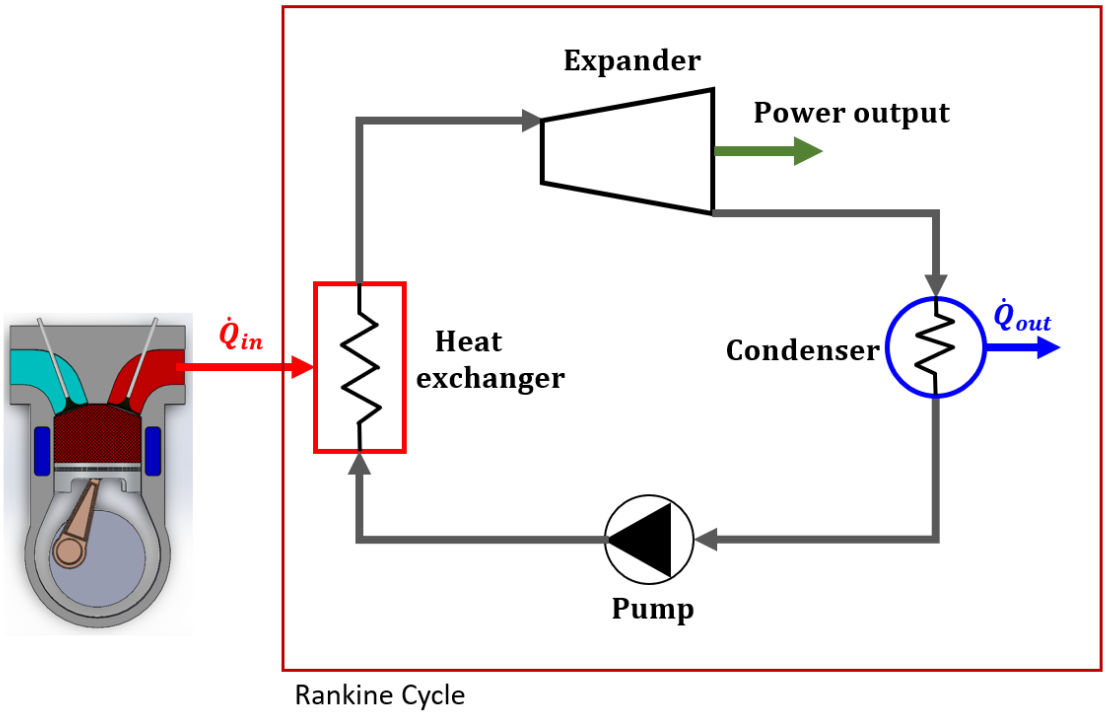

Figure 2.2: Rankine cycles coupled with an internal combustion engine. Exhaust gases are used as the Rankine cycles heat source.

In all the technologies presented, the waste heat recovery results in a limited improvement in terms of efficiency and power output (between 2% and 10%). This is due to the low-enthalpy state of the heat we are trying to convert into work, which limits the recovery efficiency. The pursuit of new energy recovery technologies and the improvement of the existing ones is still reasonable due to the popularity of internal combustion engines: a small energy recovery in a vast number of machines will result in an overall large amount of energy recovered. In addition, the higher power output could allow engine downsizing, which, as stated before, improves the overall engine efficiency.

2.2 Water injection in internal combustion engines

The historical use of water in internal combustion engines aimed to avoid or reduce the occurrence of knocking phenomena, which limits the maximum achievable compression ratio in spark ignition engines. Knocking is undesirable in internal combustion engines, since the uncontrolled combustion process leads to high pressure gradients and vibrations, which reduces the engine lifetime and its reliability. Thanks to the relatively-high water heat of vaporization and specific heat, the injection of liquid water, either in the intake manifold or directly into the combustion chamber, reduces the temperature

at the end of the compression stroke, which directly relates to the engine knock tendency. This concept was firstly applied to military aircraft engines. *Rowe and Ladd* [14] investigated the use of water and water-alcohol blends as anti-detonant and internal cooling fluids on aircrafts spark ignited engines. The anti-detonant fluid was introduced together with the intake flow during the intake stroke. A first result was the reduction of compression work by 10∼12% when water was injected. The experimental investigations also provided an increase of the detonation limited IMEP when water was added to the intake air. In particular, with a water/fuel mass ratio of 0.50 under stoichiometric conditions, the detonation limited IMEP increased by 45%. Only in recent years, due to the more stringent emissions standards, water injection is being studied for mass produced engines applications.

Berni et al. [15] investigated the potential reduction of brake specific fuel consumption using indirect water injection into a high specific power GDI turbocharged engine. In such an engine, it is common practice to use fuel rich mixtures at high loads in order to limit the engine knock tendency. The results show that the use of water injection leads to the same charge cooling effects obtained with fuel rich mixtures. Therefore, using water injection results in a lower specific fuel consumption, due to both a reduced equivalence ratio and an early spark advance without incurring in knocking phenomena. The work of *Hunger et al.* [16] also aims to assess the potential of water injection into SI engines with a particular focus on the effects of water injection parameters, such as the start of water injection, the amount of water injected and the injector location. The results show that the optimal injection timing is achieved when, at the start of injection, the in-cylinder temperature is higher than the water vaporization temperature. Indeed, water immediately vaporizes, avoiding wall wetting and resulting in a lower temperature at the end of the compression stroke, which drastically reduces the in-chamber temperature and, consequently, the knock tendency. At the selected operating conditions, a water/fuel mass ratio of 0.25 advances the center of combustion, defined as the time when 50% of the fuel mass is depleted, by 11 CAD, while doubling the amount of water results in an additional advance of 5 CAD with a reduction of 10.5% of the specific fuel consumption. Their results also point out that direct water injection has a stronger impact on the center of combustion advance with respect to indirect water injection. A comprehensive experimental analysis on the effects of direct water injection into SI engines at different engine loads and rpms is presented in the study of *Hoppe et al.* [17]. The results show an overall reduction of the specific fuel consumption. Furthermore, the minimum specific fuel consumption is achieved for a wider range of operating conditions. In addition, the engine knock tendency is strongly reduced, allowing higher compression ratios. In their study, the water/fuel mass ratio ranges from 0.1 to 0.9. The potential need of a water tank is also addressed in [17], concluding that this need may be avoided with water condensation from air conditioning or exhaust gases. *Wang et al.* [18] also investigated the effects of water injection on SI aircraft engines fueled with kerosene. The results show a potential increase of engine performances up to 28% when water injection is applied, due to the reduced knock tendency, which allows higher compression ratios.

Water injection has also been proven to reduce NOx emissions as a consequence of the lower in-chamber temperatures. The work of *Tesfa et al.* [19] shows a reduction of NOx by 50% when water injection is used for compression ignition engines. Other authors have confirmed the positive effect of water on pollutant emissions in compression ignition engines with a dedicated water injector for adding water during the compression stroke [20] or with water emulsified diesel fuels [21]. *Shain et al.* [22] experimentally determined the effects of intake manifold water addition in a turbocharged diesel engine. The results showed a significant reduction of NOx emissions, without any evident negative effect in terms of power and fuel consumption. Similarly, *Serrano et al.* [23] experimentally determined the effect of indirect water injection on the emissions of a turbocharged diesel engine. The main finding of their work is that water injection results in a comparable NOx reduction with respect to that obtained by using Exhaust Gases Recirculation (EGR), which, however, leads to a substantial increase of soot production. This negative trend can be avoided with water injection, which makes this approach very attractive to reduce diesel engines pollutant emissions. Specifically, depending on the engines load, an appropriate amount of water injection may lead to a reduction of NOx between 50% and 70%, without any significant penalty in terms of efficiency and fuel consumption.

2.3 Waste heat recovery through supercritical water direct injection

The use of water in internal combustion engines has been proven to give benefits in terms of both knocking mitigation and pollutant emissions reduction. These effects, even if desirable, do not inherently have a substantial impact on efficiency and do not perform any kind of energy recovery.

The approach that will be illustrated in the following sections aims to use water injection for energy recovery purposes. The main difference between this approach and the water injection approaches seen in the previous section is the use of water in gaseous form. This avoids the pressure drop caused by the relatively-high water latent heat of vaporization, which is one of the negative aspects of using liquid water.

The idea is to recover internal combustion engine's wall heat transfer and exhaust gases waste heat (which account for more than 50% of the total combustion heat release [3]) by using an inert fluid, such as water, then to reintroduce this energy into the combustion chamber through a dedicate injector during the expansion stroke. The injected water increases the combustion chamber mass and energy, which results in a net pressure increase, therefore increasing the engine power output.

The use of direct water injection as an energy recovery approach is a very recent strategy and is being studied by some researchers [24–26]. In the studies by *Zhang and Li* [25] and *Li and Zhang* [25], GT-POWER solver was used to estimate the potential efficiency benefit of in-cylinder direct injection of the steam superheated by the thermal energy of exhaust gas. The steam was injected into the engine chamber during the compression stroke of a turbocharged diesel engine [24] or during the expansion stroke of a natural gas turbocharged engine [25], with an appropriate timing to avoid an interaction with combustion. Indeed, the injection of a large amount of water steam right before or during combustion would influence the chemical kinetics and flame propagation and this interaction was not modeled in such works. The results suggest that superheated steam direct injection could lead to a potential reduction up to about 5% in terms of specific fuel consumption. As a steam injection pressure up to 40 bar is used, the injection timing was selected to ensure that the in-cylinder pressure was below 40 bar during injection. In the work of *Liu et al* [26], a preheater was used to increase the water temperature up to 358 K by recovering heat from the coolant and the injection pressure was set to 150 bar. The water vapor temperature was computed based on the exhaust gas temperature, which was measured in the engine in the absence of water injection.

In the following paragraphs the potential benefits of waste heat recovery by means of supercritical water direct injection will be analyzed, by using the recovery device layout shown in Figure 2.3.

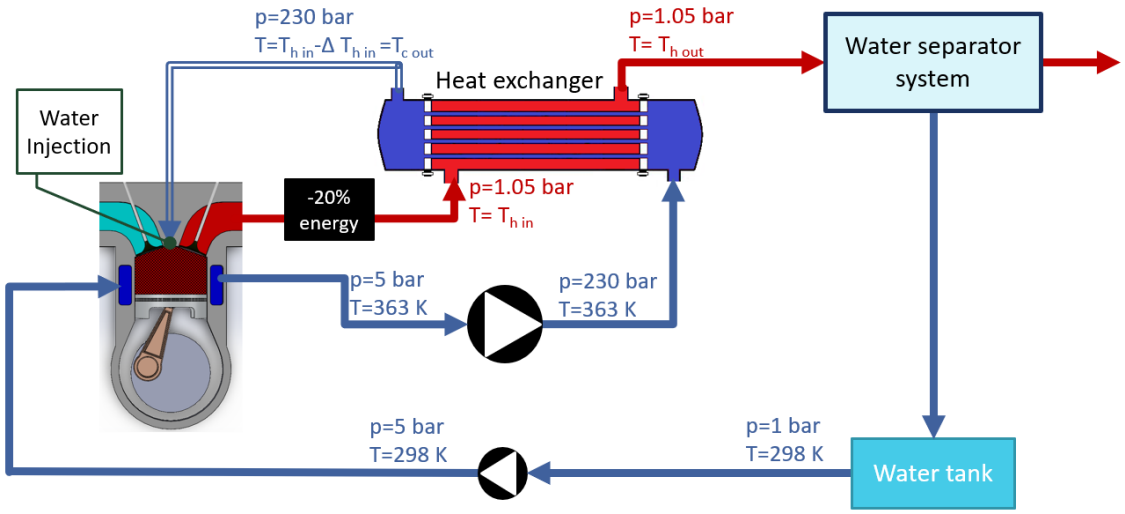

Figure 2.3: Internal combustion engines waste heat energy recovery through direct water injection: energy recovery device layout.

The liquid water is stored at ambient conditions, i.e. 1 bar and 298 K, in a water tank, which is a small buffer container filled up of water which is recovered from the exhaust gas. A low-pressure pump increases the pressure of the liquid water to 5 bar. Such water is used to partially cool the engine. The water leaves the engine at about 363 K. Then, the water is pressurized up to 230 bar by means of a high-pressure pump. Therefore, it flows through a heat exchanger, where, due to the heat provided by the engine exhaust

gas, undergoes a phase change and reaches the injection temperature $T_{c\,out}$. Finally, such water is directly injected into the engine combustion chamber. As regards the engine exhaust gas, such gas flows through the heat exchanger and enters into a water separator system, which is a condenser that separates the fraction of liquid water from all the other chemical species. In this work, it is assumed that water is condensed by means of ambient air as a cooling fluid in the condenser. The water loop closes back to the tank, which is fed by the water coming from the separator.

The energy recovery system just described may lead to a substantial improvement of the engine efficiency, but many topics need to be carefully addressed. The potential benefits may include:

- *Increased power output*: the energy recovered and reintroduced into the combustion chamber and the additional mass injected is probably going to increase the in-chamber pressure, resulting in a higher engine power output;
- *Positive effects on combustion*: the injected water will increase the in-chamber turbulence, which may lead to a fast combustion, therefore improving the engine power output;
- *Engine downsizing*: the increased engine power output may allow engine downsizing, which generally translates in higher efficiency;
- *Pollutant control*: the presence of high water quantities may affect the chemical reactions that take place inside the combustion chamber; several studies [19-23] have shown that the presence of water may reduce engines pollutant emissions. Nonetheless, in order to have a reliable measure of this effect CFD models with detailed chemical kinetics and/or experimental campaigns are needed.

On the other hand, some negative aspects may appear, such as:

- *Increased wall heat transfer*: considering the injection pressure and the in-chamber pressure, water injection will result in a supersonic jet, which will cause a considerable in-chamber turbulence increase. Even if water will likely reduce the in-chamber temperatures, which during the expansion stroke reach values of about 2500 K, the preponderant effect will probably be the increased turbulence, which will increase the wall heat transfer losses;
- *Negative effects on combustion*: injecting water directly into the combustion chamber may lead to flame quenching if the injection timing is not carefully addressed, causing a lower combustion efficiency;
- *Decreased system reliability*: the energy recovery system as described above adds several components to the internal combustion engine: two water pumps, a heat exchanger, a water separator system, a water tank, a dedicated water injector and several pipes and manifolds. Adding components always negatively impact the reliability of a system, since the probability of failure depends on the reliability of the single component and the number of components;

- Energy recovery system size: it can be difficult to fit the additional components to vehicles.

In the following paragraphs some of these issues will be deeply analyzed, in order to assess the real potential of this novel waste heat recovery approach. The first approach is a thermodynamic analysis, using a 0-D model. This type of modelling is characterized by very short computational times and, if carefully calibrated, can provide a good initial understanding of the potential benefits achievable. In addition, it can be used to perform a global optimization of the system, which would be very time consuming if performed with CFD techniques or by experiments. Subsequently, a CFD model is developed, in order to investigate more in depth the phenomena that take place, including the effects on combustion and wall heat transfer.

The energy recovery system by means of supercritical water injection can be in theory applied to any type of internal combustion engine. Overall, the system would work with the same components, but different engines are going to face different issues. For example, a turbocharged engine would have a lower exhaust gases enthalpy, since part of the energy has already been used by the turbine, therefore limiting the amount of water that can be heated up beyond the boiling point. In addition, a high amount of water in the exhaust gases could damage the turbine. In diesel engines the profoundly different combustion process would require a profoundly different injector architecture and timing. Therefore, each engine type requires a specific development procedure in order to implement such an energy recovery approach. The present work is focused on the development and optimization of the energy recovery system by means of direct water injection for a Port Fuel Injection (PFI) Spark Ignition (SI) engine.

Chapter 3

Supercritical water direct injection: a thermodynamic analysis

3.1 Engine thermodynamic analysis

3.1.2 The WISE quasi-dimensional model

A quasi-dimensional numerical model, named WISE (Water Injection Spark Engine), has been developed and validated in order to assess the SI engine performances with supercritical water injection. The model accounts for gas species thermodynamic properties, based on Janaf tables [27], and for supercritical steam water properties, based on CoolProp libraries [28]. The code includes several sub-models to simulate valves opening/closing, wall heat transfer, water injection and combustion. The code is written in FORTRAN language. All models and parameters used in WISE are described in this section in detail.

Governing equations

The WISE code solves a system of Ordinary Differential Equations (ODEs) consisting of the chemical species and stagnation internal energy conservation equations:

$$\frac{dm_i}{dt} = \frac{dm_{int_i}}{dt} - \frac{dm_{exh_i}}{dt} + \frac{dm_{w_{inj}}}{dt}\delta_{iw} \qquad i = 1, \dots, NS \qquad (3.1)$$

$$\frac{dE}{dt} = \sum_{i=1}^{NS} \frac{dm_{int_i}}{dt} h_{int_i}^{tot} - \sum_{i=1}^{NS} \frac{dm_{exh_i}}{dt} h_{exh_i}^{tot} - \dot{Q}_w + \frac{dm_{w_{inj}}}{dt} h_{w_{inj}}^{tot}. \qquad (3.2)$$

In Eq. (3.1) the subscript *i* refers to the *i-th* species and δ_{iw} is 1 for the injected water, 0 otherwise. The chemical species considered are iso-octane (C8H18), nitrogen (N_2), oxygen (O_2), carbon dioxide (CO_2) and water (H_2O).

Combustion model

The combustion process has been simulated by considering a Wiebe function [3] to compute the burned fuel mass fraction, Y_f, versus crank angle, ϑ:

$$Y_f = \left\{1 - exp\left[-a\left(\frac{\theta - \theta_0}{\Delta\theta_c}\right)^{m+1}\right]\right\}. \quad (3.3)$$

where *a* and *m* are adjustable model constants, ϑ_o is the start of combustion and $\Delta\vartheta_c$ is the total combustion duration. In the model, a single global reaction has been considered where fuel burns in presence of oxygen and leads to products formation, i.e. H_2O and CO_2. In the model validation process, the model constants of the Wiebe function have been adjusted to account for the actual combustion process, thus accurately predicting the heat release rate.

Finally, the apparent heat released during combustion is determined for each time step of the numerical integration from the enthalpy of formation of the chemical species mass fractions.

Water injection model

The water injection model has been implemented to take into account the mass and energy of injected water into the engine chamber based on user-defined injection parameters. Specifically, the parameters are the total mass of injected water, the Start Of Injection (SOI) and the Water Injection Duration (WID) given in crank angle degrees, the temperature and pressure of injected water. Since water has been injected under supercritical conditions, the water temperature and pressure are higher than 647.1 K and 220.6 bar, respectively. In the simulations, the in-cylinder pressure peak is 50~70 bar, thus the injector always works under choked conditions. Hence, the mass flow rate is given by Eq. (3.4) by considering an isentropic expansion in the injector. In Eq. (3.4) A_{inj} is the injector exit area, p^{tot} and T^{tot} are the stagnation pressure and temperature of injected water, respectively, R is the specific gas constant and γ is the heat capacity ratio.

$$G = A_{inj}\frac{p^{tot}}{\sqrt{RT^{tot}}}\sqrt{\gamma}\left(\frac{\gamma+1}{2}\right)^{-\frac{\gamma+1}{2(\gamma-1)}}. \quad (3.4)$$

Based on such assumptions, WID only depends on the injector geometry, i.e. on the injector equivalent diameter.

The thermodynamic properties for the injected supercritical water are defined according to the CoolProp libraries [28], which provide accurate data for supercritical fluids.

Intake/exhaust valves model

The input parameters for the valves model are the same for both intake and exhaust valves, thus only those for the intake valve are listed here:

- Intake valve max area Av_{max};
- Intake pressure p_{intake};
- Intake temperature T_{intake};
- Intake discharge coefficient $c_{d\text{-}intake}$;
- IVSO (Intake Valve Start Opening);
- IVFO (Intake Valve Full Opening);
- IVSC (Intake Valve Start Closing);
- IVFC (Intake Valve Full Closing).

The model assumes that the intake valve follows a linear opening from IVSO to IVFO, when the maximum opening area is reached. From IVFO to IVSC the intake valve remains fully opened and from IVSC to IVFC the intake valve follows again a linear closing. Figure 3.1 shows an example of the intake valve opening/closing.

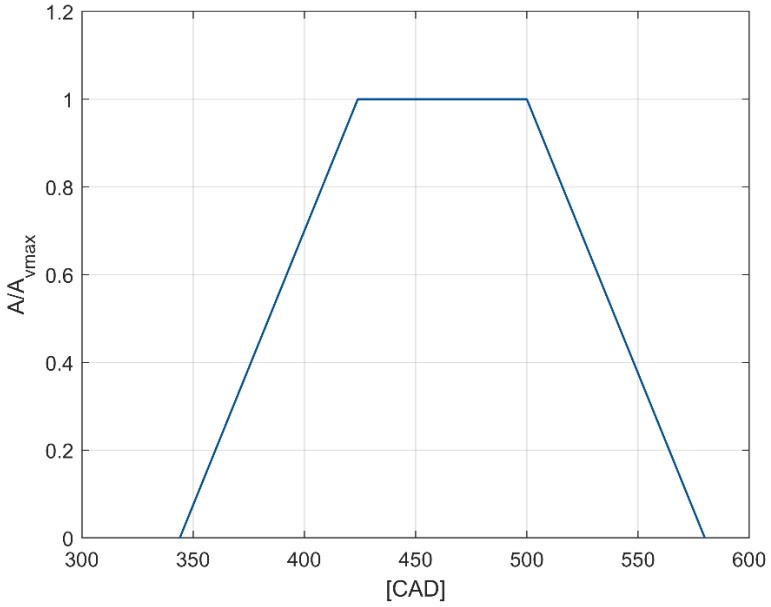

Figure 3.1: Intake valve opening and closing (IVSO=344 CAD, IVFO=424 CAD, IVSC=500 CAD, IVFC=580 CAD).

The mass flow rate through the intake valve has been evaluated based on the intake and cylinder thermodynamic conditions. The model limits the mass flow rate to choking conditions and accounts for back flow.

Wall Heat Transfer model

The heat transfer per unit surface area, $\dot{q}_w$, depends on the temperature difference between gas and cylinder wall and on the heat transfer coefficient, h_c. In this work, the temperature difference is based on the instantaneous in-cylinder temperature $T_g(t)$, and engine wall temperature, T_w, which is assumed constant. Therefore, the heat transfer per unit surface area is computed according to the following equation:

$$\dot{q}_w(t) = h_c(T_g(t) - T_w). \tag{3.5}$$

An Annand-type correlation [14] is employed to estimate the heat transfer coefficient, h_c, as:

$$h_c = a\frac{k}{B}Re^b. \tag{3.6}$$

where a, b are model constants, B is the engine bore, k the in-cylinder gas thermal conductivity and Re is the in-cylinder Reynolds number.
The thermal conductivity, k, is evaluated by the Prandtl number, Pr, assumed equal to 0.7:

$$Pr = \frac{\mu C_p}{k}. \tag{3.7}$$

where μ is the gas dynamic viscosity and $C_p$is the specific heat at constant pressure. The Reynolds number is evaluated by using the following expression:

$$Re = \frac{\rho\overline{v_p}B}{\mu}, \tag{3.8}$$

where ρ is the in-cylinder gas density and $\overline{v_p}$ is the piston mean velocity.

Finally, the total wall heat transfer rate, $\dot{Q}_w(t)$, is computed by using the following relation:

$$\dot{Q}_w(t) = \dot{q}_w(t) * \left[2\frac{\pi B^2}{4} + \pi B * y(t)\right], \tag{3.9}$$

where $y(t)$ is the instantaneous distance of the piston from the cylinder head and the term inside the square brackets represents the total instantaneous heat transfer area.

Numerical model

The model performs a numerical integration of the species and energy conservation equations (Eq. (3.1) and Eq. (3.2)) by means of a first-order accurate Euler method. A relatively small time step, equal to 10^{-6} s, is used which corresponds to $9.26\text{x}10^{-8}$ CAD at 2000 rpm, in order to ensure high accuracy. The computations start at 90 CAD before TDC with initial gas temperature and pressure in the chamber equal to 300 K and 1 bar, respectively. Several engine cycles are carried out in order to reach a cyclic convergence.

For all cases, 5 engine cycles ensure a good cyclic convergence, as shown in Figure 3.2, where the convergence history is given in terms of the in-cylinder pressure.

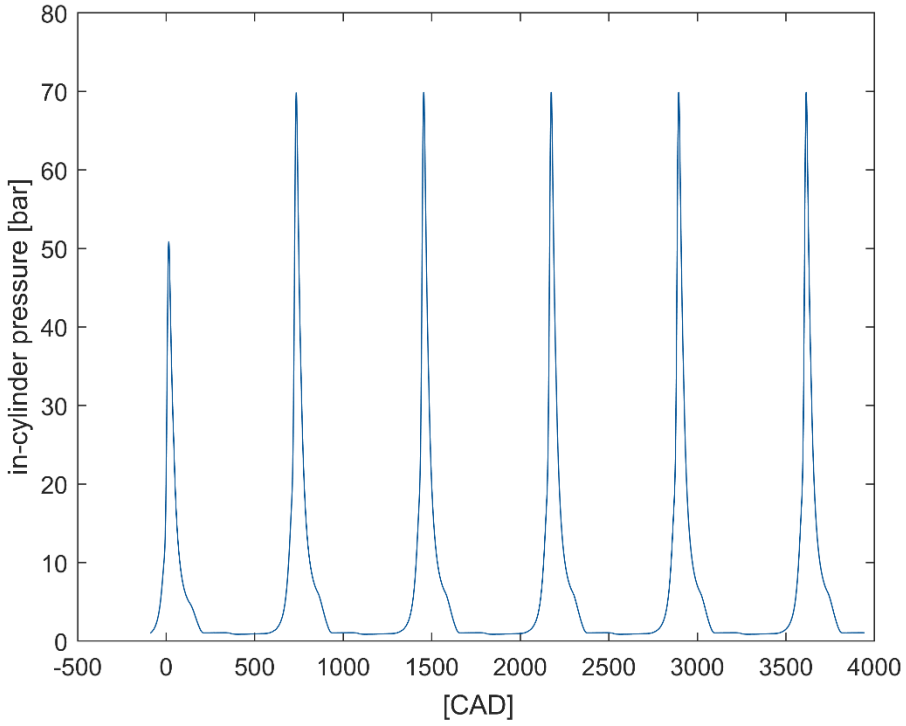

Figure 3.2: Convergence history (0 CAD = TDC firing)

3.1.2 Model validation

The WISE model has been validated by comparing the numerical results with available experimental data of a naturally aspirated engine [29], whose parameters are shown in Table 3.1. The calibration of the WISE models constants have been carried out by using the data available in [29], i.e. the instantaneous measured in-cylinder pressure profiles obtained with different values of spark timing (7, 5, 3 and 1 CAD BTDC) and the heat release rate with a spark timing equal to 3 CA BTDC.

By setting the WISE code combustion model with *a=12.8*, *m=4.9*, a combustion duration of 60 CAD and *a=0.4* and *b=0.7* for the heat transfer model, a good agreement is obtained both in terms of in-cylinder pressure and heat release rate. Figure 3.3 and Figure 3.4 show the comparison between experimental data and numerical results in terms of in-cylinder pressure and heat release rate, respectively.

Table 3.1. Reference engine specifications [29].

Displaced volume	399 cc
Stroke	81.3 mm
Bore	79.0 mm

Connecting Rod	143.0 mm
Compression ratio	10:1
Engine speed	1000 rpm

For earlier Spark Advance (SA), the results show that the start of combustion is advanced, which results in a higher pressure peak. Overall, the WISE code provides a good comparison in terms of pressure traces for all the tested conditions.

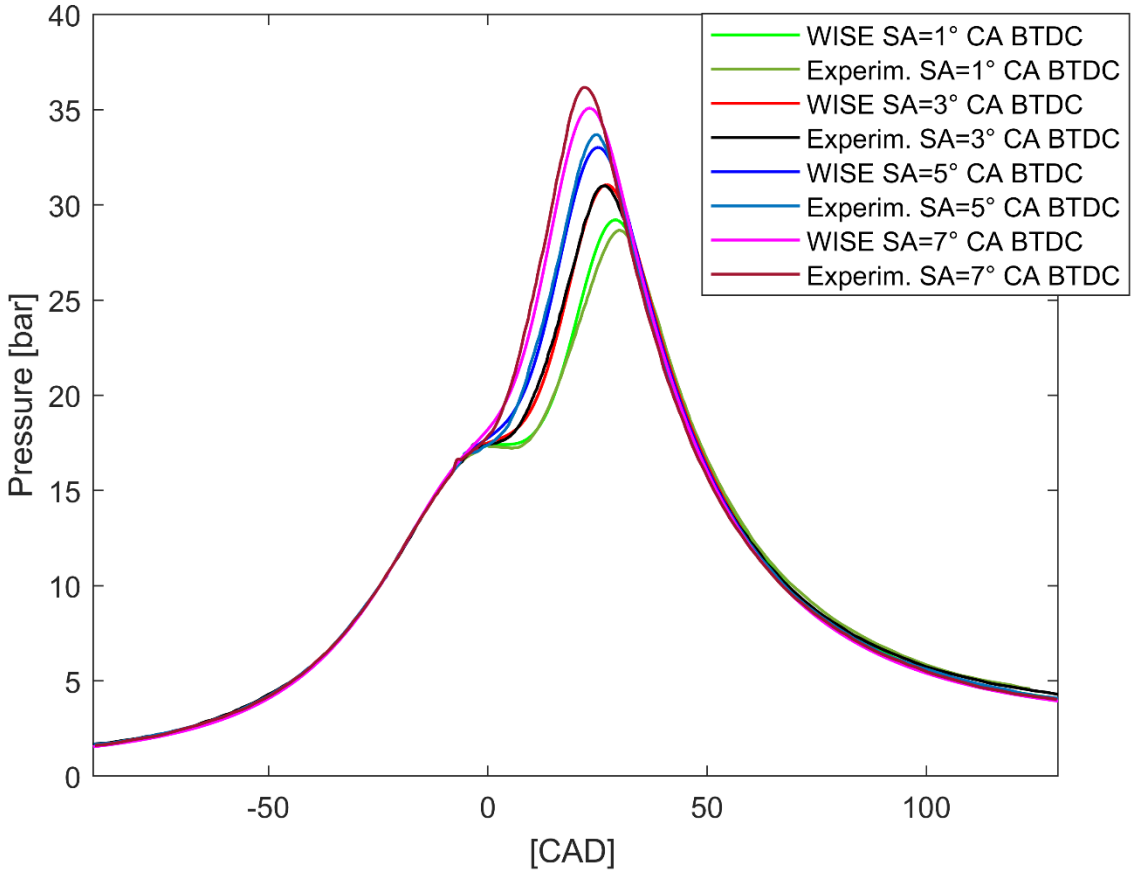

Figure 3.3: In-cylinder pressure vs CAD: WISE vs Experimental [29] for different spark advance, SA, values (0° CAD = firing TDC).

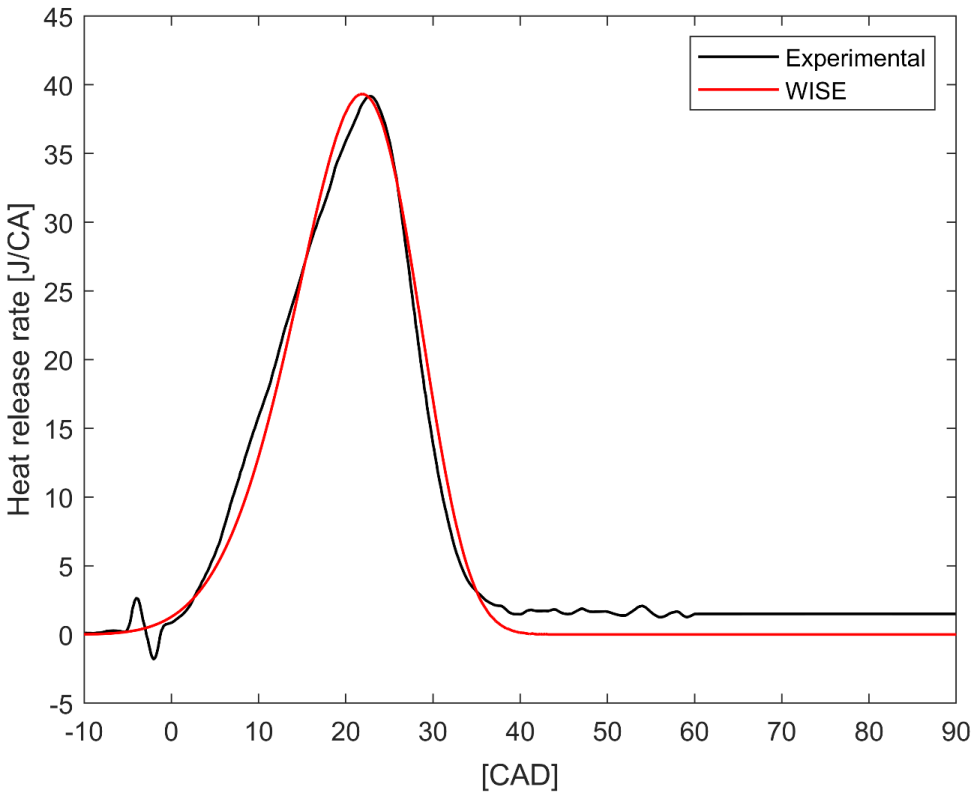

Figure 3.4: Heat release rate vs CAD: WISE vs Experimental [29] for SA = 3° CA BTDC (0° CAD = firing TDC)

3.1.3 Supercritical water direct injection: baseline case

All the simulations with supercritical water injection have been performed by considering the engine described in the previous section, with the same model constants and with a spark advance of 3 CAD BTDC.

The water injection parameters of the baseline case are summarized in Table 3.2.

Table 3.2. Water injection parameters of the baseline case

Water/fuel ratio	7
WID	15° CA
SOI	35° CA after TDC firing
Injection water pressure	230 bar
Injection water	700 K

The choice of water/fuel ratio equal to 7 is based on preliminary considerations of the presumed maximum amount of water that can be heated to supercritical temperature by recovering heat from engine cooling and exhaust gases. The choice of WID derives from considerations on the injector equivalent diameter. By considering the engine operating conditions (1000 rpm) an injector of equivalent diameter equal to 1.43 mm

has been chosen to inject supercritical water vapor (mass flow rate equal to 0.04352 kg/s) such that W/F ratio is 7 and the injection duration is 15° CAD.

Since the model does not account for water injection – combustion interaction, the start of injection is delayed to the time when the cumulative heat release due to combustion is equal to 99.3%, i.e. 35° CA ATDC. Hence, the water injection-combustion interaction is neglected.

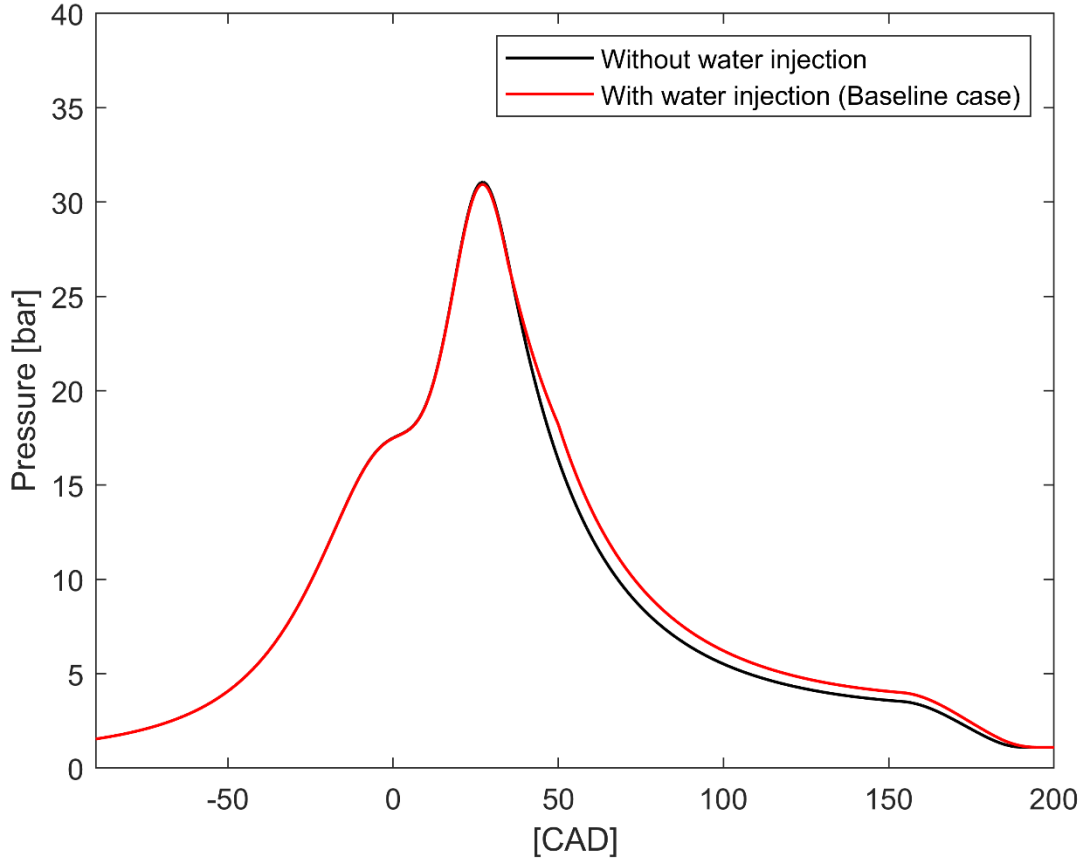

Figure 3.5: In-cylinder pressure vs CAD, with and without water injection (baseline case).

Figure 3.5 compares the pressure profiles, with and without water injection, for the baseline case. The figure shows an increase of the chamber pressure during the expansion stroke from the SOI to the opening of the exhaust valve due to the supercritical water injection. Hence, the work cycle returns a higher value, which also means a higher overall engine efficiency, as shown in Figure 3.6 where the results are given in a p-V diagram.

Indeed, in terms of both engine work and efficiency, the injection of water provides an increase of about 10%. As explained in the Introduction section, water is heated to supercritical state by recovering heat from engine cooling and exhaust gases. The water is brought to the liquid state in a condenser and an auxiliary work is required to pump liquid water to 230 bar. The water mass flow rate is relatively low, thus such pump work

can be neglected at first instance. The engine work and efficiency with and without water injection are summarized in Table 3.3.

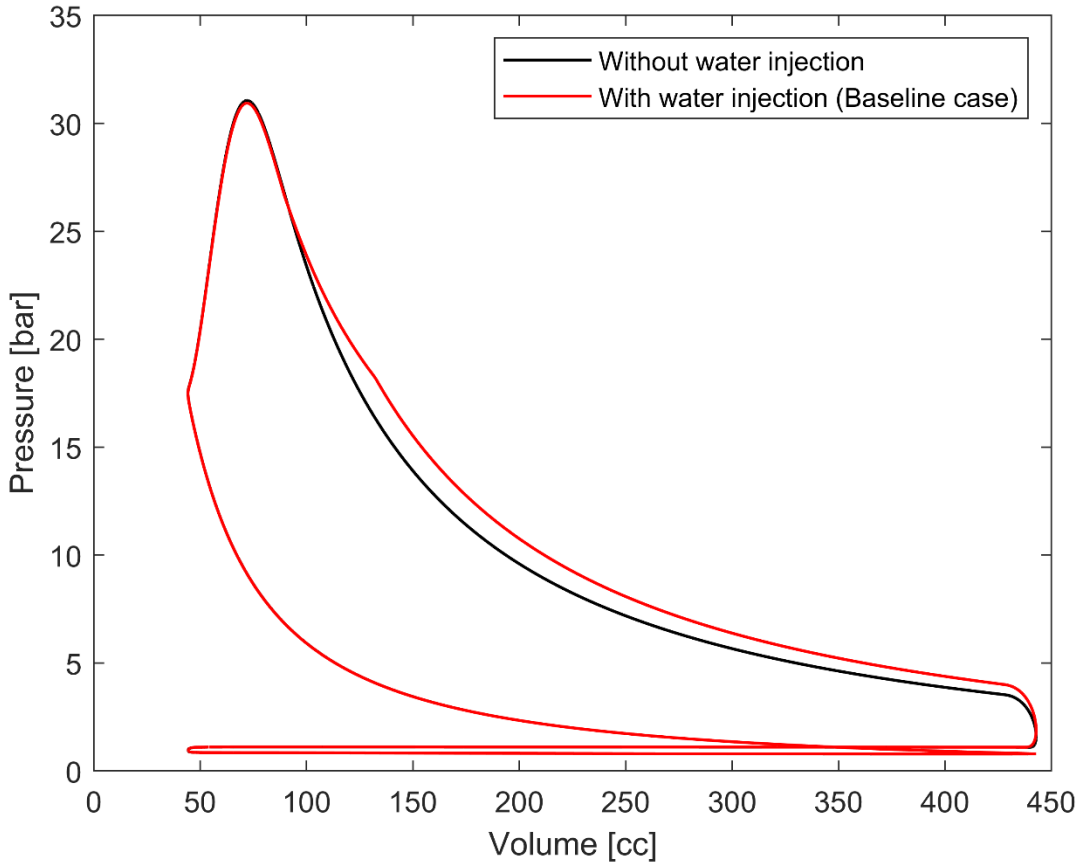

Figure 3.6: Baseline engine cycle, with and without water injection.

Table 3.3. Comparison between engine work and efficiency with and without water injection

	W/F	**Work [J]**	**Efficiency**
No water inj.	0	294.5	0.427
Baseline case	7	325.4 (+10.5%)	0.473 (+10.8%)

As expected, water injection also determines a decrease of the in-cylinder temperature (Figure 3.7), which results in a reduction of the wall heat transfer. A lower in-cylinder temperature is also expected to have effects on thermal NOx emissions and knocking tendency.

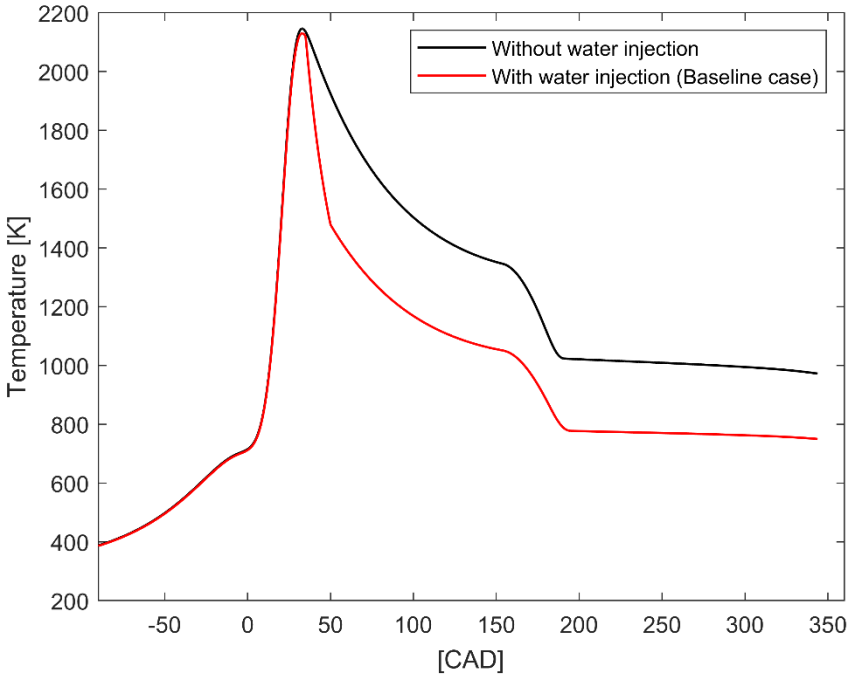

Figure 3.7: In-chamber temperature in the cases with and without water injection (0° CAD = firing TDC).

3.1.4 Supercritical water direct injection: parametric analysis

The WISE 0-D model represents a very useful tool to predict and analyze how water injection parameters affect the engine work and efficiency. This analysis can be considered as a preliminary study for 3D-CFD simulations. Indeed, WISE is able to select and identify those engine parameters that mainly influence the engine performance with supercritical water injection. 3D-CFD simulations are required to assess the effects of supercritical water injection-combustion interaction. However, this parametric analysis can provide useful suggestions as regards injections parameters.

The parametric analysis has been focused on the effects of the water/fuel ratio, the SOI and the WID. Unless otherwise specified, the values of the injection parameters are those used in the baseline case (Table 3.2).

Influence of Water/Fuel ratio

The amount of injected supercritical water is directly related to the combustion chamber pressure increase, which provides the engine efficiency and work improvement. The maximum amount of supercritical water that can be injected is limited by the exhaust gases enthalpy, since by increasing the amount of water the exhaust gas temperature decreases and, at the same time, more energy is needed to increase the injection water temperature.

In this paragraph, we are focusing on the correlation between the amount of water injected and the efficiency gain, with the hypothesis of constant injection temperature.

In the water/fuel ratio parametric study, the engine efficiency and engine work cycle with W/F ratios from 1 to 7 have been evaluated and compared with those obtained without water injection. The same injector geometry has been considered for all cases, thus the WID has been adjusted accordingly, as shown in Table 3.4, which also shows the efficiency and mechanical work increases.

Table 3.4. Water/fuel ratio parametric analysis results

W/F	WID [CAD]	Work [J]	Efficiency (%gain)
0	0	294.5	0.427
1	2.1	298.7 (+1.4%)	0.433 (+1.4%)
2	4.3	303.1 (+2.9%)	0.440 (+3.0%)
3	6.4	307.6 (+4.4%)	0.447 (+4.7%)
4	8.5	312.1 (+6.0%)	0.454 (+6.3%)
5	10.7	316.6 (+7.5%)	0.460 (+7.7%)
6	12.8	321.0 (+9.0%)	0.467 (+9.4%)
7	15	325.4 (+10.5%)	0.473 (+10.8%)

As expected, the effect of water/fuel ratio on engine efficiency and performance improvements is significant. Indeed, a value of W/F ratio equal to 1 corresponds to an efficiency improvement of about 1.4%. At the same time, the total heat loss through the cylinder walls decreases by increasing the water/fuel ratio.

Figure 3.8 shows the engine work cycle for the case without water injection and for the cases with water/fuel ratios equal to 3 and 7. Specifically, as W/F increases, the pressure in the chamber increases during the expansion stroke.

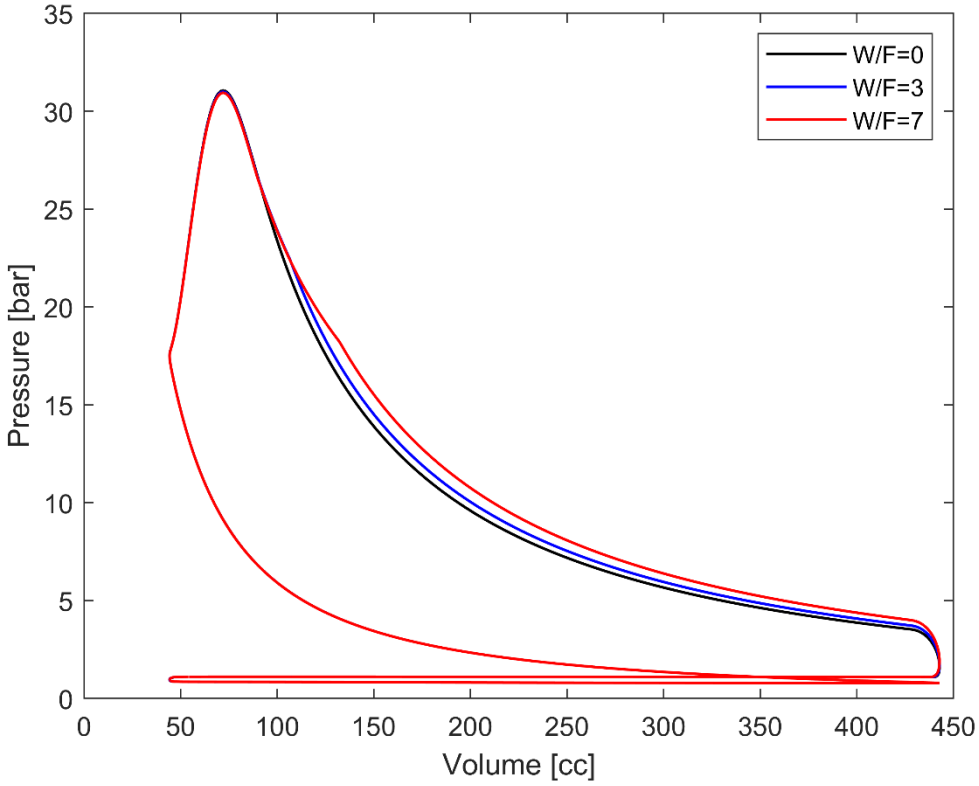

Figure 3.8: Engine cycles with different water/fuel ratios.

Influence of Start of Injection (SOI)

An SOI advance, closer to TDC, results in a higher chamber pressure after water injection and an increase of the engine efficiency. On the other hand, with advanced SOI a stronger influence on combustion is expected. Since the WISE model does not include a sub-model for the water injection-combustion interaction, injection starts when combustion is almost complete for the baseline case. Nevertheless, the gain of engine efficiency with an early water injection is computed, by assuming that there is no influence on combustion.

Three different SOIs have been considered, i.e. 30°, 35° (baseline case) and 40° CAD ATDC. As already stated before, at 35° CAD ATDC combustion has released 99.3% of the total heat, thus water injection – combustion interaction can be neglected. At 40° CAD ATDC the heat release due to combustion is equal to 99.98%, which clearly strengthens the hypothesis of no water injection – combustion interaction. At 30° CAD ATDC the heat release due to combustion is equal to 93.1%. In this case, due to the interaction between water injection and combustion, the results are less accurate.

Table 3.5 shows the results of the SOI parametric analysis. As expected, an earlier SOI provides higher efficiency and mechanical work of the engine. Specifically, with the SOI at 30° CAD ATDC an engine efficiency gain of 11.5% with respect to the case without water injection is obtained. An SOI equal to 40° CAD ATDC results in an increase in engine efficiency equal to 10.3%, 1.2% lower with respect to the previous case. Furthermore, an earlier SOI results in a reduction of the wall heat transfer, since the gas

temperature considerably decreases. This in-chamber gas temperature reduction is useful in order to reduce both NOx formation and knocking phenomena so that an increase of the engine compression ratio is welcome.

Figure 3.9 shows the engine work cycle for the case without water injection compared with the three engine cycles with different SOIs. The figure shows an increase of the chamber pressure peak as SOI is advanced. However, after water injection, the pressure profiles tend to overlap, as can be seen in Figure 3.10.

Table 3.5. Influence of SOI (0° CAD = firing TDC)

SOI [CAD]	**Work [J]**	**Efficiency (% gain)**
Without water inj.	294.5	0.427
30	327.8 (+11.3%)	0.476 (+11.5%)
35	325.4 (+10.5%)	0.473 (+10.8%)
40	324.3 (+10.1%)	0.471 (+10.3%)

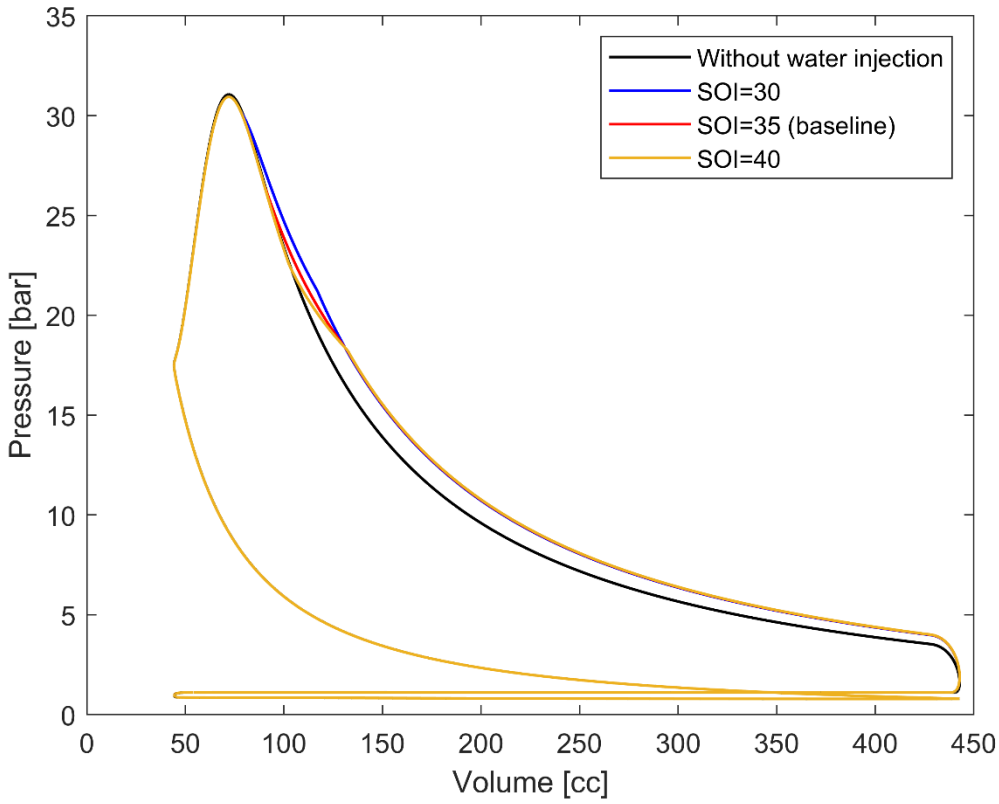

Figure 3.9: Engine cycles with different SOI.

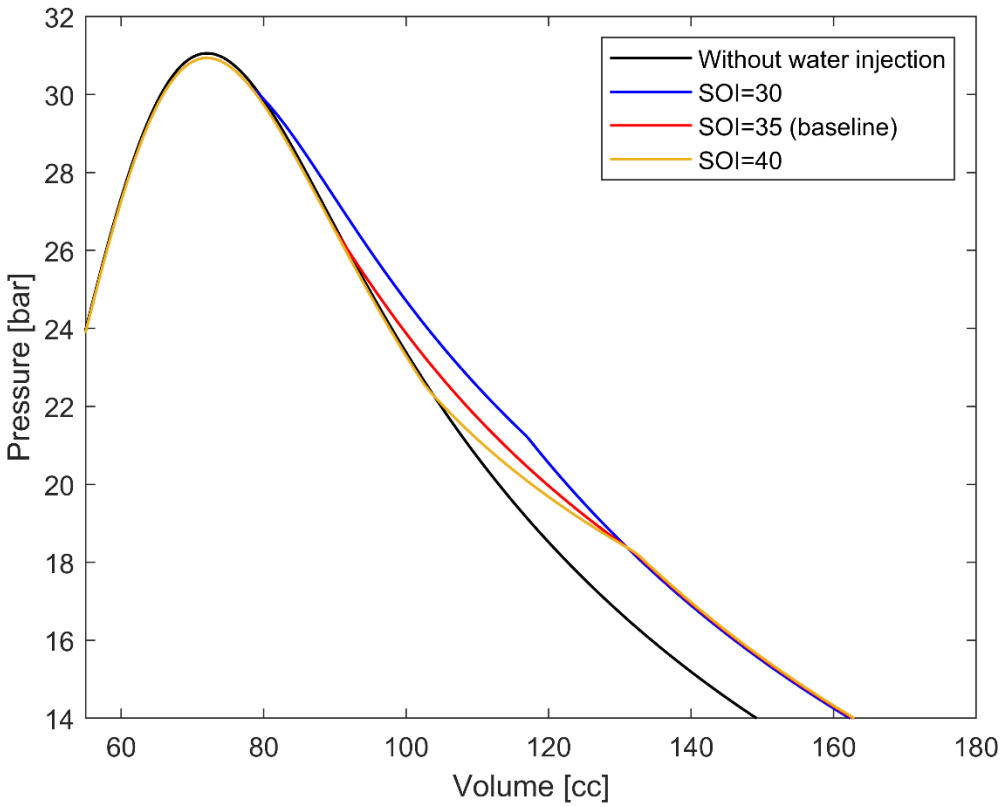

Figure 3.10: Engine cycles with different SOI (blow-up).

Influence of Water Injection Duration (WID)

In this parametric analysis, three WIDs have been investigated, i.e. injection durations equal to 10°, 15° and 20° CAD. The water injection thermodynamic parameters are kept constant, whereas the injector geometry has been modified accordingly. Specifically, for WID = 15° CAD, an injector with an equivalent diameter of 1.43 mm is considered, whereas, for the other two configurations, two injector equivalent diameters equal to 1.7 mm, with WID = 10° CAD, and equal to 1.2 mm, with WID = 20° CAD, are used. Table 3.6 shows the results of the WID parametric analysis. The engine work and efficiency increase with a shorter injection duration. As shown in the table, the influence of WID on the engine efficiency is relatively lower than the effect of water/fuel ratio and SOI. A 5° CAD difference in WID results in a change of about 0.5% in terms of engine efficiency improvement.

Figure 3.11 compares the engine cycles with different WID. With a shorter WID, the engine cycle shows a higher chamber pressure in the first part of the expansion stroke due to water injection. As in the SOI parametric analysis, as the water injection is ended, the chamber pressure profiles overlap for all the three cases, as shown in Figure 3.12.

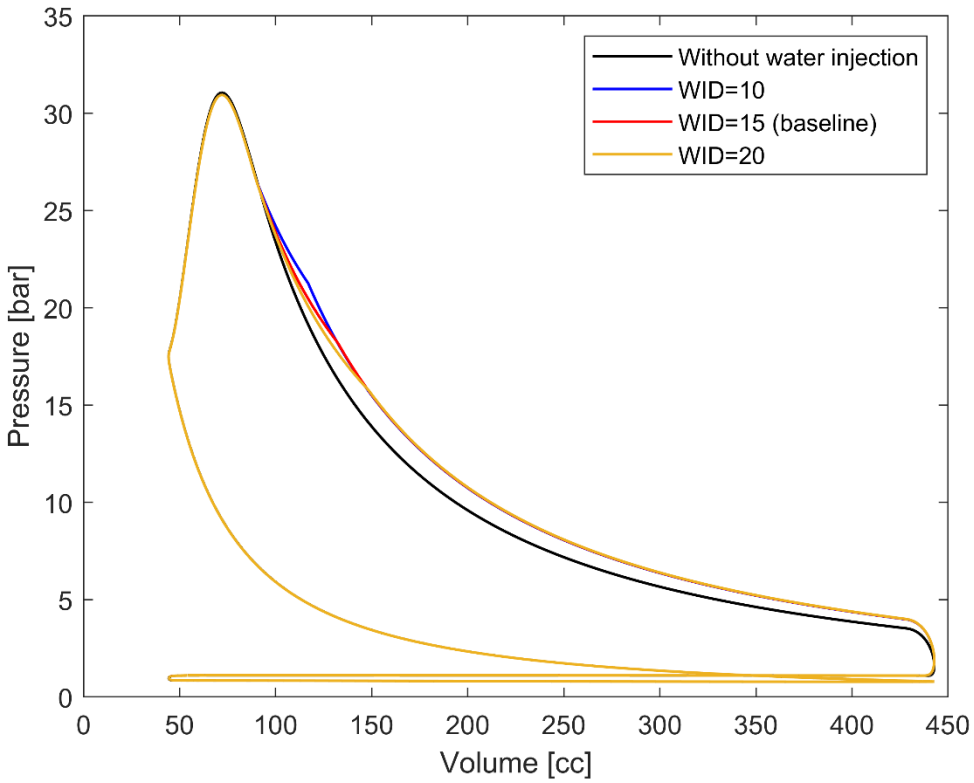

Figure 3.11: Engine cycles with different WID.

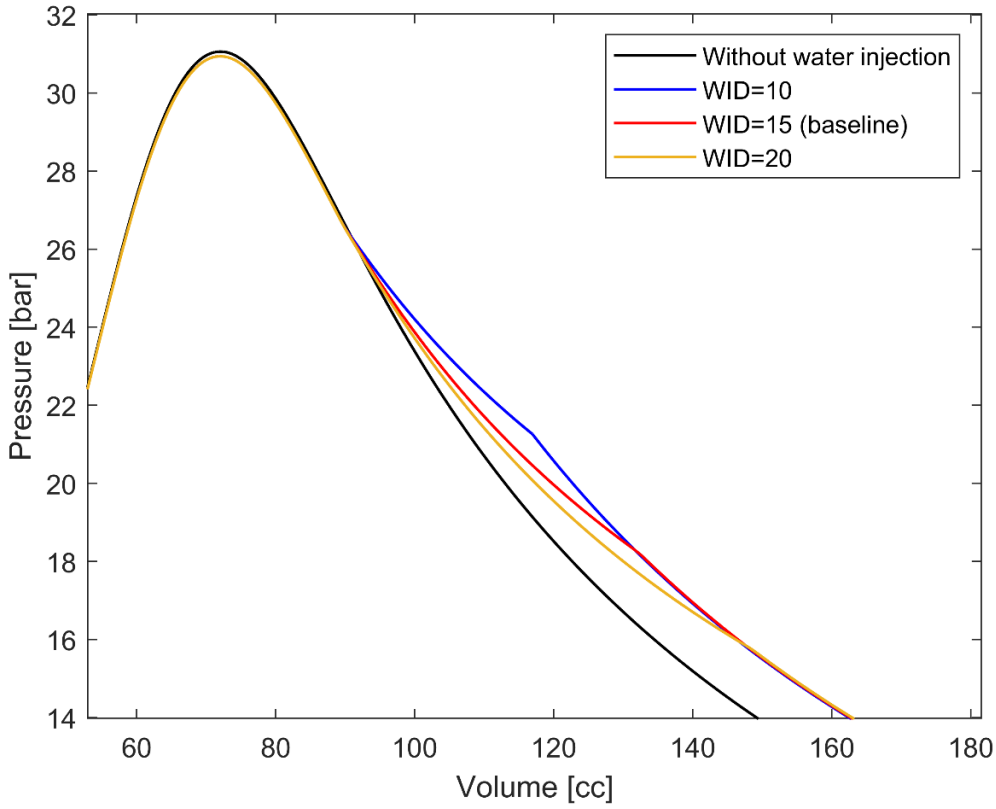

Figure 3.12: Engine cycles with different WID (blow-up).

Table 3.6. Influence of WID.

WID [CAD]	Work [J]	Efficiency (% gain)
Without water inj.	294.5	0.427
10	326.7 (+10.9%)	0.475 (+11.2%)
15	325.4 (+10.5%)	0.473 (+10.8%)
20	324.1 (+10.1%)	0.471 (+10.3%)

Influence of Spark advance

As shown in the validation section, advancing the spark timing from 3° CAD BTDC to 7° CAD BTDC results in higher engine performances and efficiency. Furthermore, with an earlier spark timing heat release is advanced and water can be injected earlier, which results in a higher efficiency gain.

Different simulations have been performed by considering the baseline case and changing the spark timing in the range 1-7 CAD BTDC. For each case, SOI has been chosen to inject water when the cumulative heat release due to combustion is equal to 99.3% and the results have been compared with the case without supercritical water injection. Table 3.7 summarizes the results in terms of performance and efficiency gains and shows for each case the value of SOI. An earlier spark timing enables to advance the SOI, which increases the water injection efficiency gain.

Figure 3.13 compares the engine cycles with and without water injection with spark timing equal to 1 and 7 CAD BTDC.

This analysis suggests that the benefit of supercritical water injection is best combined with combustion strategies that enable fast combustion.

Table 3.7. Spark advance effects on water injection efficiency and performance gains (WID equal to 15° CAD in all the configurations).

Configuration	SOI [CAD]	Work [J]	Efficiency (% gain)
SA=1 W/F=0	-	289.1	0.419
SA=1 W/F=7	37	319.0 (+10.3%)	0.464 (+10.7%)
SA=3 W/F=0	-	394.5	0.427
SA=3 W/F=7	35	325.4 (+10.5%)	0.473 (+10.8%)
SA=5 W/F=0	-	299.5	0.434
SA=5 W/F=7	33	331.4 (+10.7%)	0.482 (+11.0%)

SA=7 W/F=0	-	304.1	0.441
SA=7 W/F=7	31	336.9 (+10.8%)	0.490 (+11.1%)

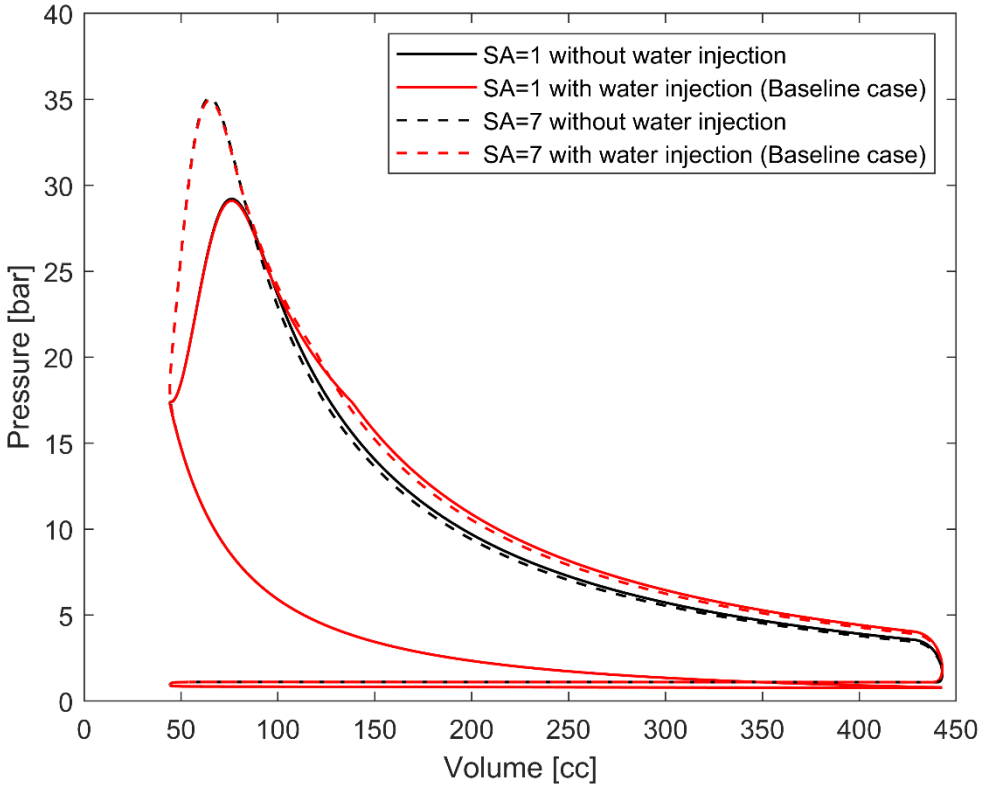

Figure 3.13: Engine cycles with different spark advances with and without water injection.

The results of this first parametric analysis are very promising. Supercritical water injection could lead to a relevant improvement in ICEs efficiency and performances.

Specifically, the injection of supercritical water directly into the engine from 35° CAD to 50° CAD after TDC, with a water/fuel mass ratio equal to 7 and a water temperature equal to 700 K, results in a 10.8% efficiency increase with respect to the case without water injection. Furthermore, the parametric study shows that the main impact on efficiency improvement is related to the water mass injected. Indeed, an injected amount of water equal to the fuel mass provides an increase of engine efficiency of about 1.4%, whereas with a water mass equal to 5 and 7 times the fuel mass an increase of efficiency of about 7.7% and 10.8%, respectively, is obtained. The SOI also has a relevant impact, since an earlier injection of 10° CAD results in a ~1.2% engine efficiency increase. Besides, the results show that the WID has only a secondary effect on efficiency improvement, with a ~0.9% efficiency increase with a WID 10° CAD shorter. The effects of spark timing on water injection efficiency gain have been examined. The spark advance does not directly affect the efficiency gain due to water injection, but an earlier SA enables to use an earlier SOI, which results in a higher efficiency improvement.

This preliminary investigation on the potentiality of supercritical water injection strategy delineates the relative importance of the various injection parameters, which may be very useful in the design choice of the injector, the engine, and the heat exchanger. In order to more accurately assess the efficiency gain obtained with water injection the other components of the system need to be modelled and coupled to the engine model.

3.2 Recovery system thermodynamic analysis

3.2.1 Recovery system mathematical modelling

The energy recovery device in Figure 2.3 consists of several other components other than the internal combustion engine. In this section the modelling of the heat exchanger and the water pumps are presented. These models are then coupled with the internal combustion engine model, in order to take into account the dependency between the engine conditions and the injection parameters.

Counter-Flow Heat Exchanger Model

A simplified counter-flow tube heat exchanger model is implemented by neglecting the pressure drop along the exchanger because it is assumed that such losses are negligible with respect to the engine power output.

The energy balance system of equations for a counter-flow heat exchanger reads:

$$\begin{cases} \dot{Q} = \dot{m}_c\left[H_{c_{out}} - H_{c_{in}}\right] \\ \dot{Q} = \dot{m}_h\left[H_{h_{in}} - H_{h_{out}}\right] \\ \dot{Q} = FK_{tot}A\left[\dfrac{\left(T_{h_{in}} - T_{c_{out}}\right) - \left(T_{h_{out}} - T_{c_{in}}\right)}{ln\left(\dfrac{T_{h_{in}} - T_{c_{out}}}{T_{h_{out}} - T_{c_{in}}}\right)}\right] \end{cases} \tag{3.10}$$

where $\dot{Q}$ is the thermal power transferred from the hot fluid to the cold fluid, $\dot{m}_c$ is the cold fluid mass flow rate, $H_{c_{out}}$ and $H_{c_{in}}$ are the cold fluid outlet and inlet total enthalpy, respectively, $T_{c_{out}}$ and $T_{c_{in}}$ are the cold fluid outlet and inlet temperature, respectively, K_{tot} is the global heat transfer coefficient, *A* is the exchanger total area, and *F* is a correction factor that accounts for the specific geometry of the heat exchanger, assumed equal to 1 in this study. Analogously, subscript "*h*" refers to the hot fluid conditions. Figure 3.14 shows a sketch of the heat exchanger with inlet/outlet hot/cold temperatures and flow directions.

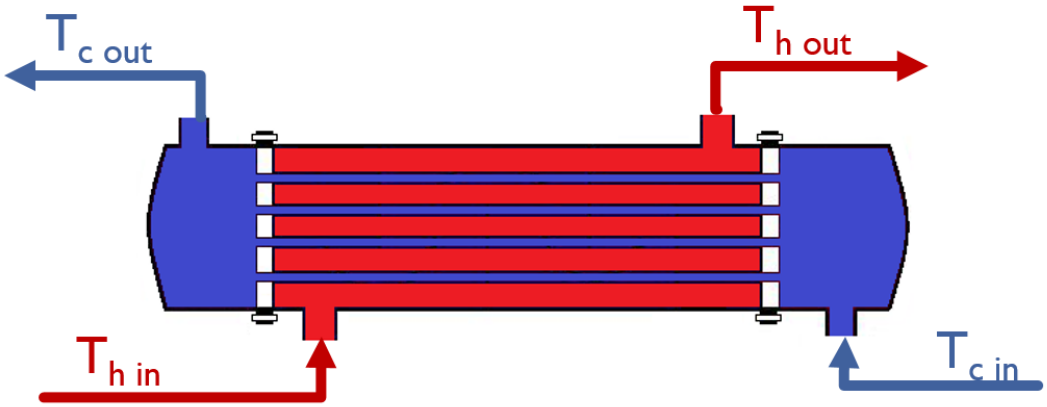

Figure 3.14: Counter-flow heat exchanger.

The global heat transfer coefficient, K_{tot}, is defined as

$$K_{tot} = \left[\frac{1}{\alpha_c} + \frac{s}{k_s} + \frac{1}{\alpha_h}\right]^{-1} \tag{3.11}$$

where α_c and α_h are the heat transfer coefficients for the cold and hot side, respectively, s is the tube wall thickness, and k_s is the tube thermal conductivity. The cold and hot flow heat transfer coefficients, α_c and α_h, depend on the Nusselt number, *Nu*, the characteristic linear dimension of the heat exchanger, *d*, and the fluid thermal conductivity, *k*, as given in the following equation

$$\alpha = Nu\frac{k}{d} \tag{3.12}$$

The Nusselt number is computed according to the physical state of the fluid, which, in this work, can be either subcritical or supercritical. Under subcritical flow conditions, the *Dittus–Boelter* correlation [30-32] is used

$$Nu = 0.023Re^{0.8}Pr^{n} \tag{3.13}$$

$$Re = \frac{\rho u d}{\mu} \tag{3.14}$$

In Eq. (3.13), *n* is a model parameter, equal to 0.3 and 0.4 for the fluid on the hot and cold side, respectively; *Re* is the Reynolds number, given by Equation (3.14), where ρ, *u*, and μ are the fluid density, velocity, and viscosity, respectively, and *Pr* is the Prandtl number.

Under supercritical flow conditions, the *Petukhov–Krillov* correlation, [33,34] given by Eqs. (3.15) and (3.16), is used

$$Nu = \frac{\left(\frac{\xi}{8}\right) Re\ Pr}{12.7\sqrt{\frac{\xi}{8}}(Pr^{2/3} - 1) + 1.07} \tag{3.15}$$

$$\xi = \frac{1}{(1.82\ log_{10}(Re) - 1.64)^2} \tag{3.16}$$

In this work, the supercritical flow correlation is applied only to the cold flow side because the exhaust gas pressure is set to 1.05 bar, largely below the critical pressure for all chemical species in the exhaust gas.

The exchanger area evaluation is performed in an iterative manner. The inlet water temperature is set to $T_{c_{in}} = 363\ K$, whereas the outlet water temperature is set to $T_{c_{out}} = T_{h_{in}} - \Delta T_{h_{in}}$, where $T_{h_{in}}$ is evaluated in the engine submodel and, as a first guess, $\Delta T_{h_{in}}$ is equal to 10 K. The water enthalpies at the inlet and outlet sections are computed by using CoolProp libraries [28] and, for a given water mass flow rate, the overall thermal power transferred from the hot fluid to the cold fluid is estimated by Eqs. (3.10). The heat exchanger is divided into 1000 elemental components, each of which exchanges $\Delta\dot{Q}$, equal to 1/1000 of the total thermal power. A single heat exchanger component is schematically shown in Figure 3.15.

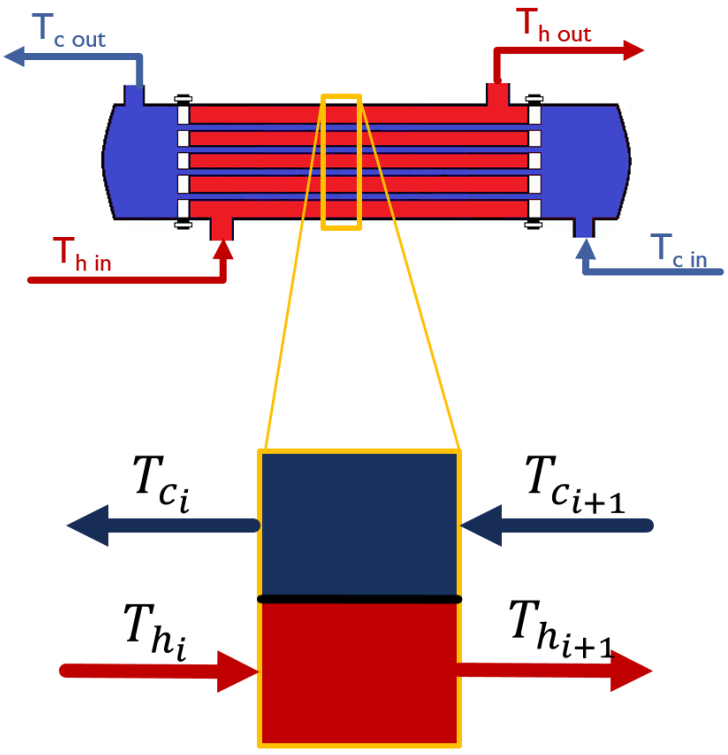

Figure 3.15: Elemental component of the heat exchanger.

In general, each component has its own size. The thermodynamic properties of the fluid, such as c_p, ρ and μ, are computed by using CoolProp libraries once the temperature of

each elemental component is known. The losses through the heat exchanger are accounted for in the loss term which is discussed in the following section.

Eqs. (3.10), for the generic heat exchanger *i-th* component, with area ΔA_i, is

$$\begin{cases} H_{c_{i+1}} = H_{c_i} - \dfrac{\Delta\dot{Q}}{\dot{m}_c} \\ T_{h_{i+1}} = T_{h_i} - \dfrac{\Delta\dot{Q}}{\dot{m}_h c_{p_h}} \\ \Delta A_i = \dfrac{\Delta\dot{Q}}{F K_{tot}} \left[\dfrac{ln\left(\dfrac{T_{h_i} - T_{c_i}}{T_{h_{i+1}} - T_{c_{i+1}}}\right)}{\left(T_{h_i} - T_{c_i}\right) - \left(T_{h_{i+1}} - T_{c_{i+1}}\right)} \right] \end{cases} \tag{3.17}$$

where c_{p_h} is the constant pressure specific heat of the hot fluid, T_{h_i} and $T_{h_{i+1}}$ are the inlet and outlet temperature, respectively, of the hot fluid flowing through the *i-th* element, and H_{c_i} and $H_{c_{i+1}}$ are the outlet and inlet enthalpy, respectively, of the cold fluid flowing through the *i-th* element.

The computation starts from the hot-fluid-entrance/cold-fluid exit side (left side of Figure 3.15) by solving, for the first elemental component, the system of Eqs. (3.17). For such equations, $\dot{m}_c$ is known based on W/F, whereas $\dot{m}_h$ and $T_{h_i} = T_{h_{in}}$ are computed in the engine submodel, $T_{c_i} = T_{c_{out}}$ and K_{tot} is computed from Eq. (2.11) with *s* = 1 mm and $k_s = 200\ W/(m\ K)$. The three unknowns of the system of equations are $H_{c_{i+1}}$, $T_{h_{i+1}}$, and ΔA_i.

For each component, the temperature difference between the hot and cold fluids cannot be less than a user defined ΔT_{pinch}, i.e., the allowed minimum temperature difference between the two fluids in the exchanger, equal to 10 K if not otherwise specified. For some configurations, the minimum temperature difference occurs at the exhaust gas entrance, i.e., $\Delta T_{h_{in}}$ is equal to ΔT_{pinch}. For some other configurations, the following condition may occur: $T_{h_{i+1}} < (T_{c_{i+1}} + \Delta T_{pinch})$. Then, the value of $\Delta T_{c_{out}}$ (which is the injection temperature) is increased and the numerical process is repeated for both the engine and the heat exchanger.

The computation ends as the cold side temperature $T_{c_{i+1}}$ reaches the cold side inlet temperature $T_{c_{in}}$. Finally, the heat exchanger total area is computed as the sum of the ΔA_i of each elemental component.

Engine–Heat Exchanger Coupling Model

The injection water temperature depends on the temperature of the exhaust gas. In turn, for a given amount of injected water, the gas temperature at the engine exhaust depends on the injection temperature. Therefore, for a given set of injection parameters, the injection temperature is not known a priori.

WISE starts with a first guess for the water injection temperature, and then the exhaust gas enthalpy at the end of a complete cycle (consisting of 5 engine cycles) is computed. To account for heat loss in the heat exchanger and in the manifold between the engine exhaust ports and the heat exchanger, the exhaust gas enthalpy is reduced by a fraction, equal to 20%, of the heat loss that would occur if the exhaust gas temperature had reached ambient conditions, i.e., T = 298 K. Then, the exhaust gas temperature $T_{h_{in}}$ is easily computed from the exhaust gas enthalpy and a new water injection temperature is computed $T_{w_{inj}} = T_{c_{out}} = T_{h_{in}} - \Delta T_{h_{in}}$. The process is repeated until the relative temperature difference between two subsequent iterations is less than 10^{-3} K.

Water Pumps Model

To accurately evaluate the overall system efficiency, the work required by the low-pressure and high-pressure pumps is computed as

$$W_p = m_{w_{inj}} \frac{(p_{out} - p_{in})}{\rho_w \eta_p} \tag{3.18}$$

where W_p is the work needed by each pump, $m_{w_{inj}}$ is the injected mass, p_{out} is the pressure at the pump outlet (5 bar for the low pressure pump and 230 bar for the high pressure pump), p_{in} is the pressure at the pump inlet (1 bar for the low pressure pump

and 5 bar for the high pressure pump), ρ_w is the water density (computed at the average pressure between p_{out} and p_{in}), and η_p is the pump efficiency, assumed equal to 0.85 for both pumps.

Injector Model

The mass flow rate computation has been slightly improved with respect to the model used for the first analysis presented in the previous paragraph. The injected mass flow rate, $\dot{m}_{w_{inj}}$, is computed by considering water as a real compressible gas. If the injection pressure/in-chamber pressure ratio is such that the injector works under choked conditions, the mass flow rate is obtained by using the following equation:

$$m_{w_{inj}} = C_d \frac{\pi d_{inj}^2}{4} \sqrt{\gamma \rho_w^{tot} p_w^{tot} \left(\frac{2}{\gamma+1}\right)^{\frac{\gamma+1}{\gamma-1}}} \tag{3.19}$$

where C_d is the injector discharge coefficient (set to 0.75), d_{inj} is the injector diameter, ρ_w^{tot} and p_w^{tot} are the injection total density and total pressure, respectively, and γ is the water specific heat ratio. The injector diameter and injection pressure are design parameters, whereas the injection total temperature depends on the exhaust gas enthalpy, as described in the previous section. Therefore, the WID is computed at each iteration as a function of the injection temperature.

If the flow is not choked, the mass flow rate is calculated by the following equation:

$$m_{w_{inj}} = C_d \frac{\pi d_{inj}^2}{4} \sqrt{\frac{2\gamma \rho_w^{tot} p_w^{tot} \left[\left(\frac{p}{p_w^{tot}} \right)^{\frac{2}{\gamma}} - \left(\frac{p}{p_w^{tot}} \right)^{\frac{\gamma+1}{\gamma}} \right]}{\gamma - 1}} \quad (3.20)$$

where p is the instantaneous in-chamber pressure.

3.2.2 Direct water injection system parametric analysis

With the direct water injection system mathematical model presented in section 3.2.1 it is possible to assess the maximum amount of wall heat transfer and exhaust gases energy recoverable, together with a more realistic understanding of the potential benefits obtainable with water injection. As described in section 3.4, an increase in W/F is beneficial to the system because the recovered heat increases with water mass, if temperature remains constant. On the other hand, an increase in W/F results in a lower exhaust gas temperature, due to the increased mass of the exhaust gas and to a higher engine efficiency, which reduces the recoverable thermal energy. In addition, a larger W/F increases the work needed by the pumps, as shown in Eq. (3.18). Based on these considerations, a parametric analysis is required to find the amount of supercritical water to be injected to maximize the overall system efficiency. In addition, simulations have been performed to evaluate the influence on the results of SOI and injector diameter.

Influence of W/F Ratio

Several simulations have been performed by using the engine specifications given in Table 3.2 with SOI equal to 35 CAD after top dead center (ATDC) and a 2.0 mm injector diameter. For these simulations, the combustion process is almost over at 35 CAD ATDC, i.e., about 99.3% of the total heat due to combustion has been released. Thus, the interaction of the injected supercritical water with the flame is negligible. In addition, the final stage of the combustion process takes place close to the cylinder liner, which is far from the injector location.

Simulations have been performed by varying W/F in the range 0–6 with increments of 0.006. For each case, the injection temperature has been computed. However, the simulation is stopped if supercritical conditions have not been reached. The efficiency of the system, ε_{sys}, is computed as the ratio between the net indicated engine work per cycle, W_e, reduced by the pumps work, W_{p1} and W_{p2}, and the total heat of combustion, Q_c

$$\varepsilon_{sys} = \frac{W_e - W_{p1} - W_{p2}}{Q_c} \tag{3.21}$$

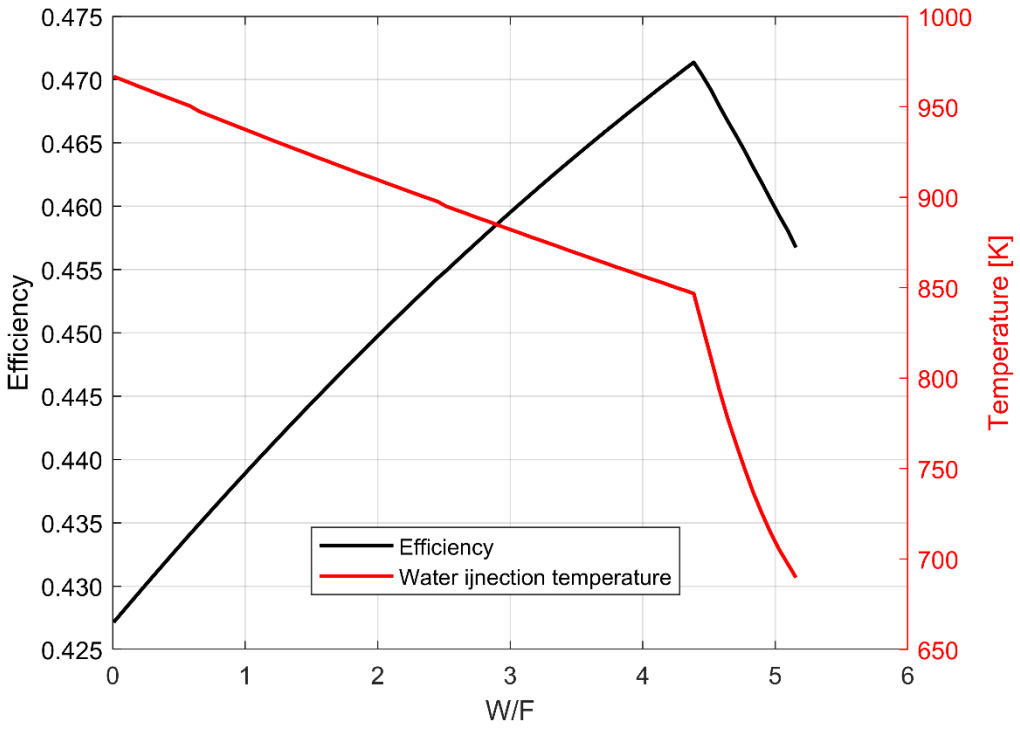

Figure 3.16: Overall system efficiency and injection temperature as a function of W/F (SOI = 35 CAD ATDC, d_{inj} = 2 mm).

Figure 3.16 shows the efficiency of the overall recovery system and the water injection temperature as a function of W/F. The efficiency reaches a maximum value of 0.471 with W/F = 4.39. This value has been selected for the baseline case, whose specifications are shown in Table 3.8. In what follows, if not otherwise specified, the injection parameters are set as for the baseline case. The efficiency gain is +10.3% with respect to the same engine but without water injection. The supercritical water injection temperature decreases by increasing W/F because a larger amount of water needs to be heated in the exchanger. In addition, an increased mass of injected water increases the exhaust gas mass flow rate, thus reducing the exhaust gas temperature, which, in turn, reduces the water injection temperature. For the baseline case, the injection temperature is equal to 846.8 K and WID is 6.54 CAD.

Table 3.8. Baseline case: injection parameters.

SOI	35 CAD after TDC
Injector diameter	2.0 mm
W/F	4.39

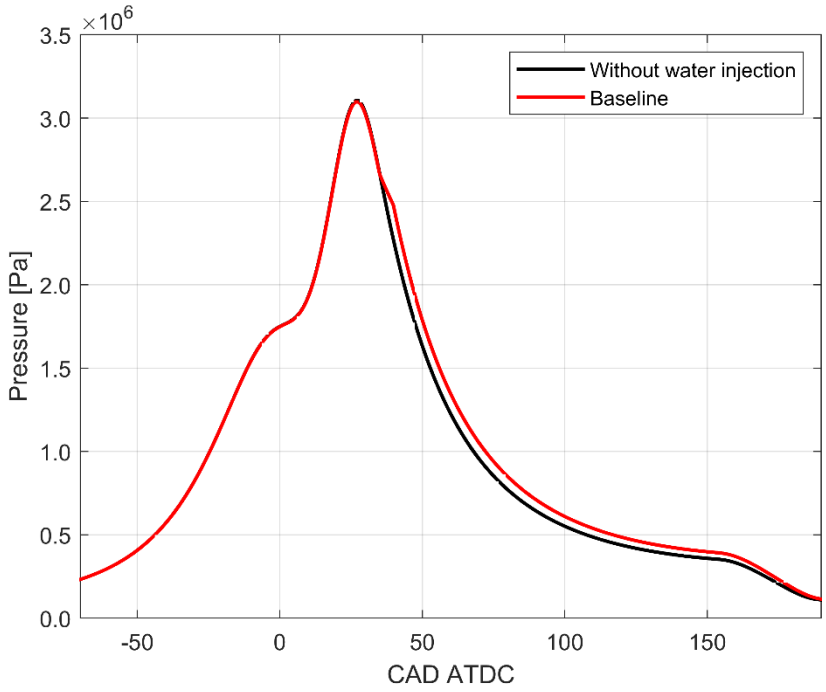

Figure 3.17: In-cylinder pressure traces for the baseline case and for the case without water injection.

Figure 3.17 compares the results with and without water injection, in terms of in-cylinder pressure. The figure shows that, during the expansion stroke, higher pressure is obtained with water injection, leading to an increase in the engine power output. Figure 3.16 shows a sudden decrease in the system efficiency at W/F = 4.39. To explain this decrease, Figure 3.18A shows the total amount of heat recovered with the exhaust gas and wall heat transfer contributions, as a function of W/F, and Figure 3.18B shows $\Delta T_{h_{in}}$ as a function of W/F. Now, as W/F increases from 0 to 4.39, an increase in the heat recovered, which results in a higher efficiency, is observed, and the hot and cold fluid thermodynamic conditions are such that the heat exchanger works with $\Delta T_{h_{in}}$ equal to 10 K. But, with a further increase in W/F above 4.39, the heat recovered from engine walls, which is a minor part of the total recovered heat, increases, whereas the amount of recovered heat from exhaust gas and the total amount of recovered heat decreases. This is reason why $\Delta T_{h_{in}}$ is no longer equal to 10 K. This results in a sudden decrease in the injection temperature ($T_{w_{inj}} = T_{c_{out}} = T_{h_{in}} - \Delta T_{h_{in}}$), which reduces the gas temperature at the engine exhaust with a reduction of the injection water temperature. Indeed, as the heat exchanger water inlet temperature $T_{c_{in}}$ is set to 363 K, for a given W/F the heat recovery from the exhaust gas is only a function of the injection temperature, which decreases if $\Delta T_{h_{in}}$ increases. Therefore, the heat contribution from the exhaust gas decreases as $\Delta T_{h_{in}}$ increases because the effect of water injection temperature reduction prevails on the increased amount of water mass, as shown in Figure 9A. The final result is a reduction of both the total heat recovered and the system efficiency.

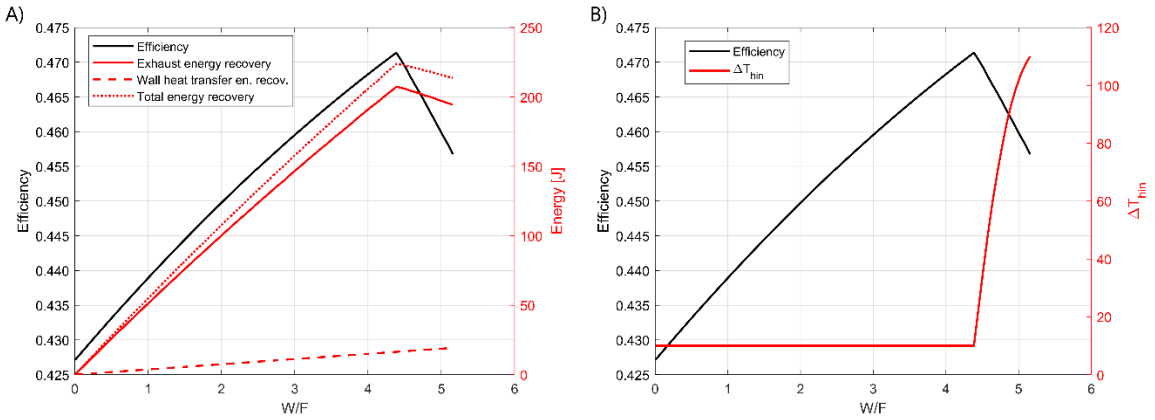

Figure 3.18: A) System efficiency and energy recovery and B) $\Delta T_{h_{in}}$ as a function of W/F (SOI = 35 CAD ATDC, d_{inj} = 2 mm).

To confirm this, Figure 3.19 shows the water and the exhaust gas temperature profiles along the heat exchanger for W/F = 4.32 and W/F = 4.45. Specifically, Figure 3.19B shows that a small W/F increment (from 4.32 to 4.45) results in a high injection temperature drop. The same figure shows that the pinch point occurs at the exhaust gas inlet side with W/F = 4.32, whereas the pinch point moves inside of the heat exchanger with W/F = 4.45, as shown in Figure 3.19C. It can be concluded that, if $\Delta T_{h_{in}}$ is not equal to ΔT_{pinch}, a drastic reduction of the overall efficiency gain is observed.

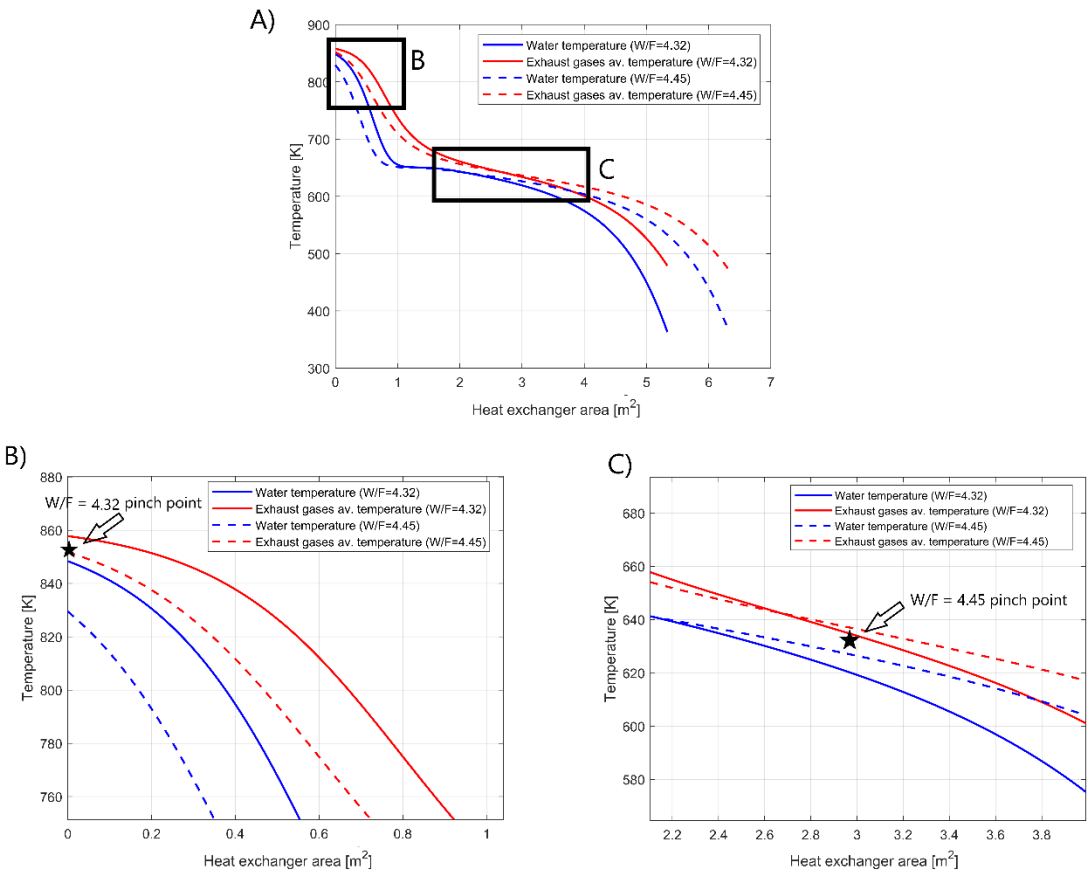

Figure 3.19: A) Heat exchanger temperature profiles, B) exhaust gas inlet blowup, and C) inside section blowup for the cases W/F = 4.32 and W/F = 4.45 (SOI = 35 CAD ATDC, d_{inj} = 2 mm).

Influence of SOI

Figure 3.20 shows the overall system efficiency as a function of W/F for different SOI, i.e., 30, 35, and 40 CAD ATDC. At 30 CAD ATDC, the combustion process is almost completed, i.e., 93.1%; thus, the water injection/flame interaction is negligible. An early water injection, closer to TDC, results in a higher efficiency gain because the increase in the in-chamber pressure occurs earlier [35]. Table 3.9 shows the optimal values of W/F, the efficiency and the percentage efficiency gain with respect to the case without water injection, and the injection water temperature and WID. An SOI closer to TDC results in a higher efficiency gain and lower W/F, injection temperature, and WID. The higher efficiency with earlier SOI is due to an earlier and higher increase in in-chamber pressure, which results in an increase in the engine work. On the contrary, as the efficiency increases, more heat is converted into work, thus less heat is available within the exhaust gas, which upper bounds the optimal W/F and the injection water temperature. Figure 3.21 shows the influence of SOI on the engine working cycle with the optimal value of W/F.

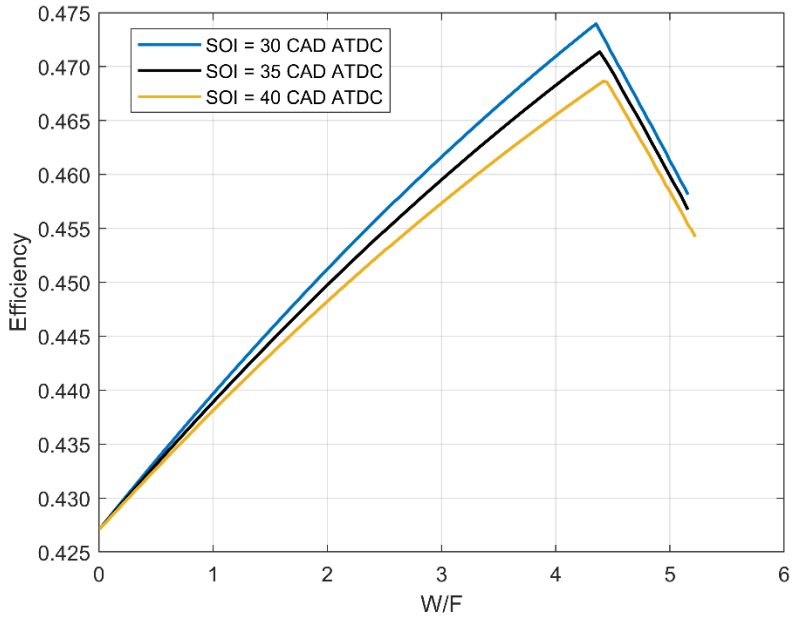

Figure 3.20: Overall efficiency as a function of W/F for different SOI (d_{inj} = 2 mm).

Table 3.9. Optimal solutions for different SOI (d_{inj} = 2 mm).

SOI [CAD]	W/F	Efficiency (% gain)	$T_{w_{inj}}$ [K]	WID [CAD]
30	4.35	0.474 (+11.0%)	843.8	6.47
35	4.39	0.471 (+10.3%)	846.8	6.54
40	4.42	0.469 (+9.8%)	849.6	6.61

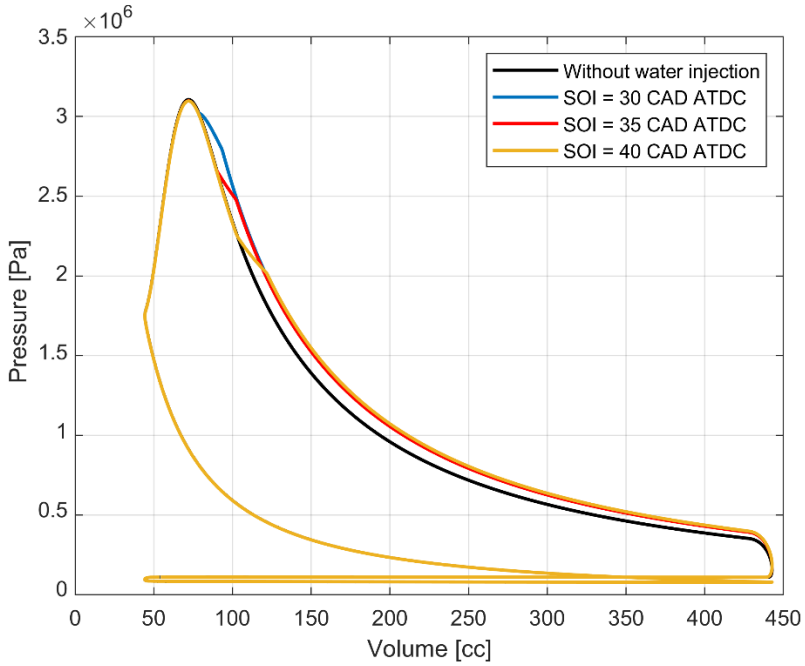

Figure 3.21: In-chamber pressure versus engine volume for the optimal configurations with different SOI (d_{inj} = 2 mm) and for the case without water injection.

Influence of Injector Diameter

A larger injector equivalent diameter results in a shorter WID for a given injected water mass. This results in a higher efficiency gain, due mainly to a higher in-chamber pressure with a shorter WID. The optimal W/F has been evaluated for different injector diameters, i.e., 1, 2, and 4 mm, and the system overall efficiency as a function of W/F is shown in Figure 3.22. A higher increase in the efficiency gain is obtained as the injector diameter increases from 1 to 2 mm. This suggests that a diameter equal to 2 mm is a good choice for both the system efficiency and the injector geometry. Table 3.10 shows, for the three injector diameters, the optimal W/F, the efficiency gain with respect to the case without water injection, the injection temperature, and WID. Finally, Figure 3.23 shows the influence of the injector diameter on the engine working cycle with the optimal W/F for each case. The figure clearly shows a lower efficiency gain as the injector diameter increases from 2 to 4 mm.

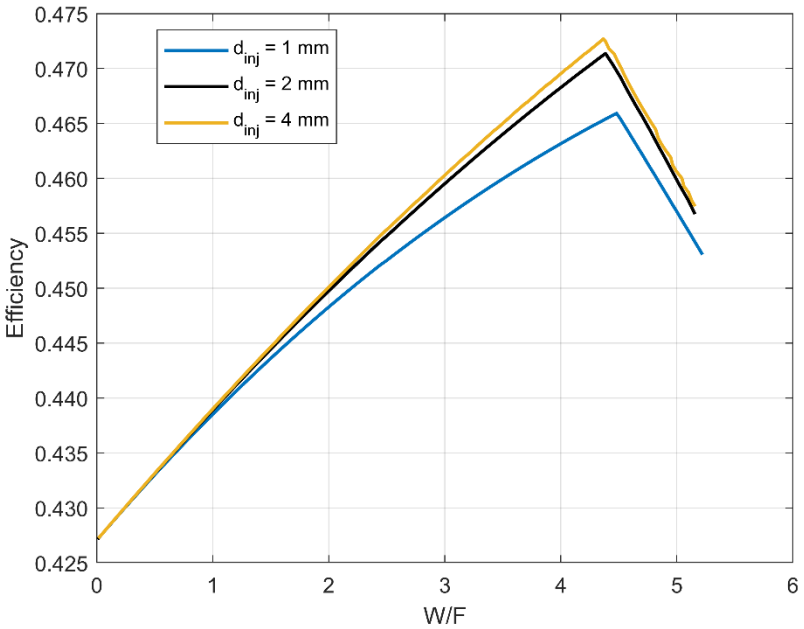

Figure 3.22: Overall efficiency as a function of W/F for different d_{inj} (SOI = 35 CAD ATDC).

Table 3.10. Optimal solutions for different d_{inj} (SOI = 35 CAD ATDC).

d_{inj} [mm]	W/F	Efficiency (% gain)	$T_{w_{inj}}$ [K]	WID [CAD]
1	4.45	0.466 (+9.1%)	851.8	26.9
2	4.39	0.471 (+10.3%)	846.8	6.54
4	4.37	0.471 (+10.8%)	845.6	1.63

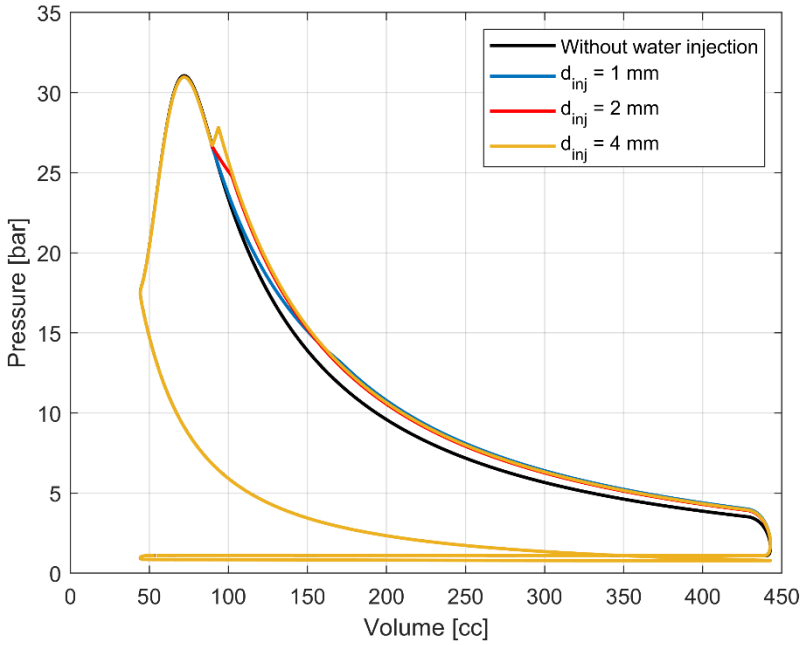

Figure 3.23: In-chamber pressure versus engine volume for the optimal configurations with different d_{inj} (SOI = 35 CAD ATDC) and for the case without water injection.

Influence of Wall Heat Loss Reduction

Based on the parametric analysis, the maximum increase in the system efficiency, i.e., 11.0%, is reached with an SOI equal to 30 CAD ATDC, an injector diameter of 2 mm, and a W/F of 4.35. However, under these circumstances, the water mass flow rate is not sufficient for cooling the engine and a supplementary cooling circuit is required. Thus, the heat through engine walls cannot be completely recovered. In recent years, many studies have focused on the reduction of engine wall heat loss by using, for example, combustion chamber insulation strategies [36-41]. If such strategies are used, the engine efficiency with supercritical water injection may increase, due to the higher amount of heat available within the engine exhaust gas, thus resulting in a higher W/F. To investigate the impact of wall heat transfer on the efficiency gain of the system, wall heat loss has been reduced by 10% by reducing the a model constant of the Annand correlation (Eq. (3.6)) from 0.40 to 0.17. The results are shown in Figure 3.24, where the system efficiency is given as a function of W/F and compared with the baseline case. As expected, the injection of supercritical water into a partially insulated engine chamber increases the system efficiency. This is shown in Table 3.11, which gives the optimal W/F, the system efficiency, the efficiency gain with respect to the corresponding case without water injection, the injection temperature, and WID for the reference engine and the partially insulated engine. A reduction of the wall heat loss results in a higher system efficiency because more heat from the exhaust gas is recovered and reintroduced into the combustion chamber. It can be concluded that it is beneficial to gather the heat recovery system with a strategy to reduce heat loss through engine walls.

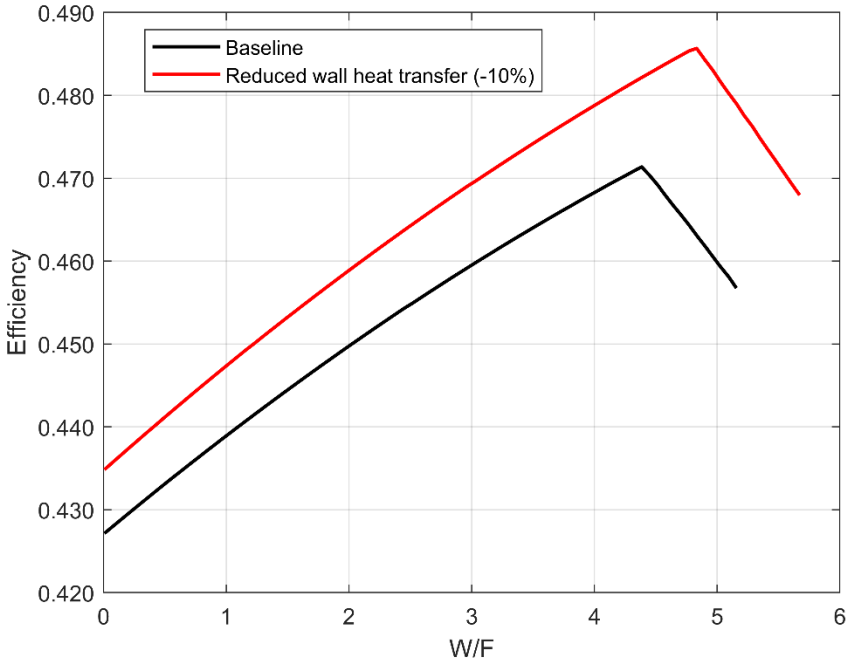

Figure 3.24: Overall efficiency as a function of W/F: influence of heat loss through engine walls.

Table 3.11. Optimal solutions for the baseline case and the partially insulated engine.

	W/F	Efficiency (% gain)	$T_{w_{inj}}$ [K]	WID [CAD]
Baseline	4.39	0.471 (+10.3%)	846.8	6.54
Reduced wall heat loss (-10%)	4.83	0.486 (+11.7%)	868.7	7.34

Influence of Exhaust Gas Energy Loss

As shown in Figure 3.18A, most of the recovered heat comes from the exhaust gas. A fraction of such heat is released to the environment in the exhaust manifold between the exhaust ports and the heat exchanger. Such a fraction depends on the geometry and material of the exhaust manifold and on other components placed before the heat exchanger, such as a particulate filter. An estimate of the impact of such loss on the efficiency of the system has also been addressed. In all the simulations discussed so far, an exhaust gas heat loss of 20% has been assumed between the engine exhaust ports and the heat exchanger entrance. Additional computations with exhaust gas heat loss of 15% and 25% have been performed. Figure 3.25 shows the system efficiency as a function of W/F by varying the amount of exhaust gas heat loss, whereas Table 3.12 shows the optimal values of W/F, the system efficiency, the efficiency gain with respect to the case without water injection, the injection temperature, and WID for the three cases. The results show a very high impact of the exhaust gas heat loss on the efficiency gain. Indeed, with a loss of 15%, the system efficiency gain increases up to 12.2%. It can

be concluded that it is demanding to consider a strategy for the reduction of such a loss in the system design process.

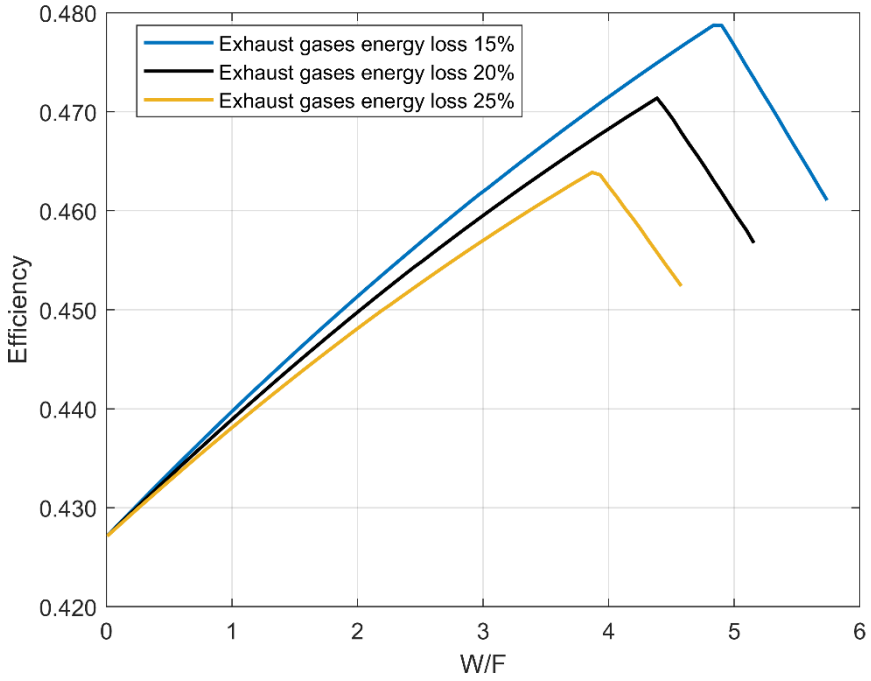

Figure 3.25: Overall efficiency as a function of W/F: influence of exhaust gas heat loss through manifolds.

Table 3.12. Optimal solutions for different d_{inj} (SOI = 35 CAD ATDC).

Exhaust gas energy loss	W/F	Efficiency (% gain)	$T_{w_{inj}}$ [K]	WID [CAD]
15%	4.84	0.479 (+12.2%)	875.3	7.41
20%	4.39	0.471 (+10.3%)	846.8	6.54
25%	3.87	0.464 (+8.7%)	820.1	5.61

Influence of injection pressure

The choice of injecting water under supercritical conditions enables to have a high-density fluid, in order to have a short WID and to reduce the size of the injector, which, if not small enough, may not fit on the engine head. From a theoretical perspective, an instantaneous injection would result in the maximum achievable in-chamber pressure gain, which, in turn, would give the maximum increase in terms of efficiency. On the other hand, since the injected water vapor is assumed to be a real gas, its thermodynamic properties are pressure dependent.

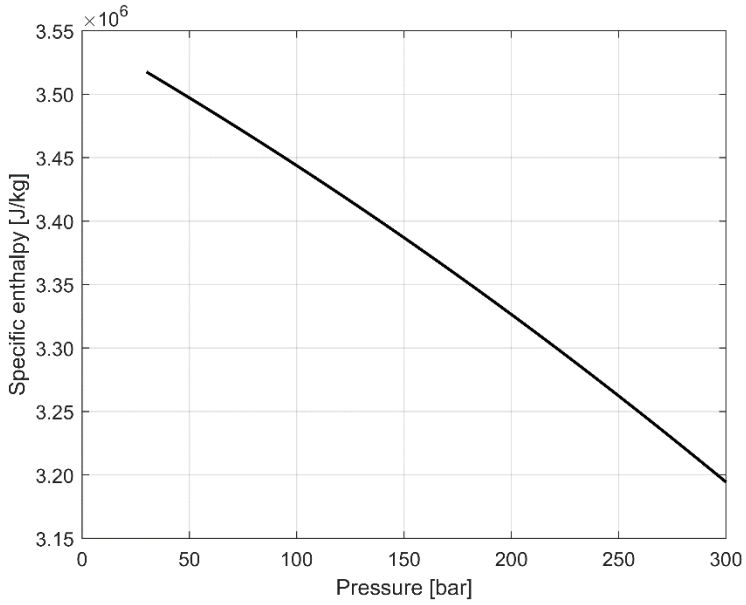

Figure 3.26: Water specific enthalpy as a function of pressure at 800 K.

Figure 3.26 shows water specific enthalpy as a function of pressure at 800 K. The graph shows that an increase of the injection pressure results in a lower specific enthalpy, which, for a given injected mass, results in a lower amount of internal energy introduced into the combustion chamber. Therefore, it cannot be concluded a priori if a higher injection pressure is beneficial in terms of system efficiency gain. In order to determine the optimal injection pressure, a parametric study has been carried out. Since the in-chamber pressure at 35 CAD ADTC is 26.6 bar for the baseline case, the parametric analysis starts with an injection pressure of 30 bar and ends at 280 bar, with an increment of 10 bar. Hence, superheated steam has also been considered along with supercritical water vapor. For each injection pressure, the optimal values of injection temperature and W/F have been determined. The results are summarized in Figure 3.27. The figure shows that, in the range 30~90 bar, increasing the injection pressure results in a higher efficiency system. In other terms, in this range the benefit due to the shorter injection duration, obtained with a higher injection pressure, prevails over the lower water specific enthalpy, which is shown in Figure 3.27. The injection pressure of 90 bar returns the maximum system efficiency of 0.475 (with a gain of +11.2% respect to the same case without water injection), with a WID of 18.0 CAD, a water injection temperature of 858.2 K and a W/F of 4.47. This efficiency gain is comparable with that obtained by using supercritical water with SOI = 30 CAD ATDC and d_{inj} = 2mm. In the latter case, however, the amount of injected water and the injection temperature are less, with W/F equal to 4.35 and $T_{w_{inj}}$ = 843.8 K. Finally, a further increase of water injection pressure results in a lower efficiency, since a lower water specific enthalpy prevails over a shorter WID.

The choice of the injection pressure should not be limited only to thermodynamic considerations, since it will also influence wall heat transfer, the jet/flame interaction (which could either enhance combustion or quench the flame) and the injector size and

geometry. These aspects need a dedicated investigation, which will not be part of the present work, where a supercritical pressure will be considered, in order to have injection fluid characteristics as close as possible to the fluids that are currently injected into internal combustion engines.

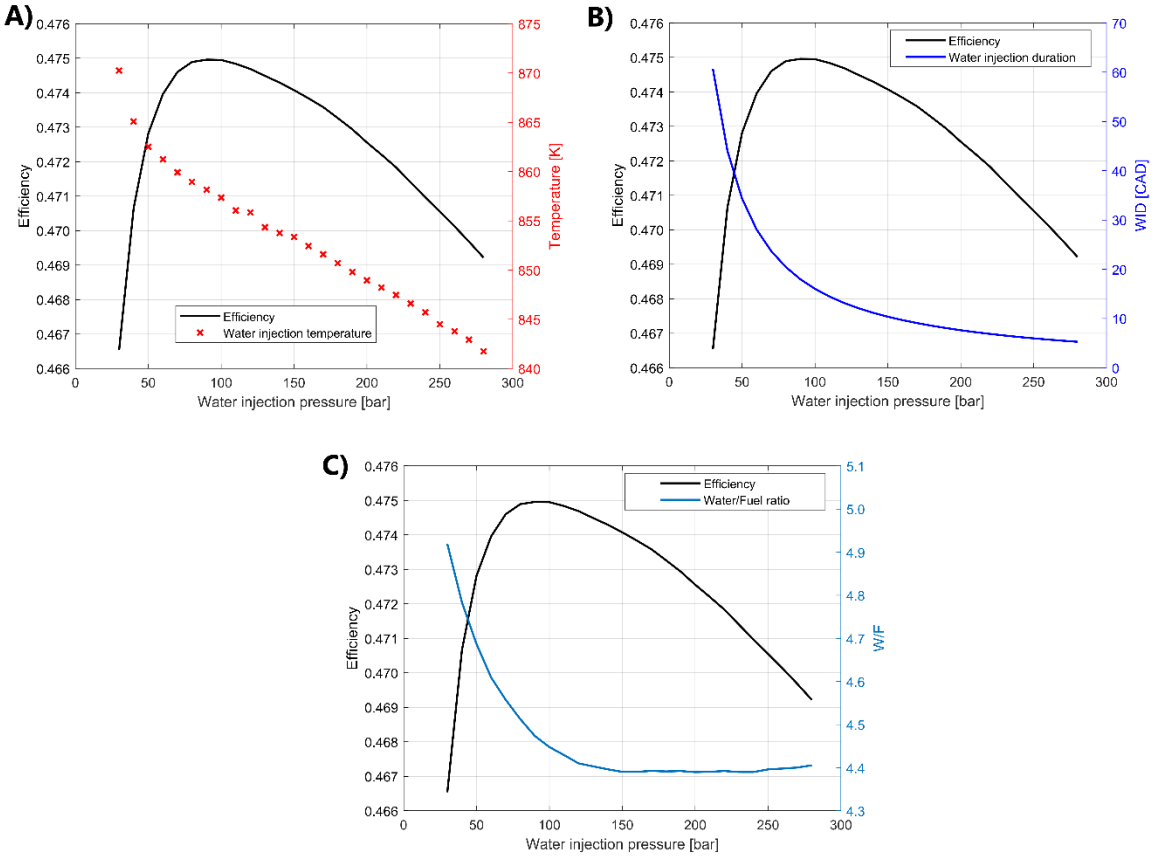

Figure 3.27: Optimal system efficiency and A) water injection temperature B) WID, and C) W/F as a function of injection pressure (SOI = 35 CAD ATDC, d_{inj} = 2 mm).

3.2.3 Direct water injection system optimization

Single-objective optimization

The parametric analysis shown in section 3.2.2 showed the optimal W/F values varying one injection parameter and keeping constant the others. A single-objective GA has been coupled to the WISE solver to search for a global optimum of the overall system efficiency by varying the injection parameters, i.e., SOI, injector diameter, and W/F. The GA variables have been constrained within specific ranges based on the results of the previous parametric analysis. Indeed, SOI varies between 30 CAD ATDC and 40 CAD ATDC. Earlier injections are not considered to not take into account the water injection/flame interaction. On the contrary, a further delay of water injection timing

would be not useful to optimize the system efficiency. The W/F ranges between 0.64 and 5.15 because, as previously shown, the maximum efficiency gain is always within such limits for all cases. The injector diameter ranges between 1 and 4 mm. Based on practical considerations, the optimal solution is expected to be found within these limits. Such constraints are shown in Table 3.13. The GA has been applied by using a population of 40 individuals, which turns out to be sufficiently large to obtain the global optimum. The optimization procedure ends when the best fitness function value does not change for at least 50 generations. The convergence criterion is reached after 101 generations, as shown in Figure 3.28. The best individual has an overall efficiency of 0.475 (+11.2% with respect to the same engine without water injection), with W/F, SOI, and d_{inj} equal to 4.90, 30.8 CAD ATDC, and 3.94 mm, respectively. This result clearly suggests that an SOI closer to TDC and an injector with a relatively large diameter provide the maximum increase of the system efficiency.

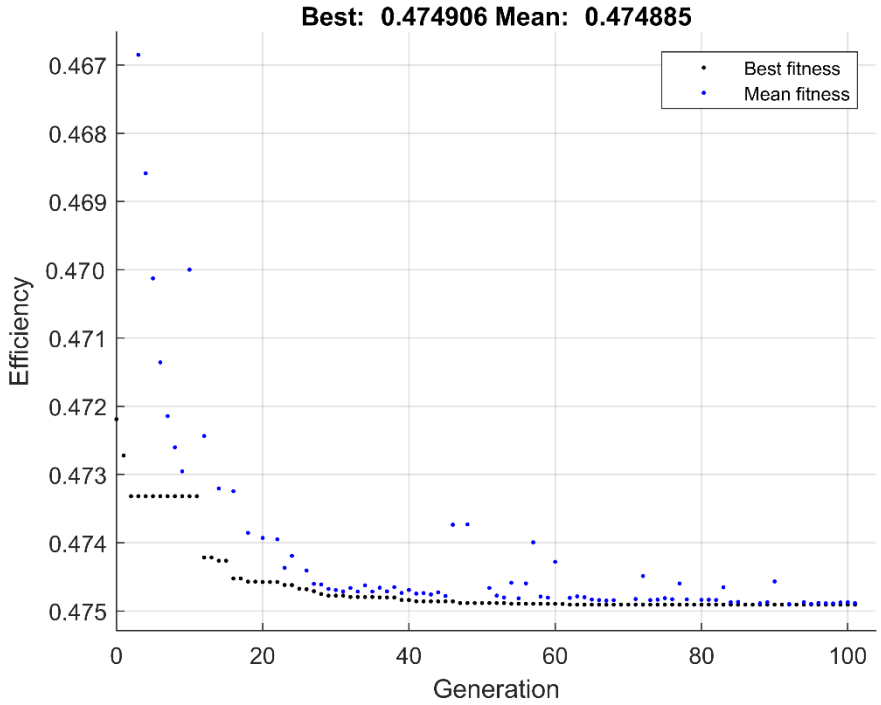

Figure 3.28: Single-objective GA convergence history (descending order on y-axis).

Table 3.13. Single objective GA constraints.

	Lower bound	Upper bound
W/F ratio	0.64	5.15
SOI (CAD ATDC)	30	40
Injector diameter [mm]	1.0	4.0

Multi-objective optimization

For automotive applications, the heat exchanger plays a fundamental role in terms of cost and size. Therefore, the system design should return a good compromise between efficiency gain and heat exchanger size. This issue has been investigated by using a multi-objective GA with the system efficiency and the exchange surface of the heat exchanger as objective functions. The objective functions depend on the injection parameters, i.e., W/F, SOI, and d_{inj}, and are computed by WISE. The GA constraints have been set up as in the single-objective optimization, whereas the population has been set to 300 individuals to achieve accurate results. Figure 3.29 shows the Pareto front. As the system efficiency approaches 0.475, the Pareto front reaches an asymptote, with an oversized heat exchanger. Thus, from a practical perspective, solutions beyond this value should be avoided. On the contrary, the efficiency decreases with the heat exchanger size and approaches the efficiency obtained without injection. The optimal solution is a compromise between the two objectives and depends on the specific application. The set of injection parameters corresponding to three values of efficiency on the Pareto front, i.e., 0.470, 0.465, and 0.460, have been selected and are shown in Table 3.14. The results confirm that, to get the maximum system efficiency, a large injector diameter and an SOI close to TDC should be selected. Moreover, the heat exchanger size mainly depends on the amount of injected water.

Table 3.14. Multi-objective GA: Pareto front analysis. The efficiency gain percentage is computed with respect to the same engine without water injection.

	Efficiency 0.470 (+10.1%)	Efficiency 0.465 (+8.9%)	Efficiency 0.460 (+7.7%)
Heat exchanger area [m^2]	2.58	1.60	1.12
W/F ratio	3.79	3.27	2.82
SOI (CAD ATDC)	30.1	30.5	30.8
Injector diameter [mm]	3.92	3.91	3.89

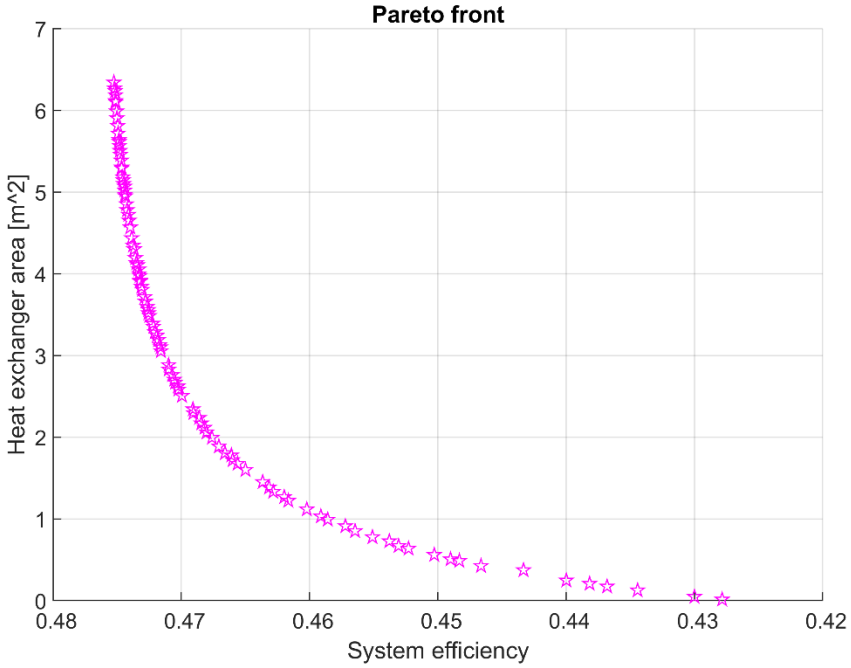

Figure 3.29: Multi-objective GA Pareto front (descending order on x-axis).

Single-objective GA: injection pressure optimization

The single-objective GA optimization discussed in the previous section was done with a constant injection pressure of 230 bar. Since the overall efficiency gain also depends on the injection pressure, the genetic algorithm has been employed to take into account this additional parameter together with the W/F ratio, the injector diameter and the SOI. Table 3.15 summarizes the GA constraints, while Figure 3.30 shows the convergence history (population size: 50 individuals). The objective function of the optimization is to maximize the overall system efficiency, as defined in Eq. (3.21).

Table 3.15. Single objective GA constraints (injection pressure optimization).

	Lower bound	Upper bound
W/F ratio	0.64	5.15
SOI (CAD ATDC)	30	40
Injector diameter [mm]	1.0	4.0
Injection pressure [bar]	30	300

Figure 3.30 shows the convergence history. The efficiency maximum is found with an injection pressure of 54.7 bar. The optimal solution has an efficiency of 0.484 (+13.4% respect to the case without water injection), an injection temperature of 851.7 K, a WID of 7.48 CAD, a W/F ratio of 4.5, an injector diameter of 4 mm and a SOI of 30.0 CAD. The efficiency obtained with the subcritical injection pressure of 54.7 bar is higher than all previous cases, being equal the engine wall heat transfer and the energy loss between the exhaust valve and the heat exchanger inlet. Thus, the subcritical direct water

injection should be further explored, since it may result in a higher efficiency gain. Nonetheless, the lower injection pressure may produce technical issues on the injector, which must operate with a lower density fluid and remain open for a longer period of time.

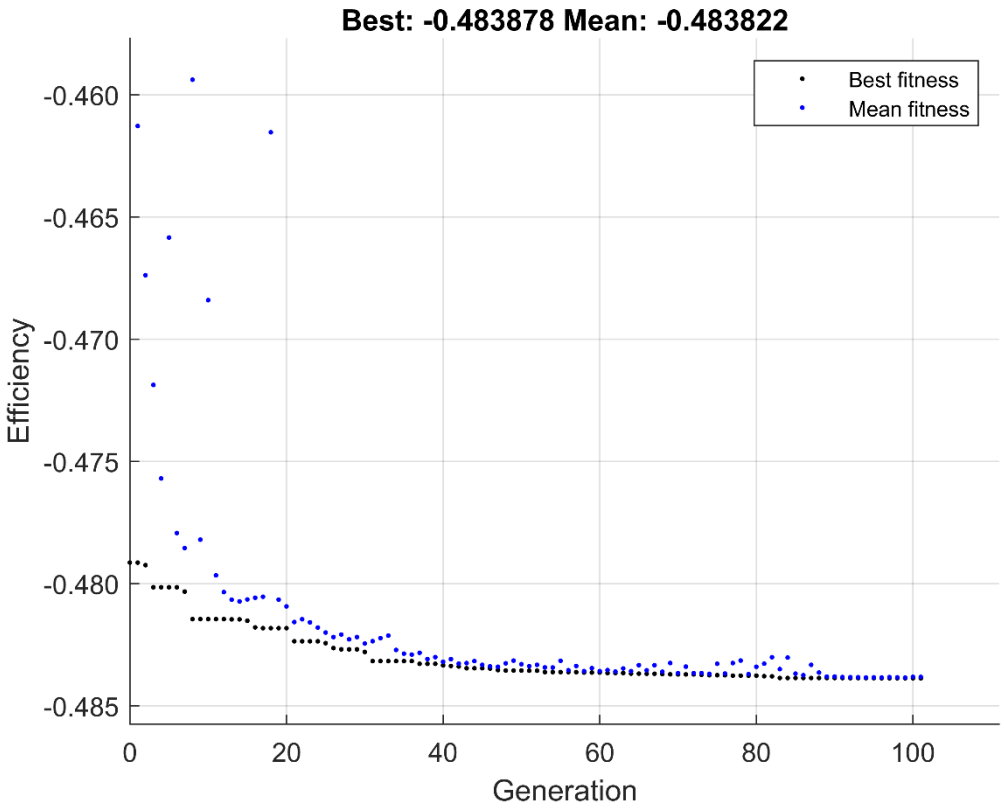

Figure 3.30: Single-objective injection pressure optimization convergence history (descending order on y-axis).

Chapter 4

Supercritical water direct injection: RANS simulations with the ECFM Model

4.1 Direct water injection: 2D CFD modelling using the ECFM

In order to assess the reliability of the quasi-dimensional model used for the analysis presented in the previous sections and to have a more accurate assessment of the engine performance, a 2D CFD model of the engine used as reference for the quasi-dimensional analysis [29] has been developed using Ansys® Fluent. In order to reduce the computational time, the simulations start at intake valve closing (IVC = -144 CAD ATDC) and end at exhaust valve opening (EVO = 153 CAD ATDC).

4.1.1 Engine geometry

Even if the actual engine combustion chamber is three-dimensional, an axisymmetric computational domain has been considered for the simulations in order to drastically reduce the computational time. As shown in Figure 4.1, the combustion chamber geometry is characterized by a flat piston, whereas the cylinder head presents a shape with a slight slope. The axisymmetric domain has been selected among several different shapes, obtained by varying the angle α of Figure 3.31, as the one that better matches the heat release rate and pressure trace of the actual engine. This parametric analysis will be given in the *Model validation* section.

In this first simulation, an axial water injector has been chosen, which has been schematically represented in Figure 4.1. This specific convergent-divergent geometry allows both to include the effects of the laminar sub-layer at the injector walls and to get

a more accurate representation of the water jet velocity profile at the injector exit. The axial location of the injector is required, once again, to guarantee the axial symmetry of the geometry. The specific dimensions of the injector used in the simulations are: 2 mm throat diameter, 6 mm inlet diameter and 2.2 mm outlet diameter.

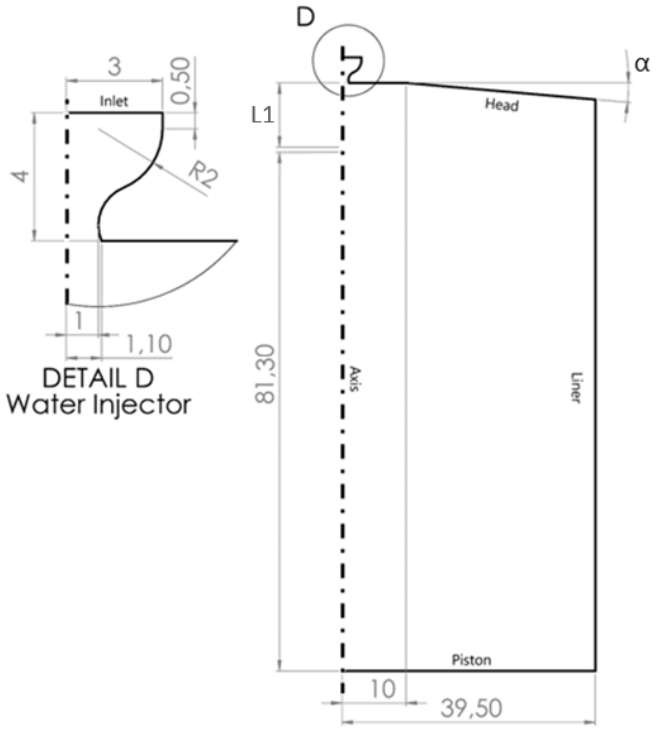

Figure 4.1: Chamber axisymmetric geometry. The length L1 depends on the angle α

4.1.2 Computational domain

The domain and details of the mesh are shown in Figure 3.32. A structured grid has been used for the combustion chamber with numerical cells that are squares with 0.125 mm sides, except near the cylinder head, where the cells are quadrilaterals, but not squares. Specifically, the region with perfectly square elements goes from the piston up to a distance of 81.8 mm at the start of the computations. On the boundary between the injector exit and the engine head, the grid size is set to 0.05 mm in order to get an accurate velocity profile at the injector exit. Since a turbulence model with wall functions is employed, the y^+ value must be high enough on the second numerical cell away from the wall boundaries. The chosen grid is the most refined grid that ensures such a condition. Besides, the main features of an under-expanded jet are correctly captured, as specified in the results section, thus assessing the accuracy of the grid resolution for the computations.

As regards the injector, an unstructured grid has been selected in order to guarantee an accurate representation of the geometry. Most of the numerical cells are regular quadrilaterals with 0.05 mm side, some are triangular elements.

The layering method is used to adjust the grid during the piston motion. Specifically, the layering has been set on the interface between the second and the third cell row, starting from the piston wall, as shown in Figure 4.2C. This avoids a variable length of the cells at the wall, where a wall function model is used. The axial dimension of the variable length cells row is being reduced until it reaches a size of 0.4 times its original length during the compression stroke, while it is increased until it reaches a size of 1.4 times its original length during the expansion stroke.

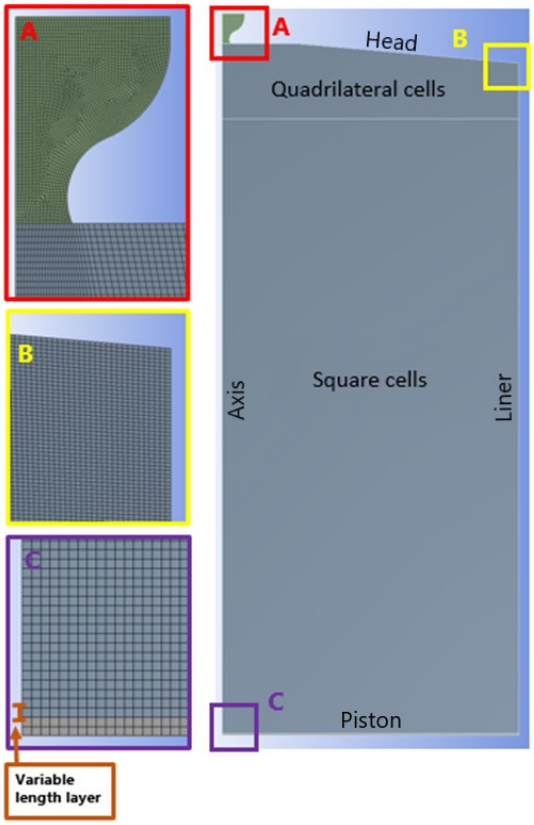

Figure 4.2: Computational grid details.

4.2.3 CFD models

The Unsteady Reynolds-Averaged Navier-Stokes (U-RANS) equations for a multicomponent, reacting, turbulent gas mixture are solved. Turbulence is modeled with the standard k-ε model and standard wall functions [42]. The wall heat transfer has been considered up to the time when water injection starts. A standard wall functions model has been used. In the following subsections, a description of the combustion, ignition and water injection models are provided. All the simulations have been performed using

Ansys® Fluent Student, Release 19.2. Further details about the models can be found in the Ansys® Fluent Theory Guide [43].

The *Extended Coherent Flamelet Model* (*ECFM*) [44] has been used to model the combustion process. The ECFM model is based on the *c-equation* model, which assumes that the flame front propagates from the burned gases, where the reaction progress variable *c* is equal to 1, towards the unburned gases (*c* = 0). The reaction progress variable is defined as:

$$c = \frac{\sum_{i=1}^{NS} \alpha_k \left(Y_k - Y_k^u\right)}{\sum_{i=1}^{NS} \alpha_k \left(Y_k^{eq} - Y_k^u\right)} \tag{4.1}$$

where *NS* is the number of the chemical species, the superscript *u* denotes the unburnt reactant, Y_k denotes the *k-th* species mass fraction, Y_k^{eq} denotes the *k-th* species mass fraction at chemical equilibrium, α_k are equal to 1 for product species and to zero for reactants. The flame front propagation is modeled by solving the transport equation for the reaction mean progress variable $\bar{c}$:

$$\frac{\partial}{\partial t}(\rho\bar{c}) + \nabla \cdot (\rho\vec{u}\bar{c}) = \nabla \cdot \left[\left(\frac{k_c}{C_p} + \frac{\mu_t}{Sc_t}\right)\nabla\bar{c}\right] + \rho Sc \tag{4.2}$$

where:

ρ = density

$\vec{u}$ = velocity

μ_t = turbulent viscosity

Sc_t = turbulent Schmidt number

Sc = reaction progress source term

k_c = thermal conductivity of the gas mixture

C_p = gas mixture specific heat.

The ECFM model differs from the *c-equation* model mainly in modeling the reaction progress source term. Indeed, in Eq. (4.2) the term ρSc is replaced by $\rho_u S_L \Sigma$, where S_L is the mixture laminar flame speed and Σ is the flame area density. Therefore, an additional equation for the flame area density transport is needed, which reads:

$$\frac{\partial\Sigma}{\partial t} + \nabla \cdot (\vec{u}\Sigma) = \nabla \cdot \left[\left(\frac{k_c}{C_p} + \frac{\mu_t}{Sc_t}\right)\nabla \cdot \left(\frac{\Sigma}{\rho}\right)\right] + (P_1 + P_2 + P_3)\Sigma + P_4 - D \tag{4.3}$$

where four Σ source terms (P_1, P_2, P_3, P_4) and one dissipation term (D) are present, which need closure models. In the present work, the closure terms proposed by Poinsot [44] have been used, which read:

$$P_1 = \alpha_1 K_t, \tag{4.4}$$

$$P_2 = \frac{2}{3}\frac{\alpha_2}{\rho}\nabla(\rho\vec{u}), \tag{4.5}$$

$$P_3 = \alpha_3 \frac{\rho_u}{\rho_b} S_L \frac{1-\bar{c}}{\bar{c}}\Sigma, \tag{4.6}$$

$$P_4 = 0, \tag{4.7}$$

$$D = \beta_1 S_L \frac{\Sigma^2}{1-\bar{c}}, \tag{4.8}$$

where K_t is the turbulent time scale, ρ_u is the unburned mixture density, ρ_b is the burned mixture density, S_L is the mixture laminar flame speed. The values of the model constants α_1, α_2, α_3 and β_1 are listed in Table 4.1.

Table 4.1: Model constants values for ECFM Poinsot closure terms.

	α_1	α_2	α_3	β_1
Poinsot [44]	1.6	1.0	1.0	1.0

The turbulent time scale K_t is determined as:

$$K_t = \frac{\varepsilon}{k}[(1-\alpha_0) + \alpha_0\Gamma_K], \tag{4.9}$$

where ε is the turbulent dissipation rate, k is the turbulent kinetic energy and α_0 is a model constant. The *Intermediate Net Turbulent Flame Stretch (INTFS)* term (Γ_K) is defined as:

$$log_{10}(\Gamma_K) = -\frac{1}{(s+0.4)}e^{-(s+0.4)} + \left(1-e^{-(s+0.4)}\right)\left(\sigma_1 s\frac{u'}{S_L} - 0.11\right), \tag{4.10}$$

$$\sigma_1\left(\frac{u'}{S_L}\right) = \frac{2}{3}\left(1-\frac{1}{2}e^{-\sqrt[3]{\frac{u'}{S_L}}}\right), \tag{4.11}$$

where u' is the turbulent velocity fluctuation and s is defined as:

$$s = log_{10}\left(\frac{l_t}{\delta_l^0}\right), \tag{4.11}$$

where l_t is the turbulent integral length scales and δ_l^0 is the laminar flame thickness. The closure for the ECFM model is achieved by computing the laminar flame thickness δ_l^0. In this work, the equations proposed by Poinsot [44] are used. The laminar flame thickness is computed as:

$$\delta_l^0 = \frac{2\alpha}{S_L}, \tag{4.12}$$

where α is the unburned gas thermal diffusivity. In addition, the model proposed by Poinsot for the laminar flame thickness adds a correction to the INTFS term Γ_K, which is replaced by $\Gamma_K + \Gamma_P$. Γ_P is determined by using the following equations:

$$\Gamma_P = -\frac{3}{2}\frac{l_t S_L}{\delta_l^0 u'} log\left(\frac{1}{1-p_q}\right), \tag{4.13}$$

$$p_q = \frac{1}{2}\left[1 + tanh\left(\frac{b^3}{|b|}\right)\right], \tag{4.14}$$

$$b = \frac{\left[log_{10}\left(\frac{u'}{S_L}\right) - g_l\right]}{0.04\ s}, \tag{4.15}$$

$$g_l = \left(0.7 + \frac{1}{s}\right)e^{-s} + (1 + e^{-s})(1 + 0.36s). \tag{4.16}$$

In the present work iso-octane has been selected as gasoline surrogate. A reduced chemical kinetics mechanism for iso-octane has been implemented in the combustion model. This mechanism consists of 73-species and 296 reactions [45] and includes a sub-mechanism for NOx formation, with an addition of 15 chemical species and 53 reactions [46].

The combustion model takes into account the influence of the burned gases within the combustion chamber. This leads to a more accurate evaluation of the combustion process.

The laminar flame speed (S_L) of the iso-octane/air mixture is determined using the correlation proposed by Metghalachi and Keck [47]. This correlation takes into account the effects of pressure, temperature, equivalence ratio (φ) and residual combustion gases present in the unburned mixture (Y_d), according to the following equation:

$$S_L = S_{L_0}\left(\frac{T_u}{T_0}\right)^{\alpha}\left(\frac{p}{p_0}\right)^{\beta}(1 - 2.1Y_d), \tag{4.17}$$

where T_0 = 298 K, p_0 = 1 atm, and

$$S_{L_0} = 0.2632 - 0.8472\ (\varphi - 1.13)^2, \tag{4.18}$$

$$\beta = -0.38 + 0.22(\varphi - 1), \tag{4.19}$$

$$\delta_l^0 = \frac{2\alpha}{S_L}, \tag{4.20}$$

The value of laminar flame speed is determined in each cell, the unburned gases temperature T_u is determined as the mass-weighted average temperature of the cells where the progress variable is lower than 0.01, whereas, as regards the pressure, the value of the current cell is used. If the minimum value of the progress variable in the domain is higher than 0.01, the unburnt temperature is set to the lowest temperature in the domain.

As regards the spark ignition model, the initial spark kernel is assumed to be a perfect sphere of radius r_0. The flame front is assumed to be infinitely thin. The spark kernel radius grows according to the following equation:

$$\frac{dr}{dt} = \frac{\rho_u}{\rho_b} S_{ts}, \tag{4.21}$$

where S_{ts} is the spark model turbulent flame speed, which is defined as the highest value between the mixture laminar flame speed (S_L) and the turbulent flame speed evaluated at the turbulent length scale of the spark radius ($S_{ts}(r)$).

During the spark flame front propagation, the reaction progress variable *c* is determined as:

$$\mathrm{c} = \left(\frac{r}{r_f}\right)^3, \tag{4.22}$$

where r_f is the final spark kernel radius. All other variables, such as temperature and species mass fraction, are computed as:

$$\zeta = \mathrm{c}\zeta^b + (1 - c)\zeta^u, \tag{4.23}$$

where ζ is a general scalar quantity, the superscripts *b* and *u* denote the burned (i.e. chemical equilibrium) and unburned state, respectively. The spark propagates according to the spark model equations presented above until it reaches a given final radius r_f. From that point, the combustion develops according to the ECFM model. The initial value of the flame area density $\Sigma_{initial}$ is:

$$\Sigma_{initial} = \left[\max\left(r_f, 0.0001\right)\right]^{-1}. \tag{4.24}$$

As regards the water injector, it is modelled as a convergent-divergent nozzle in order to obtain an accurate velocity profile at the injector exit. Indeed, it is possible to simulate both the laminar sublayer due to the injector walls and the development region of the supersonic jet into the combustion chamber. The boundary conditions at the injector inlet are the mass flow rate and the inlet total temperature. The velocity contour plot in the nozzle during injection is given in Figure 4.3, where it is clearly shown how the fluid flow accelerates from subsonic to supersonic conditions.

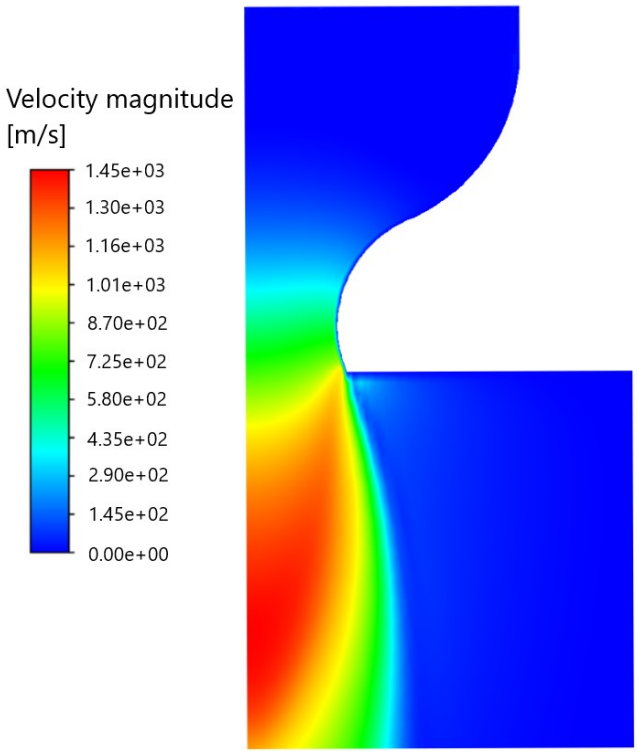

Figure 4.3: Velocity contour plot: zoom on the nozzle.

The injected water is treated as a perfect gas and its properties are determined by the *JANAF* tables coefficients [27]. In the present work, the supercritical water injection starts when the flame front is sufficiently further down from the injector, so that the chemical interaction between the injected water and the flame front is negligible. In order to ensure that this interaction does not affect the results, injection starts at the time when the cumulative heat release due to combustion is about 97%. Such a time has been selected from the case without water injection.

4.2 Model validation

The numerical pressure and heat release rate profiles have been compared with the experimental data available in [29]. In order to achieve a good matching, various sets of geometry and models parameters have been tested. As regards the geometry, a parametric study has been performed, by keeping fixed all dimensions except the angle α, which measures the slope of the cylinder head, as shown in Figure 4.1. This allowed to determine the axisymmetric engine geometry that better approximates the actual geometry. Figure 4.4 shows a comparison of three axisymmetric geometries with α angle equal to 0°, 5° and 10°, respectively. Among the different geometries tested, the best approximation of the experimental heat release and in-chamber pressure profiles is obtained with α = 5°. Specifically, the geometry with α = 5° returns the best matching of

both the positive and negative slopes of the experimental heat release rate profile with respect to the engine geometries with α values of 0° and 10°.

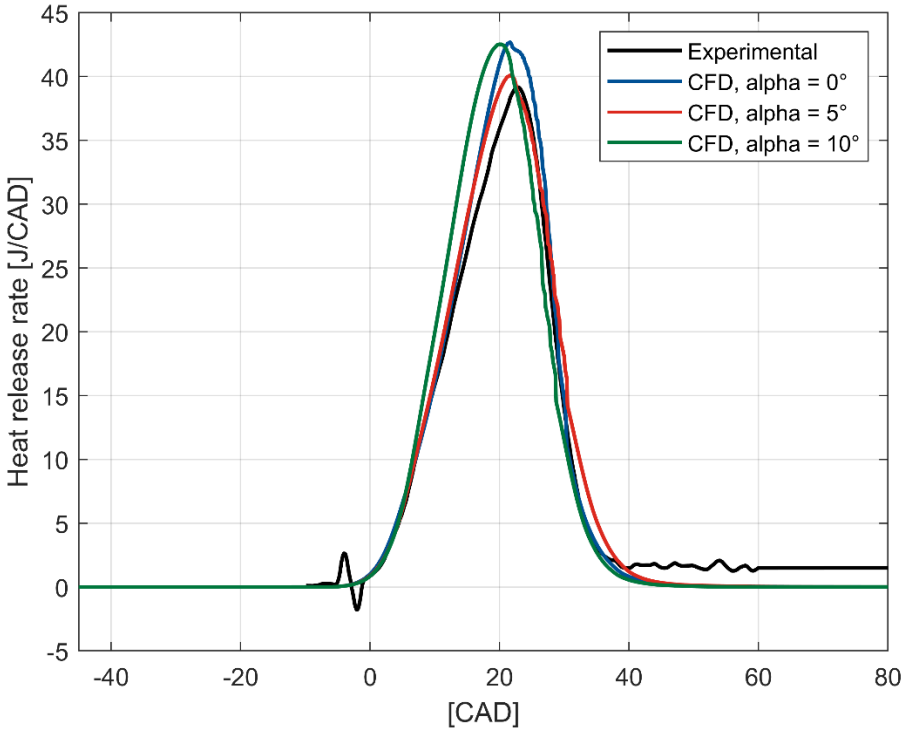

Figure 4.4: Heat release rate vs CAD: Experimental [29] vs CFD with different α angle (i.e. 0°, 5°, 10°).

As regards the initial thermodynamic conditions, they are listed in Table 4.3. The turbulent kinetic energy (k) and dissipation rate (ε) have been evaluated by using the correlations proposed by Hayder et al. [48]:

$$\mathrm{k} = \chi \left(\frac{A}{A_i}\right)^2 \frac{1}{\theta_i^2} \overline{v_p}^2, \tag{4.25}$$

$$\varepsilon = \psi \left(\frac{A}{A_i}\right)^3 \frac{1}{\theta_i^3} \frac{1}{\sqrt{A_i}} \overline{v_p}^3, \tag{4.26}$$

where A and A_i are the piston and maximum open intake valves area respectively, ϑ_i is the intake angle, $\overline{v_p}$ is the piston mean velocity. χ and ψ are dimensionless constants, which have been set to 0.0981 and 0.0267, respectively.

The unburned gases mass fraction comes from considerations on the experimental cumulative heat release rate and the values of pressure and temperature at the intake valve closing. The unburned gases composition is obtained by considering a complete air/iso-octane combustion, resulting in a composition of 72% of N2, 19% of CO2 and 9% of H2O in terms of mass. Furthermore, the initial spark radius has been set to 0.2 mm, while the transition to the ECFM model occurs when the spark kernel reaches a radius of 0.3 mm. The spark is axially located, in order to preserve the axial symmetry, at a distance of 1 mm respect to the engine head wall. In order to compensate for a

numerical delay which is introduced by the spark ignition model, the numerical spark advance has been set to -5 CAD ATDC instead of the -3 CAD ATDC used in the experimental setup. The turbulent Schmidt number, Sc_t, in Eq. (4.3) is set to 0.90. The simulations have been performed with a time-step of 0.125 CAD.

Table 4.3. Initial and boundary conditions

IVC pressure	0.98 bar
IVC temperature	410 K
IVC turbulent kinetic energy	4.4 m^2/s^2
IVC turbulent dissipation rate	180 m^2/s^3
Walls temperature	430 K
Equivalence ratio	1.0
Burned gas mass fraction	0.15
Swirl ratio	1.0

Figure 4.5 and Figure 4.6 show the comparison between experimental and numerical results in terms of heat release rate and in-cylinder pressure trace, respectively. The figures show that the numerical model returns a very good matching of the actual engine characteristics.

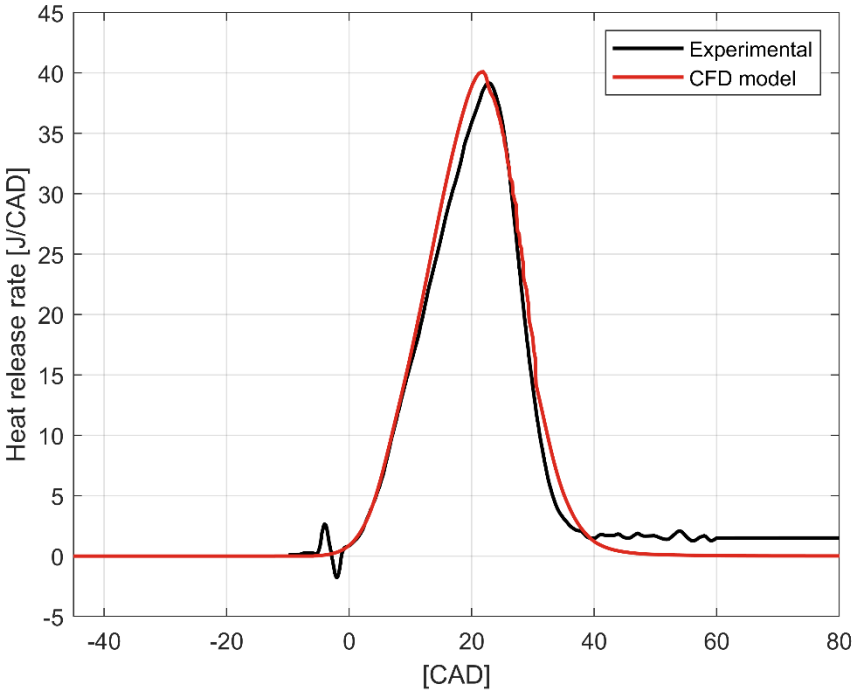

Figure 4.5: Heat release rate vs CAD: Experimental [29] vs CFD model (0 CAD = firing TDC)

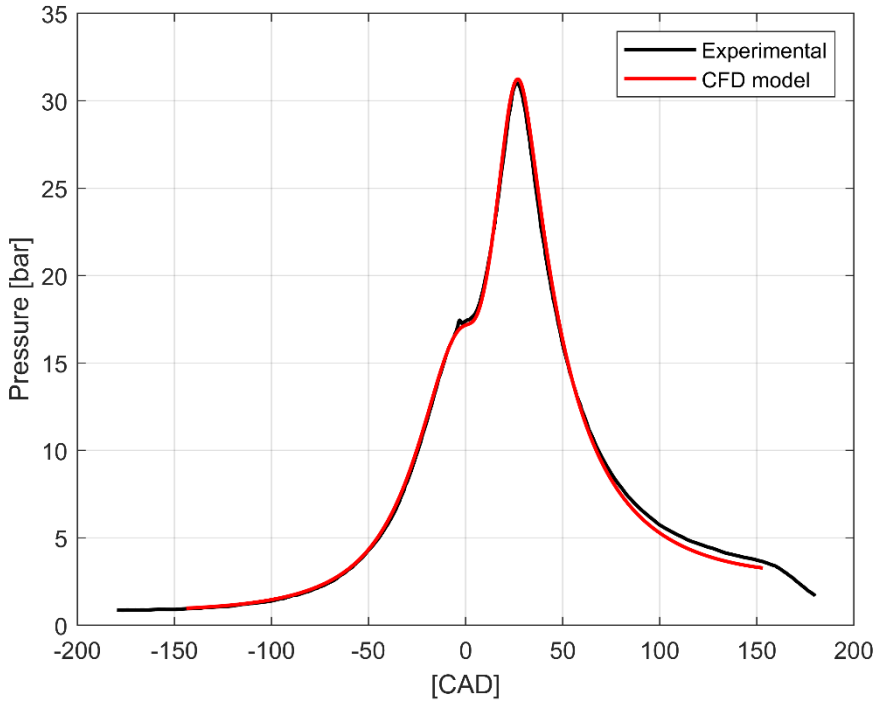

Figure 4.6: In-cylinder pressure vs CAD: Experimental [29] vs CFD model (0 CAD = firing TDC)

4.3 Supercritical water direct injection

In order to analyse the influence of supercritical water injection on the engine performance, the injection parameters have been set as listed in Table 4.4. As already stated in the previous paragraphs, the injection timing plays a significant role for the engine efficiency gain obtained with water injection. An early water injection maximizes the efficiency benefit, if supercritical water injection has not a negative effect on combustion. On the other hand, an early injection may affect the propagation of the flame front, which may cause an incomplete combustion, resulting in a lower engine overall efficiency. In the present work, a relatively late start of injection (SOI) is employed, so that injection starts when the heat release is almost completed. An earlier injection without flame interaction may be achieved if the piston geometry is properly optimized, but this issue goes beyond the scope of this analysis. Therefore, it should be pointed out that it should be possible to reach a higher engine efficiency gain with respect to the benefit achieved in this analysis.

Based on the injector geometry, water injection results in a supersonic under-expanded jet, which impinges on the piston surface. It has been proved that, when RANS models are used, the wall heat transfer evaluation of impinging jets configurations is very critical and leads to large heat transfer over-estimation if not carefully addressed [49-51]. In order to avoid this over-estimation and to compare the results of this analysis with the

results of the quasi-dimensional model, the simulations are performed under the hypothesis of adiabatic walls. Specifically, starting from SOI, the engine walls are considered adiabatic for both cases, i.e. with and without water injection. The consequences of this assumption are discussed later in this section.

In order to correctly represent the transient fluid dynamic structure of supersonic under-expanded jets, the time step has been reduced to 0.0001 CAD for the first 0.1 CAD after the SOI, the time step has been raised to 0.001 CAD until the end of the injection process. Mass flow rate has been set as the injector inlet boundary condition, in order to match the mass flow rate of the WISE model.

Table 4.4. Water injection parameters for the case with SOI=35 CAD ATDC

Injection total pressure	230 bar
Injection total temperature	846.8 K
Start of injection	35 CAD ATDC
Water injection duration	6.7 CAD
W/F	4.39
Mass flow rate	0.06258 kg/s
Total injected mass	$6.891 \cdot 10^{-5}$ kg

Water injection strongly modifies the in-chamber velocity distribution and thermodynamics. Figure 4.7B shows in-chamber Mach number, injected water mass fraction and temperature distributions at a late water injection stage (39 CAD ATDC). The water expansion at the injector exit increases the water jet Mach number up to about 4, and the characteristic fluid dynamics patterns of the Mach disk structure [52] are recovered. The jet impinges on the piston surface, resulting in a stagnation point on the axis and a radial spreading of the water along the piston surface. As shown in Figure 4.7B, the injected water flows along the combustion chamber walls, starting from the piston, then moving on the liner and finally arriving on the engine head. Figure 4.7B also shows a strong temperature reduction in the region of the combustion chamber where water is located. There is a higher temperature decrease closer to the engine walls, due to the higher water mass fraction. Indeed, the in-chamber temperature tends to reach a relatively uniform distribution later during the expansion stroke. The current model does not include the wall heat transfer during water injection. Nevertheless, some considerations can be made. As stated before, the in-chamber temperature decreases close to the engine wall surfaces, which could result in a lower wall heat transfer. On the other hand, the flow velocity locally increases at walls due to the injection of water, which may result in a higher wall heat transfer coefficient. Further analyses are required to assess the actual influence of water injection on wall heat transfer, but it is more realistic to think that an increase of heat transfer is expected. If water injection leads to an increase of wall heat transfer, an *ad-hoc* piston geometry can limit this undesirable effect. In addition, as stated before, the piston geometry could help to avoid water-

flame front interactions, thus allowing an earlier SOI with an increase of the potential benefit in terms of engine work and efficiency gain.

In order to assess the grid accuracy, the Mach disk height from the injector exit, x_{disk} , has been compared with the value obtained by using the empirical relation proposed by Maté et al. [53,54]:

$$\frac{x_{disk}}{d_{inj}} = 0.67\sqrt{\frac{p_{inj}^0}{p_{ch}}}, \tag{2.49}$$

where p_{inj}^0 is the injection total pressure and p_{ch} is the in-chamber pressure, equal to about 26 bar during injection. In the simulations, the Mach disk height from the injector exit resulting from *Eq. 28* is approximately 4 mm. The numerical results show a very good agreement with this empirical relation.

Figure 4.7A shows the injected water mass fraction distribution at different crank angles, starting from 0.1 CAD up to 0.4 CAD after SOI. The supercritical water jet reaches the piston wall at about 0.3 CAD after SOI.

Figure 4.8 shows the in-cylinder pressure profiles with and without water injection into the chamber. During supercritical water injection, the pressure shows a strong change in its slope, since an increase of the overall mass in the chamber counterbalances the decrease of pressure during the expansion stroke. After the end of injection, the pressure profile evolves according to a standard expansion, but starting from a higher-pressure value with respect to the case without water injection. This leads to a larger work obtained during the expansion stroke. Specifically, the gross indicated work per cycle increases by 15%, going from 298.4 J to 343.3 J. This result is in-line with the quasi-dimensional analysis presented in section 2.7. Specifically, with the WISE model, under similar conditions with respect to the CFD simulation, an increase of 10.3% on the overall engine cycle efficiency was obtained, which is lower since in that case the intake/exhaust strokes are considered as well.

In addition, Figure 4.8 compares the pressure profiles obtained without water injection when the wall heat transfer is switched on and off and some differences are noticeable. Therefore, the estimation of the potential benefit of supercritical water injection could be considered a good approximation of the actual engine performance.

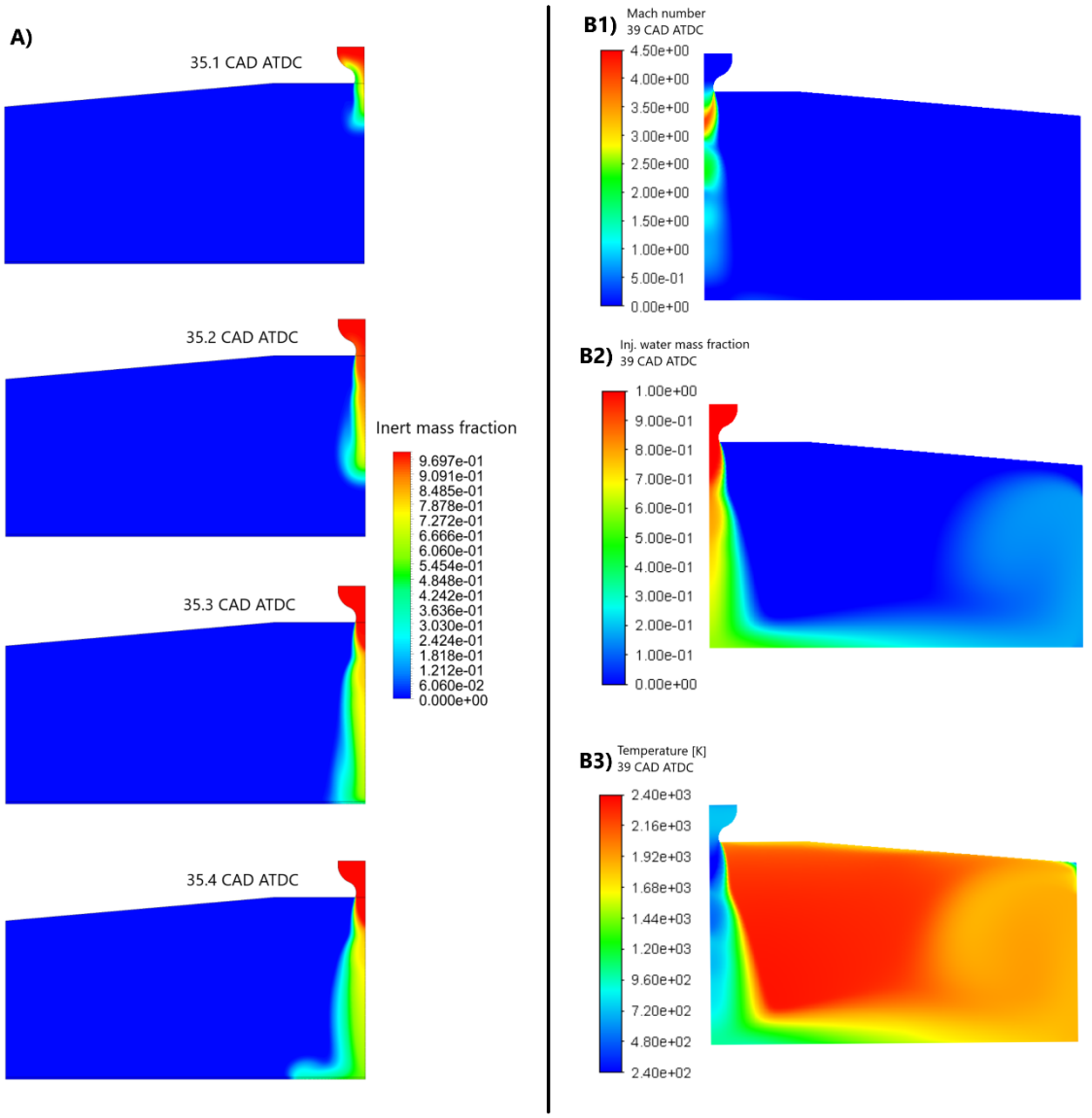

Figure 7: A) Water injection mass fraction at several times until the piston wall impingement, and in-cylinder Mach number (B1), Injected water mass fraction (B2) and temperature (B3) distributions at 39 CAD ATDC (0 CAD = firing TDC).

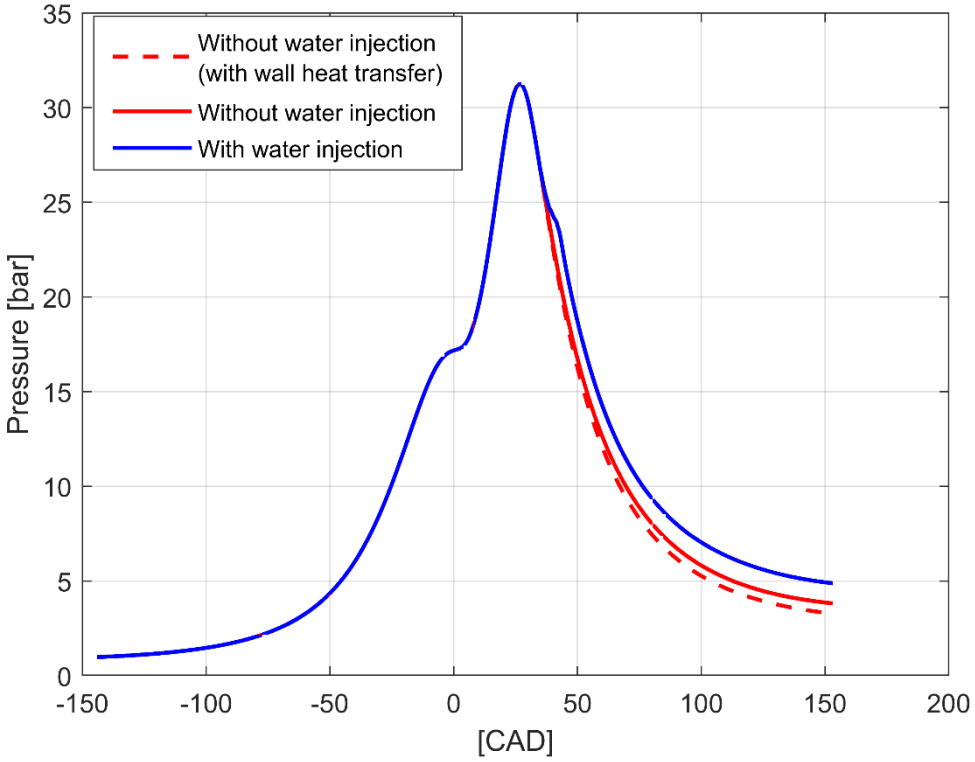

Figure 4.8: In-cylinder pressure vs CAD: CFD model without water injection (SOI=35 CAD ATDC) with wall heat transfer, CFD model without water injection without wall heat transfer starting from 35 CAD ATDC, CFD model with water injection without wall heat transfer starting from 35 CAD ATDC (0 CAD = firing TDC)

Since the combustion process, up to the crank angle when the heat release value is equal to 97%, follows the same trend with and without injection, no significant difference in terms of pollutant emissions is found for the two cases. An earlier water injection timing may result in lower emissions, which may be an additional benefit of this strategy together with higher engine efficiency and lower greenhouse gases emissions.

4.4 Effects of injector architecture on water jet structure

The injected water jet structure plays a fundamental role on the actual efficiency gain achievable with supercritical water injection, since its direction and momentum will influence both the interaction with the flame-front and the wall heat transfer. Indeed, the longer the jet wets the combustion chamber walls, the higher the wall heat transfer. On the other hand, a jet directed towards the flame front may either enhance combustion or quench the flame. It should be also mentioned that the effect of the injection on combustion enhancement and heat transfer are not dependent solely on the injector architecture, but also on the combustion chamber geometry.

Three different injector architectures have been analyzed in order to investigate the resulting jet structure:

- *Axial injector*: the injector used in section 4.1, which consists in an axial-symmetric convergent-divergent nozzle. The whole pintle is inside the injector body (Figure 4.9A);
- *Open nozzle injector*: the injector pintle opens towards the combustion chamber, the resulting jet will have a hollow-cone shape (Figure 4.9B). The geometry of the injector pintle plays a significant role on the resulting jet direction;
- *4-Holes injector*: the injector body has 4 holes for the fluid discharge. The pintle is fully inside the injector body (Figure 4.9C);

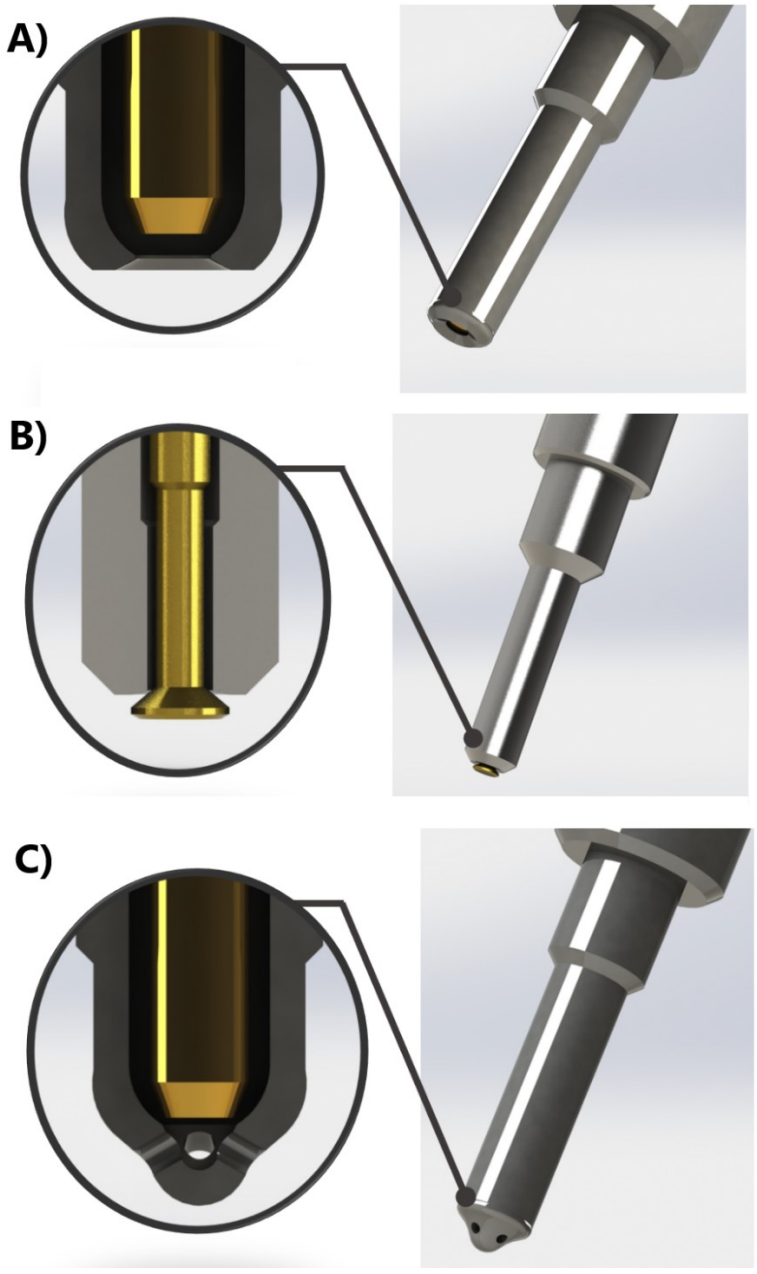

Figure 4.9: Different injector architectures: A) axial injector, B) open nozzle injector, and C) 4-holes injector (details in the section view).

The analysis has been performed using the ECFM model with the same engine geometry used in section 4.1. The injector geometries are displayed in Figure 4.10.

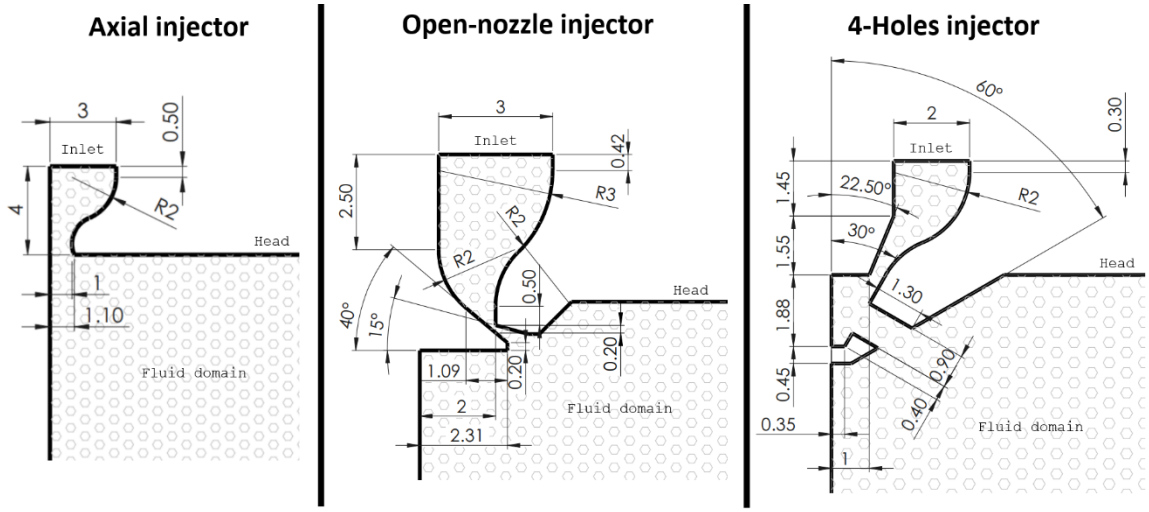

Figure 4.10. Injector geometries.

The injector used in internal combustion engines usually operates with low temperature fluids, which do not cause overheating of its components. Injecting a high temperature fluid, such as water in a supercritical state, may lead to failure, due to the high temperatures reached by the injector parts. Therefore, the injector may need a cooling circuit and/or the injection temperature must be limited to a certain maximum value. For this reason, in this analysis, the injection temperature has been limited to the maximum value of 773 K. Specifically, the injection thermodynamic conditions simulated are listed in Table 4.5.

Table 4.5: Water injection thermodynamic conditions

	Condition A	**Condition B**
Injection total temperature	673 K	773 K
Injection total pressure	250 bar	150 bar
Water/Fuel ratio	4	3

4.4.1 Axial injector

The axial injector has already been used in section 4.1, where the jet structure resulting in the case of an injection pressure of 230 bar and an injection temperature of 846.8 K has already been discussed. The new injection conditions do not radically change the jet

structure. At the injector exit the typical under-expanded jet structure is observed, with the formation of the Mach disk, and several subsequent compressions and expansions. The jet eventually reaches the piston surface, impinging on it, then moving in radial direction toward the liner wall. Close to the liner wall, the formation of an eddy is observed, which dissipates the jet kinetic energy and causes the mixing of the injected water with the combustion chamber gases. The injection transient for condition A and condition B is shown in Figure 4.11. The main differences between injection conditions B with respect to injection conditions A are a delayed jet impingement, a lower maximum Mach number and a higher number of subsequent compressions/expansions.

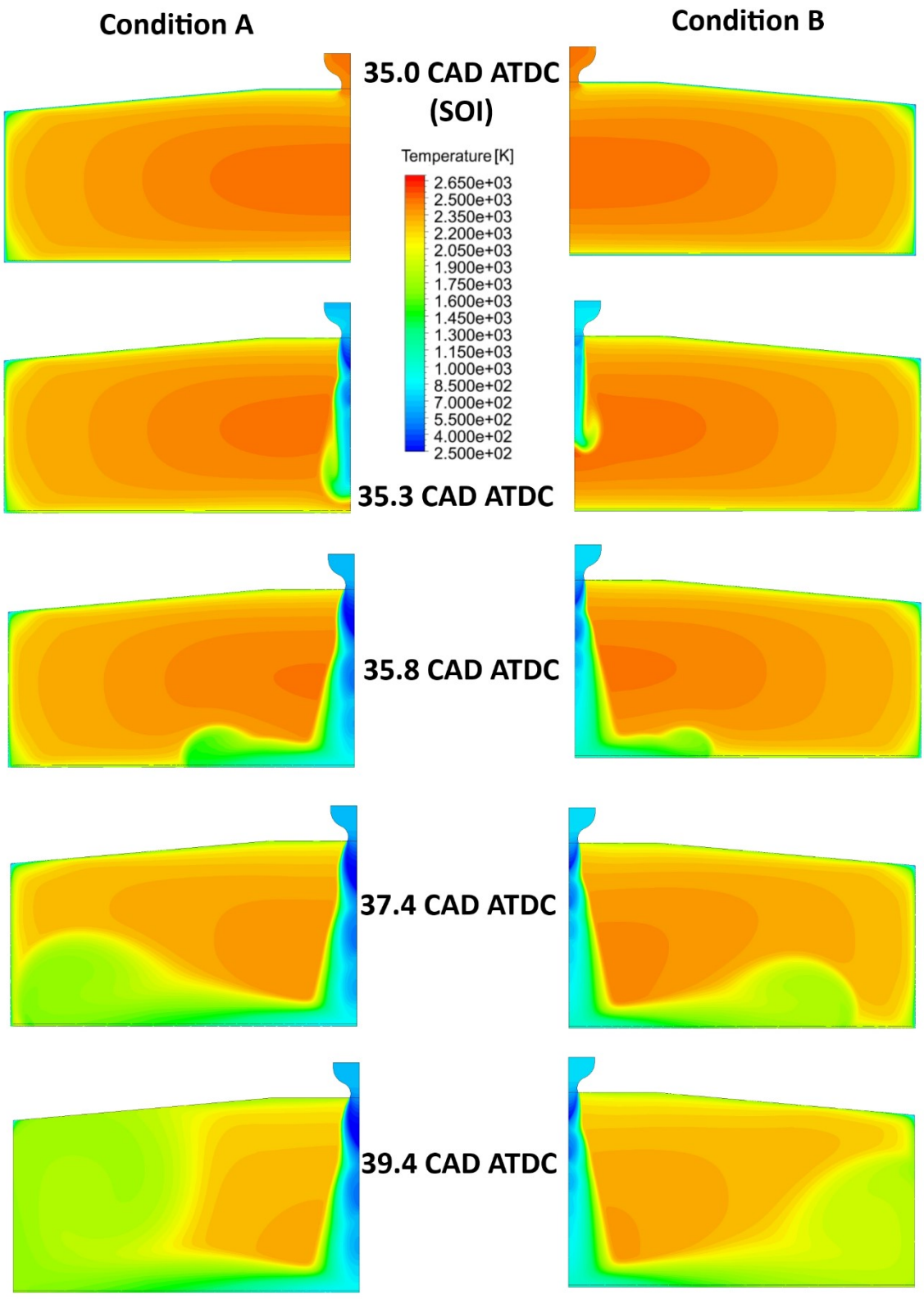

Figure 4.11: Injection transient for configuration A and B, in terms of temperature contour plots, in the case of axial injector architecture.

Considering the jet structure resulting in the case of the axial injector architecture, an increased heat transfer is expected mainly through piston walls, but also through liner

and head walls at a lower extent. As regards the interaction with combustion, if the flame front has already reached the piston surface the jet will travel the longest possible distance before reaching it. The main benefit of this aspect may be the dissipation of momentum before the jet reaches the flame front, which would result in a lower likelihood of flame quenching. A lower injection pressure would result in lower momentum when the jet reaches the flame front, which may allow a more advanced SOI without resulting in the quenching of the flame. On the other hand, if flame quenching does not occur, this architecture may be sub-optimal.

4.4.2 Open nozzle injector

The pintle of the open nozzle injector opens towards the combustion chamber, resulting in a hollow-cone shaped jet. Figure 4.12 shows the combustion chamber and a detail of the computational grid close to the injector. The grid is more refined in the vicinity of the injector since a higher spatial resolution is needed.

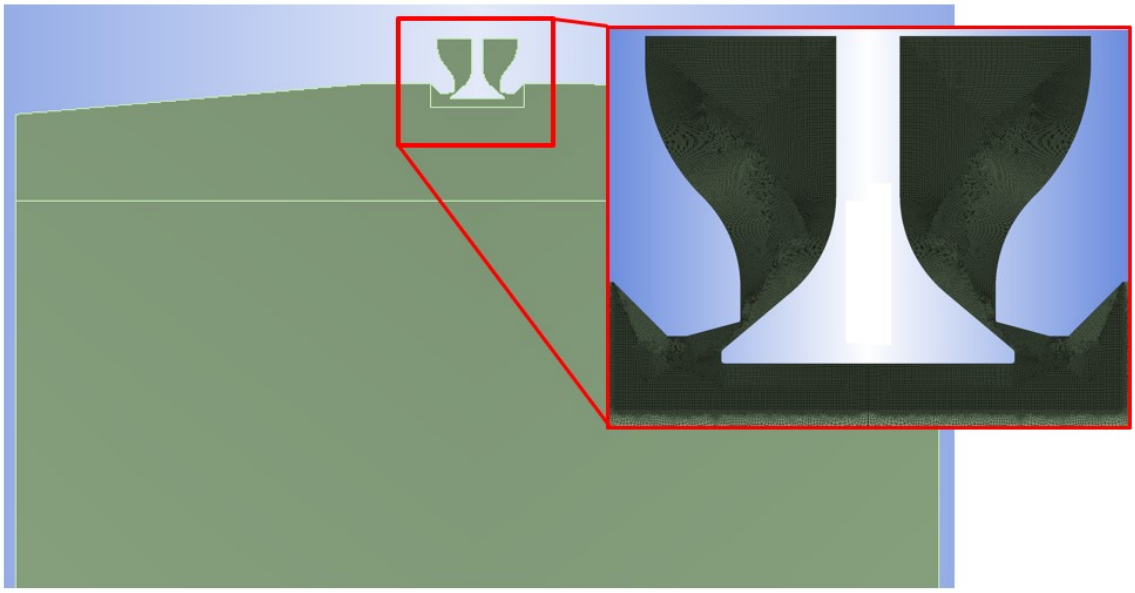

Figure 4.12 Open nozzle injector computational domain and computational domain and injector grid detail.

The selected injector geometry has a throat area of 2.42 mm^2, which allows a mass flow rate of 0.0612 kg/s and of 0.0254 kg/s for *Condition A* and *Condition B* respectively (calculated according to Eq. 3.19). For the simulations performed with the open nozzle injector architecture a SOI of 31 CAD ATDC has been selected, which corresponds to a 90% complete combustion.

Figure 4.13 shows the injection transient for the two configurations. Both result in a jet attachment to the head surface. The jet then moves towards the liner wall, following its surface, forming a vortex similar to what is observed with the axial injector that favors the mixing between the injected water and the burned gases. As one may expect, a

lower injection pressure results in a slower jet, which takes longer to reach the liner walls. Therefore, as already observed for the axial injector architecture, *Configuration B* will have a delayed and weaker interaction with the flame front. As already stated, this effect could be beneficial if the jet-combustion interaction is such that quenching of the flame takes place, while it could be detrimental if the jet enhances combustion. The open-nozzle architecture has a similar behavior with respect to the axial injector, where the jet follows the piston surface instead of the head surface. Indeed, the axial architecture follows a longer path, which results in a delayed interaction with combustion, together with a lower momentum. The benefits of one or the other configuration must be carefully analyzed with appropriate models and/or an experimental campaign.

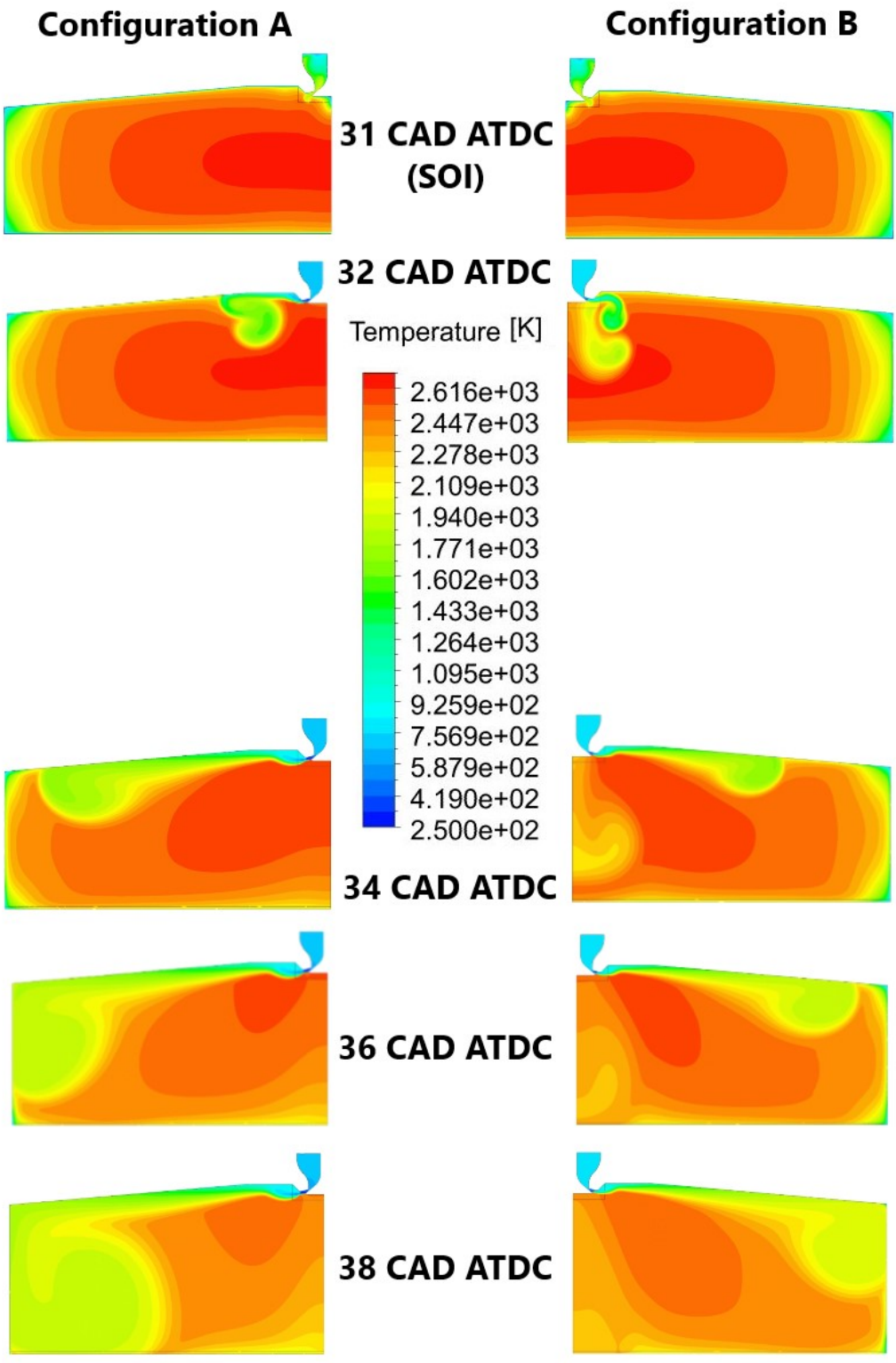

Figure 4.13 Injection transient for configuration A and B, in terms of temperature contour plots, in the case of open nozzle injector architecture.

4.4.3 4-Holes injector

The geometry considered for the 4-holes injector will produce 4 distinct under-expanded supersonic jets, spaced by 90°. Therefore, the domain is not axial-symmetric, making it

necessary to use a 3D numerical domain. Since the domain has two planes of symmetry, a 90° sector can be used for the simulations. The 3D domain, the mesh and a close-up of the injector are shown in Figure 4.14. The mesh is structured anywhere except for the injector. The structured mesh is formed by elements of 1 mm side minimum, while the tetrahedral elements in the vicinity of the injector have sides between 0.1 mm and 1 mm. The number of elements at the bottom dead center is ~133k.

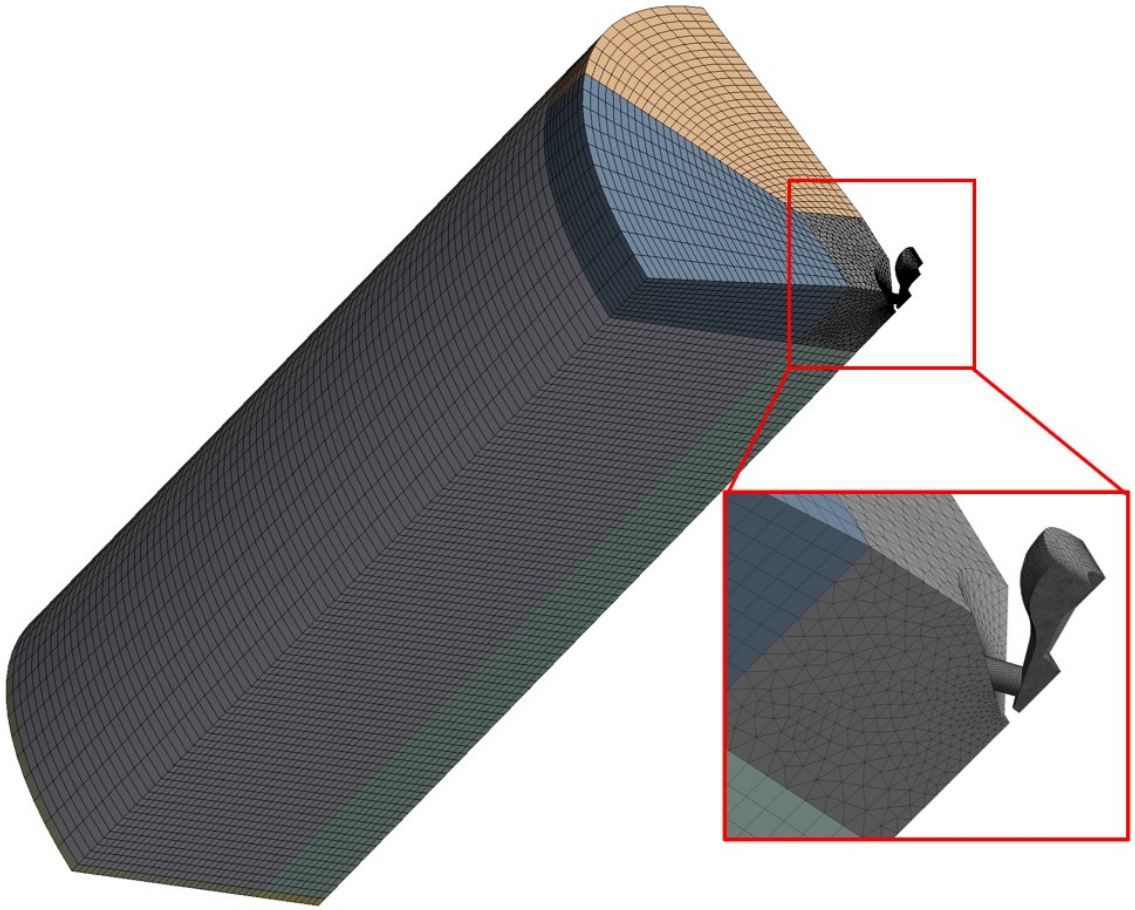

Figure 4.14 4-Holes injector computational domain and injector grid detail.

Since for the previous injector architectures the two conditions listed in Table 4.5 returned comparable results, and considered that the 3D domain used in this case increases the computation time, only *Configuration A* has been simulated. For the injector geometry used, displayed in Figure 4.10, the mass flow rate is limited by the holes area, which therefore represents the throat section. According to Eq. 3.19, the mass flow rate is equal to 0.08296 kg/s.

As it can be seen from Figure 4.15, the 4-holes injector geometry used results in a jet with the same direction of the hole axis, which impinges on the piston surface, then moves mostly towards the combustion chamber liner and head walls. The main difference between this architecture and the two previously analyzed is the direction of the jet, which does not follow a solid boundary until it reaches the piston surface. Furthermore, with the 4-holes injector, the four-jets have a circular cross section when

they reach the flame front, while the axial injector and the open nozzle injector both reach the flame front with a continuous cylindrical cross section, which has a wider jet-flame front impact area. These two aspects need to be very carefully considered in terms of interaction with the flame front: among the three injector architectures analyzed, this one will reach the flame front in the shortest time and will also have the highest probability of flame quenching, since it will carry a higher momentum and will interact with the flame front on a smaller surface. On the other hand, if quenching does not take place, this architecture will give the highest benefits in terms of combustion enhancement.

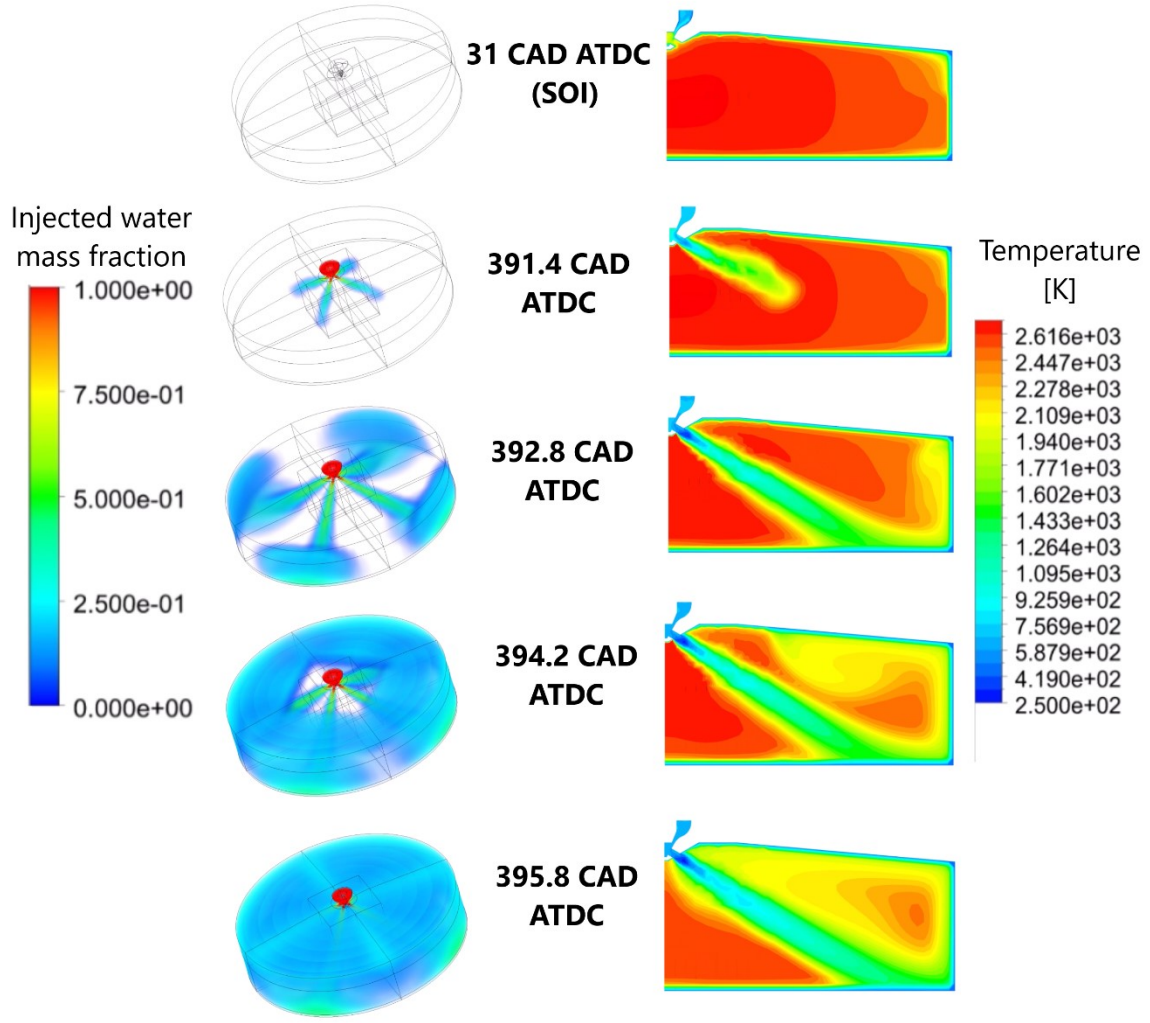

Figure 4.15 Injection transient for configuration A and B, in terms of temperature contour plots, in the case of 4-holes nozzle injector architecture.

Chapter 5

Supercritical water direct injection: RANS simulations with the EDC Model

5.1 The Eddy-Dissipation Concept model

The ECFM model has been useful to understand the jet structure resulting from the different injector architectures, especially considering its relatively low computational time. Nonetheless the ECFM model does not seem to be reliable in terms of water injection-combustion interaction. Few tests have been performed with the ECFM model and water injection always resulted in combustion enhancement. It never predicted flame quenching, not even with very advanced SOI. Indeed, a negative effect of water injection on combustion is expected for advanced SOI, since the jet could destroy the flame front. The analysis performed with the ECFM model assumed that the injected water did not affect chemistry, therefore the amount of water in a computational cell did not affect the laminar flame speed and the equilibrium chemical composition, but only the temperature reached in that cell. Hence the model is not capable of predicting flame quenching if, with water injection, the flammability limit is locally reached.

In order to have a more accurate prediction of the effects of water injection on combustion, the *Eddy-Dissipation Concept* (EDC) model [55] has been used. The use of this model allows to solve detailed kinetic reaction mechanisms and accounts for turbulence-chemistry interactions. The underlying assumption is that reactions take

place within small turbulent structures, called *fine scales*, whose length depends on the flow turbulence level, according to the equation:

$$\xi^* = C_\xi \left(\frac{\nu\varepsilon}{k^2}\right)^{1/4}, \tag{5.1}$$

where C_ξ is a model parameter, ν is the kinematic viscosity, and k and ε are the turbulent kinetic energy and its dissipation rate, respectively. The volume fraction of the fine scales is calculated as ${\xi^*}^3$. The reactions in the fine structures are assumed to occur within the time scales:

$$\tau^* = C_\tau \left(\frac{\nu}{\varepsilon}\right)^{1/2}, \tag{5.2}$$

where C_τ is a model parameter. The reactions are assumed to occur in a constant pressure reactor and are governed by the reaction rates resulting from the species concentrations and thermodynamic conditions in each cell, according to the chemical kinetics mechanism used. The reaction rates are then adjusted to take into account turbulence, according to the equation:

$$R_i = \frac{\rho(\xi^*)^2}{\tau^*[1-(\xi^*)^3]}(Y_i^* - Y_i), \tag{5.3}$$

where R_i is the net rate of production, Y_i is the initial species mass fraction, while Y_i^* is the species mass fraction resulting from the constant pressure reactor calculations performed using the provided chemical kinetic mechanism. The resulting net rates of production R_i are then used in a convection-diffusion equation for the *i-th* species:

$$\frac{\partial}{\partial \mathrm{t}}(\rho Y_i) + \nabla \cdot (\rho \bar{v} Y_i) = -\nabla \cdot \bar{J}_i + R_i, \tag{5.4}$$

where $\bar{v}$ is the mean velocity, $\bar{J}_i$ is the diffusion flux of species *i*. An equation in the form of Eq. (5.4) will be solved for N-1 chemical species, where N is the total number of species in the system. More details on the EDC model can be found in the Ansys Fluent theory guide [43].

The ignition model used consists in an increment of the temperature in a specific zone, close to the spark location. The temperature is increased to 1500 K, then chemical reactions proceed according to the EDC model. Figure 5.1 shows the spark zone and the temperature distribution in the combustion chamber at the ignition time.

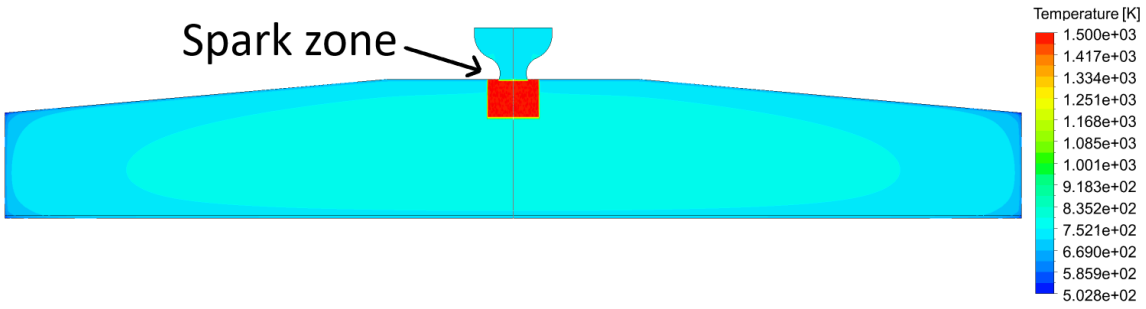

Figure 5.1: Spark zone and in-chamber temperature distribution at the ignition time.

The EDC model allows to take into account the effects of the instantaneous chemical composition, thermodynamic conditions and turbulence on chemical reactions. This is indeed a better way to model the water injection-combustion interaction when compared to the ECFM model, but, as all the RANS models, it still needs calibration on experimental data to increase the confidence level on results. The model calibration will be performed in the case without water injection, which will give some reliability to the results. Nonetheless, the lack of experimental results with water injection is the main shortcoming of the injection-combustion interaction evaluation presented in this section.

5.2 Model validation

The same reference engine used to calibrate the ECFM model has been used to calibrate the EDC model. Furthermore, the same grid has been used, since it was considered accurate enough for RANS modelling. The EDC model calibration essentially consists in finding the values of the two constants C_{ξ} and C_{τ} (Eq. 2.50 and Eq. 2.51 respectively), which return a good approximation of the experimental pressure trace and a reasonable flame front shape. In particular, if the EDC model constants are not carefully calibrated the EDC model may predict a higher flame speed close to the walls, resulting in a convex flame-front, which does not match experimental observations.

The initial and boundary conditions resulting from the validation process are listed in Table 5.1. It should be highlighted that the equivalence ratio is set to 0.9, even if the real engine works with an equivalence ratio of 1.0, in order to match the cumulative heat release resulting from the combustion process. This can be justified by the assumptions of the numerical model, which does not account for blow-by and does not take into account the presence of crevices, where fuel oxidation essentially does not take place.

Table 5.1. Initial and boundary conditions resulting from the validation process for the EDC model.

IVC pressure	0.97 bar
IVC temperature	410 K
IVC turbulent kinetic energy	4.4 m^2/s^2

IVC turbulent dissipation rate	180 m^2/s^3
Walls temperature	430 K
Equivalence ratio	0.9
Burned gas mass fraction	0.15

Figure 5.2 shows the comparison between the experimental and numerical pressure (A) and heat release rate (B) obtained with C_ξ equal to 6.4131 and C_τ equal to 1.6328, and a time-step of 0.01 CAD (i. e. 1.667x10^{-6} s at 1000 rpm). Figure 5.3 shows the flame front at 14 CAD ATDC, which has the typical shape expected in the case of premixed combustion.

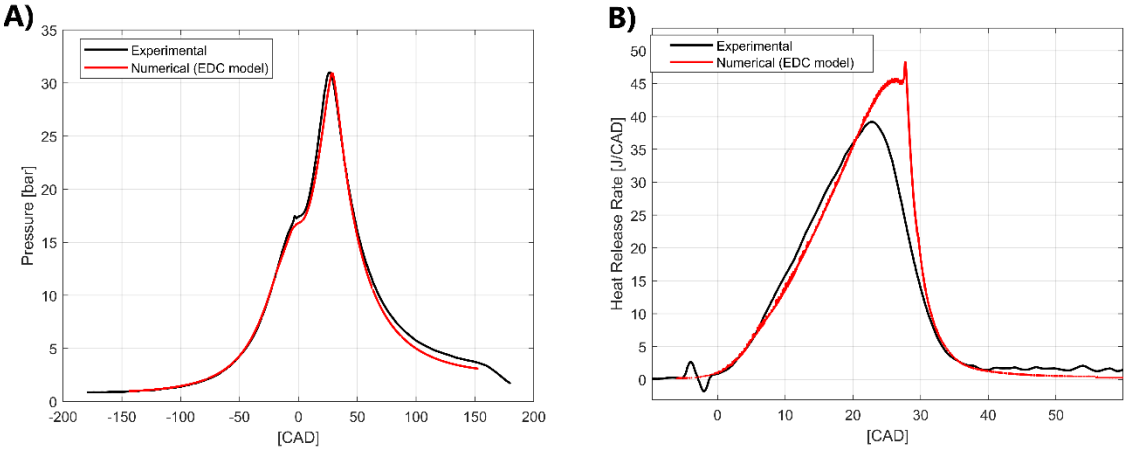

Figure 5.2: A) In chamber pressure vs CAD: Experimental [29] vs CFD model (EDC); B) Heat release rate vs CAD: Experimental [29] vs CFD model (0 CAD = firing TDC).

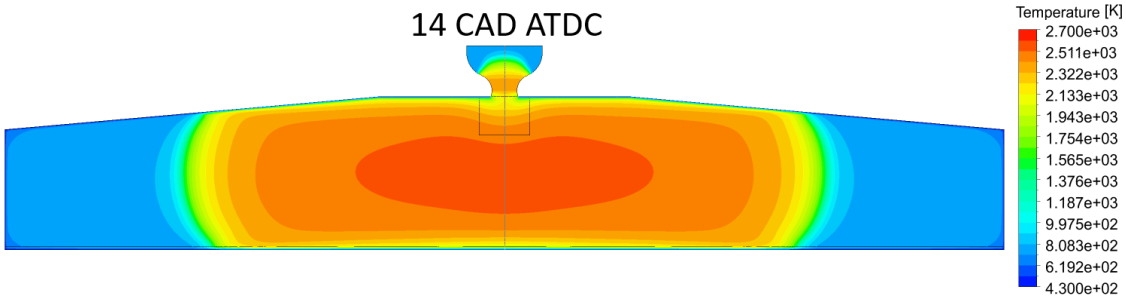

Figure 5.3: In-chamber temperature distribution at 14 CAD ATDC.

As shown in Figure 5.3, the injector is part of the fluid domain, therefore combustion takes place also in the injector. In the real setup, the injector is closed when combustion starts. Nonetheless, the injector volume in the CFD model is 700 times smaller than the combustion chamber volume at TDC, allowing to neglect its effects.

5.3 Injector opening/closing model

The injector opening/closing transient has been modelled by gradually increasing/decreasing the inlet total pressure, according to the equation:

$$p_{inj}^{0} = p_{inj\_max}^{0} \left\{ a_{inj} - \delta_{inj}\, exp\left[\left(-4\, \frac{t - t_{start}}{\Delta t} \right)^{3} \right] \right\}, \qquad (5.5)$$

where p_{inj}^{0} is the instantaneous inlet total pressure, $p_{inj\_max}^{0}$ is the injection pressure, a_{inj} is equal to 1 for the opening transient and to 0 for the closing transient, δ_{inj} is equal to 1 for the opening transient and to -1 for the closing transient, t is the numerical time, t_{start} is the start opening/closing numerical time, Δt is the opening/closing duration, set to $1.5*10^{-5}$ seconds both for the opening and closing transient. Figure 5.4 shows the opening and closing laws.

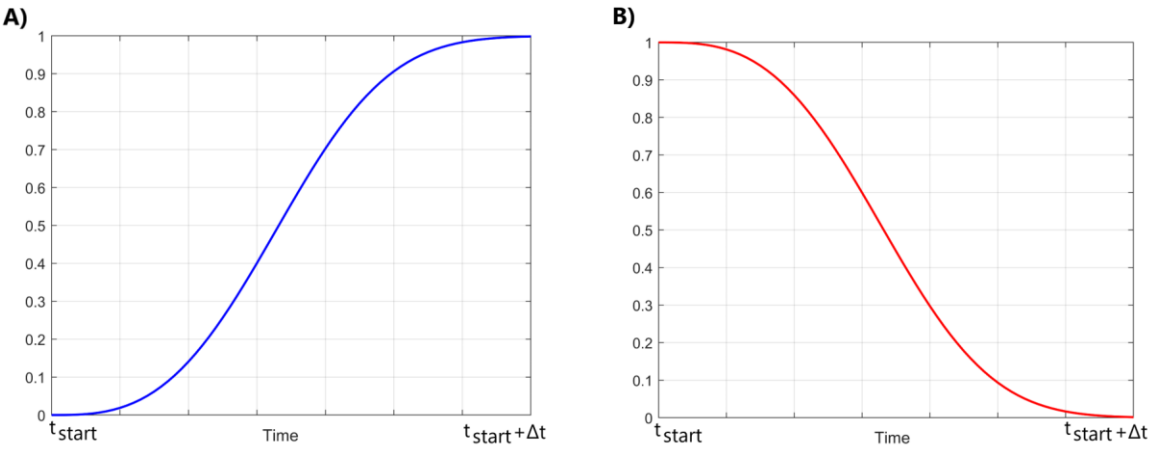

Figure 5.4: Water injector opening (A) and closing (B) laws (0 = full close, 1 = full open).

5.4 Water jet-combustion interaction: Axial injector

Injection conditions A

The axial injector is the first architecture that has been analyzed, by injecting water under the injection conditions A and B (Table 4.5). During water injection, in order to properly capture the supersonic jet structure resulting from water injection, and to avoid numerical errors, the time step has been reduced. In particular, the model has been tested with time steps of 0.001, 0.0004, 0.0002 and 0.0001 CAD. The time step independence is reached with a time step of 0.0002 CAD, which will be used for all the following simulations. In addition, it has also been checked that it is possible to increase the time step back to 0.01 CAD after water injection, without any noticeable effect on results.

Since the total pressure and total temperature have been set as inlet boundary conditions, in this case the WID cannot be determined a priori since the mass flow rate is unknown. The WID resulting from each simulation, the SOI and the mass flow rate through the injector are listed in Table 5.2. The parameter MBF (Mass fraction of Burned Fuel) is representative of the combustion progress. This parameter is linked to the SOI, but it intrinsically takes into consideration the flame front position, which, as opposed to the SOI, is independent respect to the engine SA. Therefore, it can be used to compare different engines.

Table 5.2. Water Injection Duration (WID) and Start of Injection (SOI) for injection conditions A (axial injector).

	MBF5	MBF15	MBF20	MBF25
WID [CAD]	5.1	5.1	5.1	5.1
SOI [CAD ATDC]	7.7	12.0	14.0	15.8
Mass flow rate [kg/s]	0.0929	0.0929	0.0929	0.0929

Figure 5.5 shows the engine cycle, without water injection and with water injection at different injection timings. The parametrization is presented with respect to the fuel Mass fraction of Burned Fuel (MBF) instead of the SOI. The figure shows that in all the configurations simulated a higher pressure peak is reached in the case with water injection with respect to the case without water injection (i.e. combustion is accelerated), except the case with SOI at MBF05.Particularly, with the injection set at MBF05 we notice a rapid pressure increase just after the start of injection. Unfortunately, this trend is not preserved for the rest of the expansion stroke due to the quenching of the flame, which results in a lower pressure peak respect to the case without water injection, thus a lower efficiency.

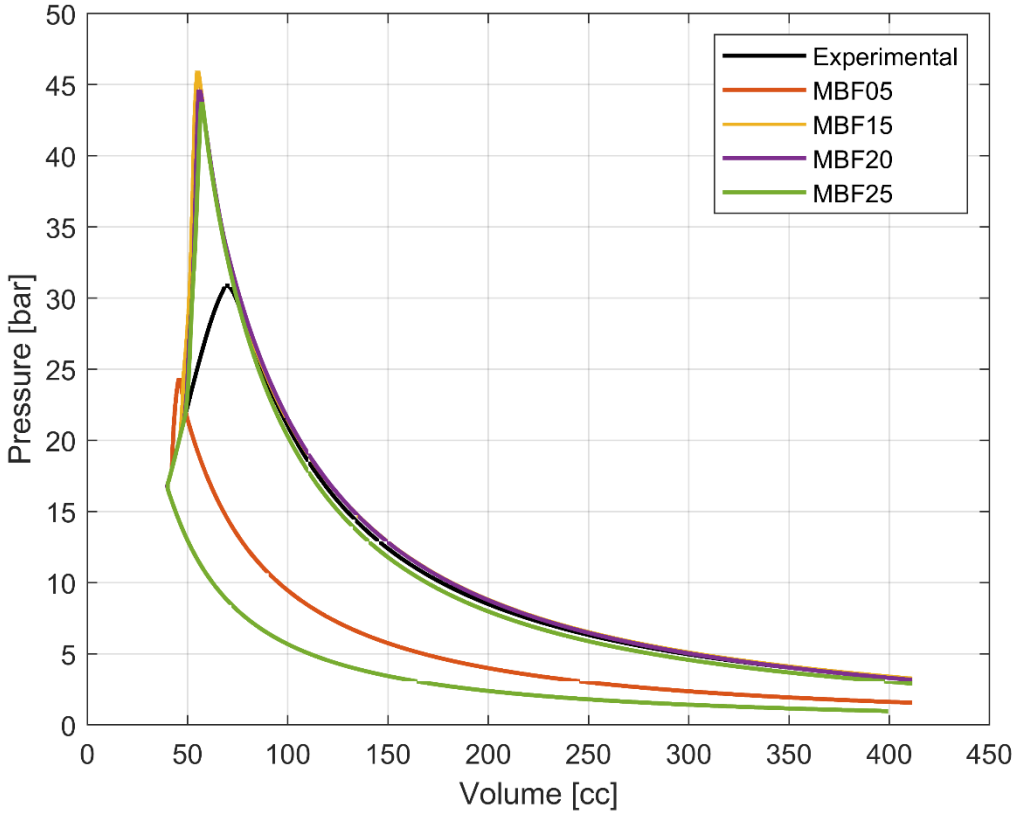

Figure 5.5. In-chamber pressure versus engine volume without water injection and for different MBFs with the axial injector architecture and injection conditions A.

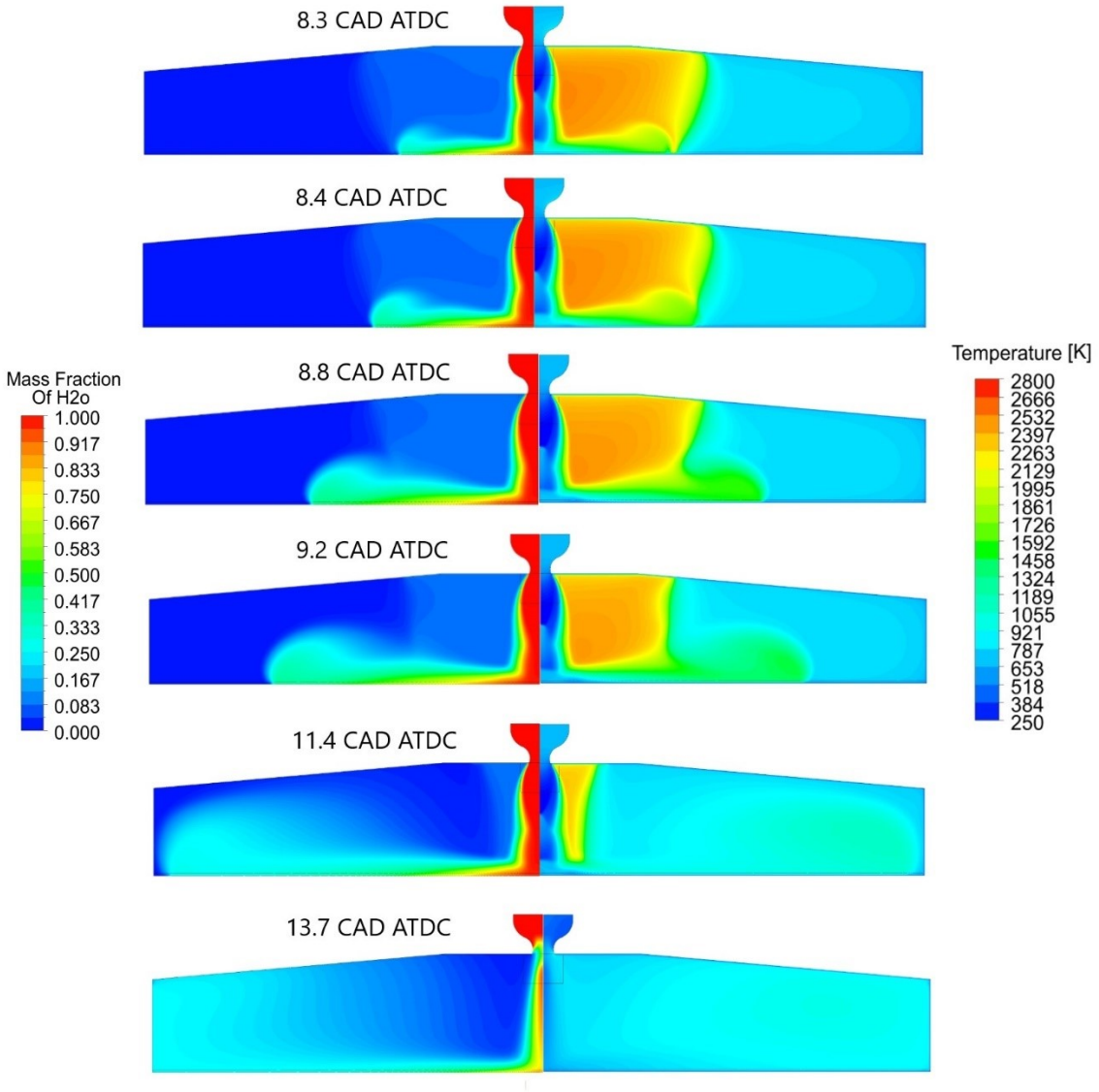

Figure 5.6. Water injection-combustion interaction transient for condition A at MBF5: water mass fraction (left) and temperature (right) contour plot.

In order to better understand the different phenomena that lead to flame quenching or combustion enhancement, an analysis of water injection-combustion interaction is performed. Figure 5.6 shows the water injection transient in the case with the start of injection at MBF5. The water jet reaches the flame front at ~8.3 CAD ATDC (1.4 CAD after the SOI). In this stage the combustion is accelerated, resulting in a higher in-chamber pressure with respect to the case without water injection. Around 8.8 CAD ATDC the water jet goes beyond the flame front and the injected water starts to mix with unburned gases. In addition, the velocity field generated by the jet pushes the flame front toward the engine axis, preventing combustion. As visible from the figure, at ~13.7 CAD we cannot distinguish a flame front anymore, since burned and unburned gases are mixed. The thermodynamic and the mixture composition is such that combustion cannot proceed. We have therefore reached combustion extinction.

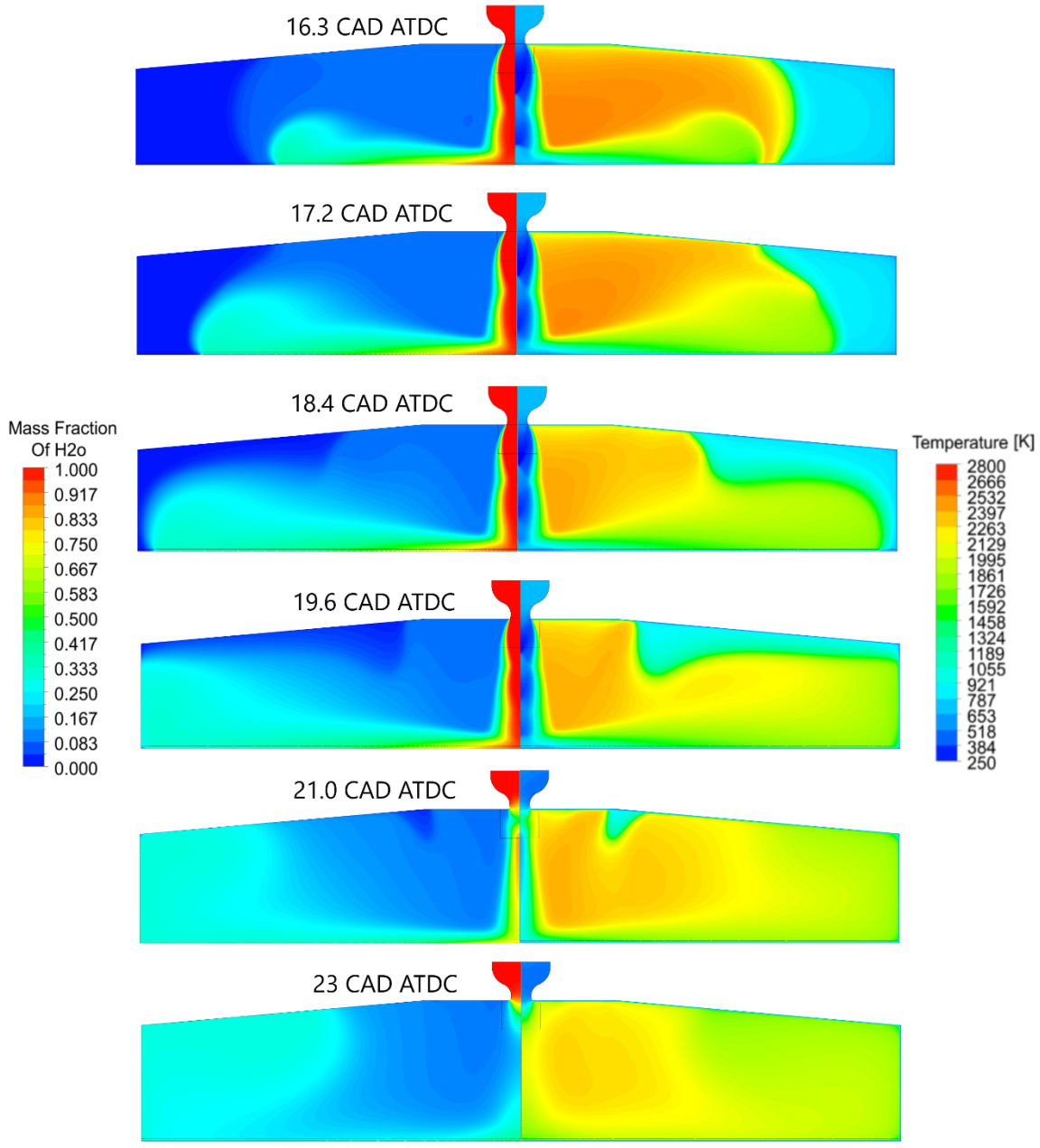

Figure 5.7. Water injection-combustion interaction transient for condition A at MBF20 (Axial injector): water mass fraction (left) and temperature (right) contour plot.

Figure 5.7 shows the water injection transient with SOI at MBF20 for condition A. The water jet reaches the flame front at ~16.3 CAD ATDC (2.3 CAD after the SOI). In this case, the jet does not reach the unburned gases before the flame front, but it only enhances combustion. In particular, the jet deforms the flame front, which does not only propagate towards the liner walls (as in the case without water injection), but also towards the engine head.

The goal of supercritical direct water injection is to improve engines efficiency. As we have just seen, water injection can enhance flame speed, which in turn increases the engine power output, therefore its efficiency. On the other hand, the supersonic under-expanded jet will enhance wall heat transfer, which reduces engine performances and

efficiency. Figure 5.8 shows the wall heat transfer without water injection and with water injection at different MBFs. Water injection always increases the overall wall heat transfer, except in the case MBF5, where it is 30% lower with respect to the case without water injection. This is caused by the substantially lower temperatures reached into the combustion chamber due to flame extinction. The cases MBF15 and MBF20 have an overall wall heat transfer 2.3 times higher with respect to the case without water injection, while in the case MBF25 it only doubles.

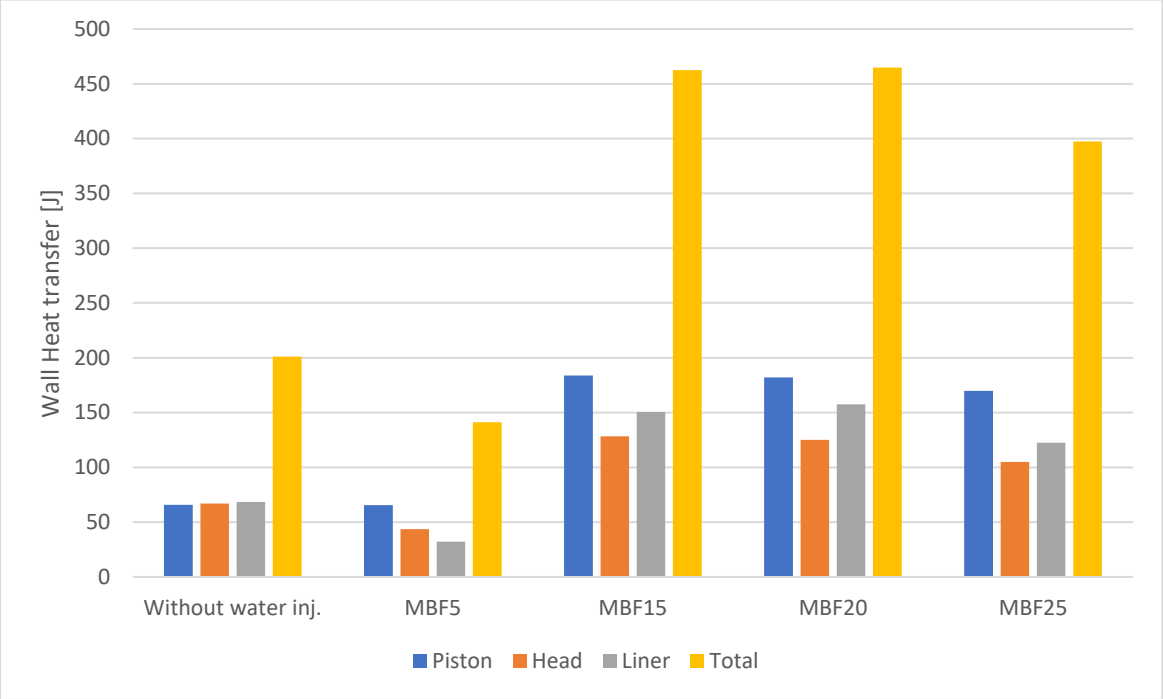

Figure 5.8: Total wall heat transfer without water injection and with water injection at different MBFs (Axial injector, injection conditions A).

Finally, the gross indicated work per cycle in the various cases have been evaluated. Figure 5.9 shows the relative work gain obtained with water injection at different MBFs. The injection of water at MBF5 reduces the engine work by 70%, therefore making the water injection strategy deleterious. Injecting at MBF25 has practically no effect on the engine gross indicated work per cycle, i.e. the benefits in terms of added mass and energy into the combustion chamber and the faster combustion are counteracted by the increased wall heat transfer. The maximum efficiency gain is reached between MBF15, with a work gain of +11.8% with respect to the case without water injection, and MBF20 where the work gain is +10.2% with respect to the case without water injection. In conclusion, in order to optimize the supercritical direct water injection strategy, it is crucial to select an appropriate SOI.

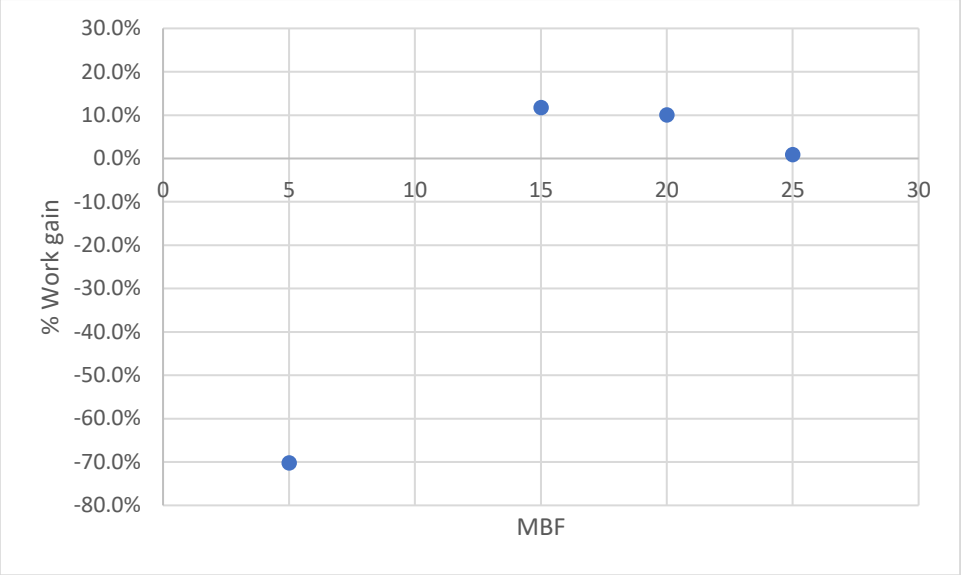

Figure 5.9: Relative work gain obtained with water injection respect to the case without water injection (axial injector, injection conditions A).

The work gain obtained with water injection comes from the effects of the added in-chamber mass and energy and the faster combustion. Figure 5.10 compares the combustion transient without water injection and with water injection in the case MBF15. The water jet substantially enhances combustion, both due to the faster flame speed and the higher flame surface due to the deformation of the flame front caused by the water jet.

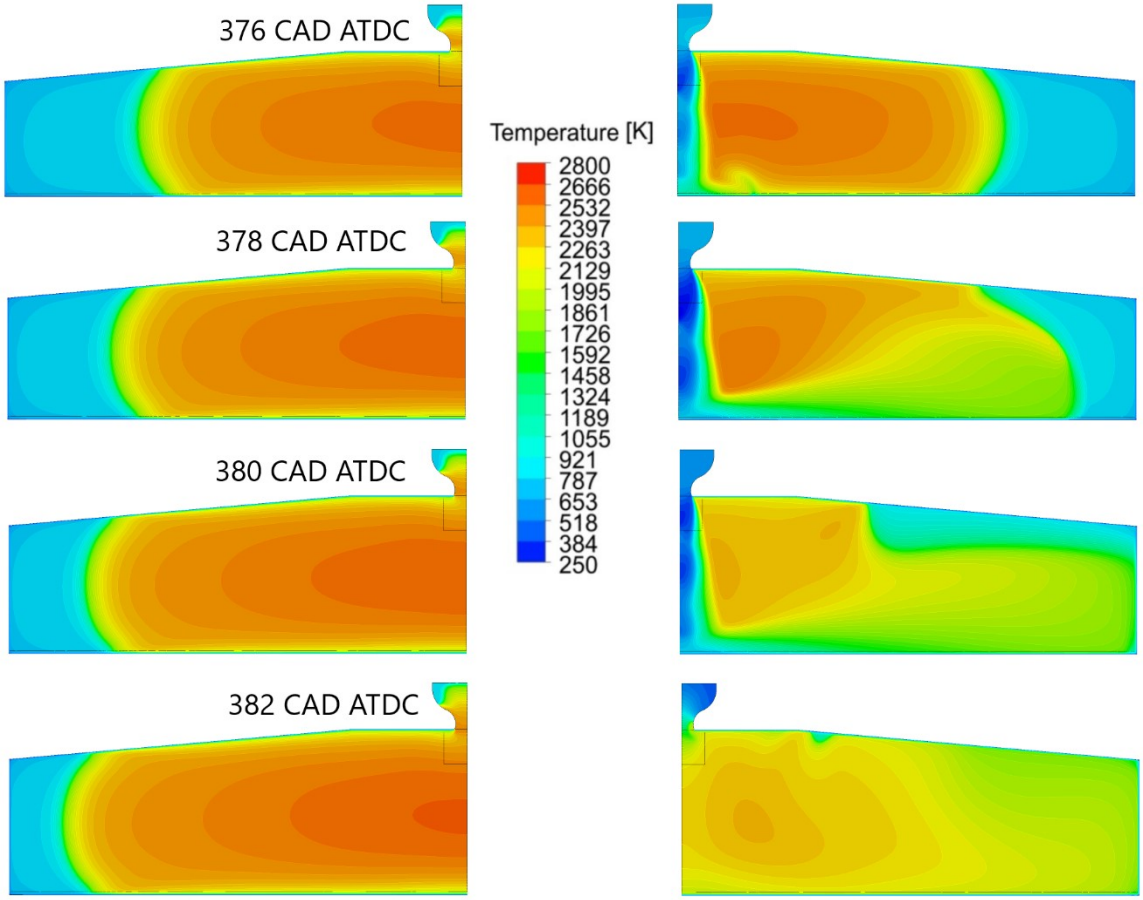

Figure 5.10: Flame speed without water injection and with water injection at MBF25.

Finally, Table 5.3 summarizes the results obtained with the axial injector architecture, using the injection conditions A, in terms of work gain and wall heat transfer.

Table 5.3. Effects of water injection on engine work gain and wall heat transfer (Axial injector architecture, injection conditions A).

	Without water injection	MBF5	MBF15	MBF20	MBF25
Work [J]	269.3 (-)	80.3 (-70%)	300.92 (+11.8%)	296.4 (+10.1%)	271.58 (+0.9%)
Wall heat transfer [J]	201.1 (-)	141.3 (-30%)	462.6 (+130%)	464.7 (+131%)	397.2 (+98%)

Injection conditions B

The injection conditions B are characterized by a lower injection pressure and a higher injection temperature. The impact of these two factors on wall heat transfer and flame extinction/enhancement are going to be discussed in this paragraph.

The different inlet thermodynamic conditions with respect to the previous case will affect the mass flow rate, which in turn will change the WID. Table 5.4 shows the WID, SOI and mass flow rate for injection conditions B.

Table 5.4. Water Injection Duration (WID) and Start of Injection (SOI) for injection conditions B (axial injector).

	MBF5	MBF15	MBF25
WID [CAD]	6.7	6.7	6.7
SOI [CAD ATDC]	7.7	12.0	15.8
Mass flow rate [kg/s]	0.0519	0.0519	0.0519

Figure 5.11 shows the engine working cycles without water injection and with water injection at different injection timings, with the axial injector and injection conditions B. The only case where the flame is quenched is MBF5. As visible from the pressure trace, combustion is slowed down by water injection, but it still goes on when water injection stops. For the injection timings of MBF15 and MBF25 a combustion enhancement is observed, with a higher pressure-peak reached by the MBF15 configuration.

Figure 5.12 shows the wall heat transfer without water injection and with water injection at the different MBFs simulated. As already observed for the injection conditions A, water injection always enhances the overall wall heat transfer, in this case even when the flame is partially quenched (i.e. MBF5). Namely, at MBF5 the wall heat transfer is increased by 34% with respect to the case without water injection, while it is increased by 113% and 121% with injection at MBF15 and MBF25, respectively. As in the case of injection conditions A, the piston experiences the highest wall heat transfer gain, due to the direct impingement of the water jet on its surface.

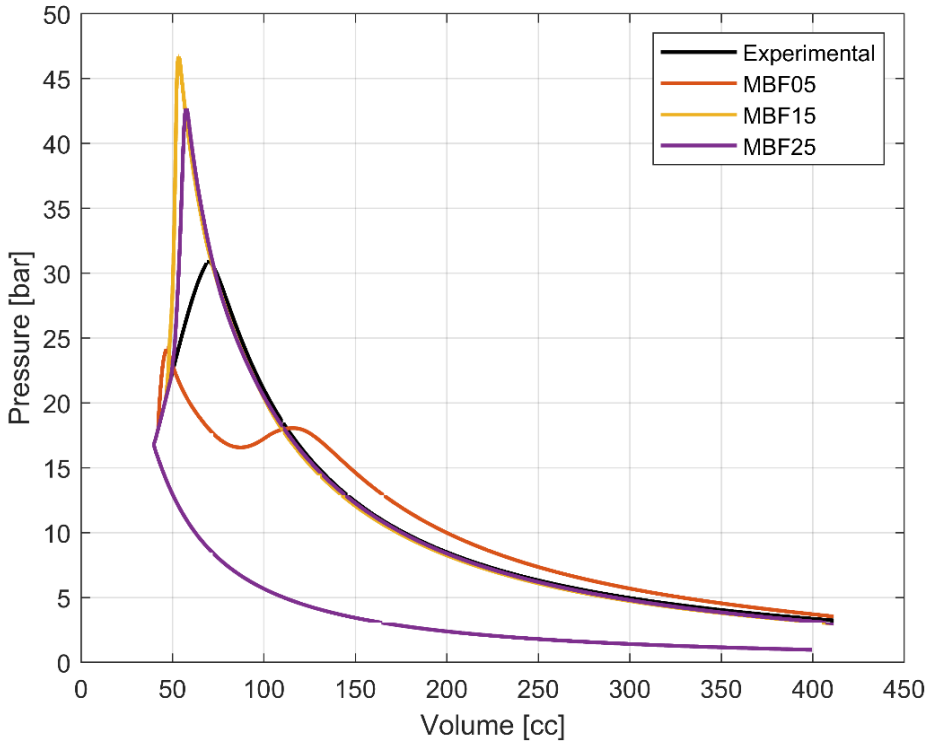

Figure 5.11. In-chamber pressure versus engine volume without water injection and for different MBFs with the axial injector architecture with injection conditions B.

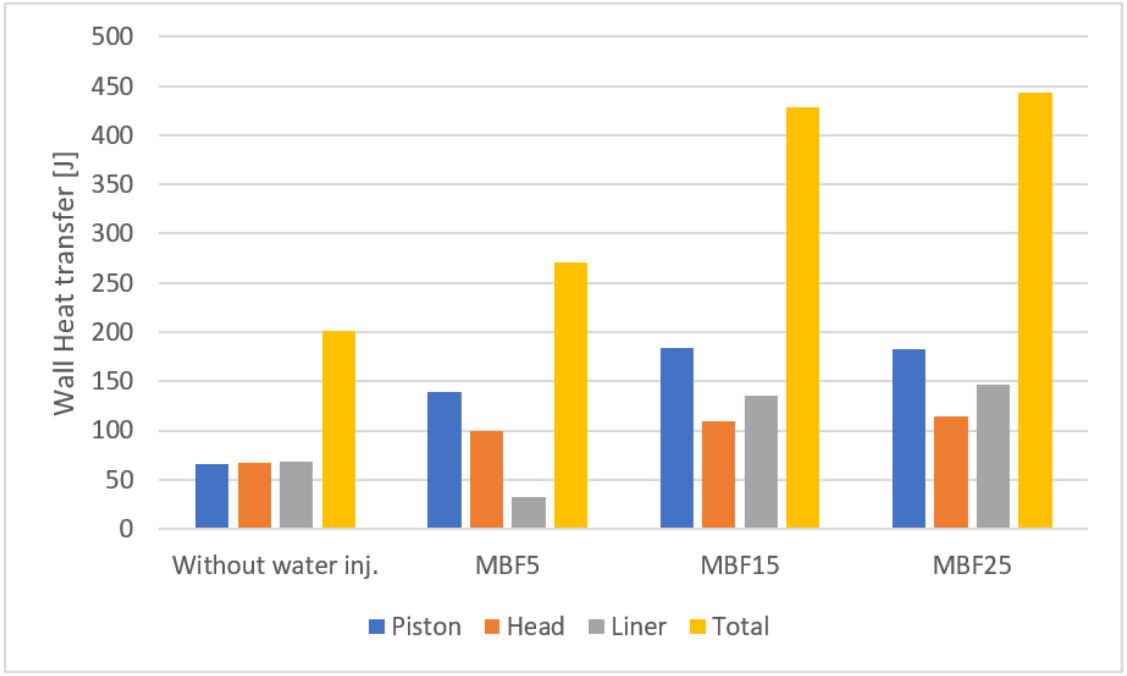

Figure 5.12: Total wall heat transfer without water injection and with water injection at different MBFs (Axial injector, injection conditions B).

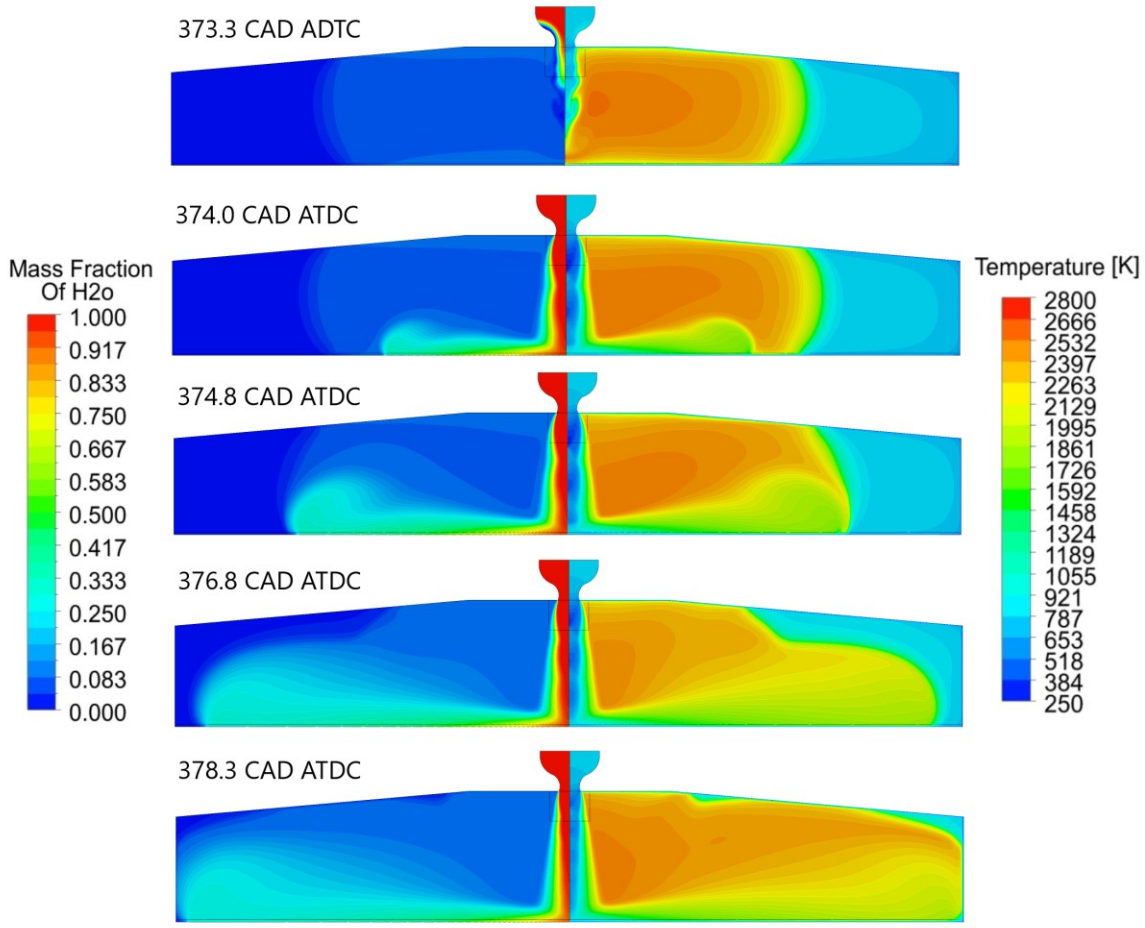

Figure 5.13: Water injection-combustion interaction transient for condition B at MBF15 (Axial injector): water mass fraction (left) and temperature (right) contour plot.

Figure 5.13 shows the injection transient, in the case of injection timing at MBF15 with the injection conditions B. The lower injection pressure results in a weaker interaction with the flame front, which is not stretched as much as what has been observed with injection conditions A (Figure 5.7). This leads both to a lower combustion enhancement and a lower probability of flame quenching.

Finally, the work gain and wall heat transfer are summarized in Table 5.5, while Figure 5.14 shows the work gain trend with respect to the injection timing. The injection conditions B always underperform injection conditions A, reaching a maximum work gain of +4.4% with injection timing at MBF15. In terms of wall heat transfer enhancement, injection condition B returns a lower value with respect to injection conditions A.

Table 5.5. Effects of water injection on engine work gain and wall heat transfer (Axial injector architecture, injection conditions B).

	Without water injection	MBF5	MBF15	MBF25

Work [J]	269.3 (-)	259.6 (-3.6%)	281.2 (+4.4%)	277.7 (+3.1%)
Wall heat transfer [J]	201.1 (-)	270.4 (+34%)	428.4 (+113%)	443.7 (+121%)

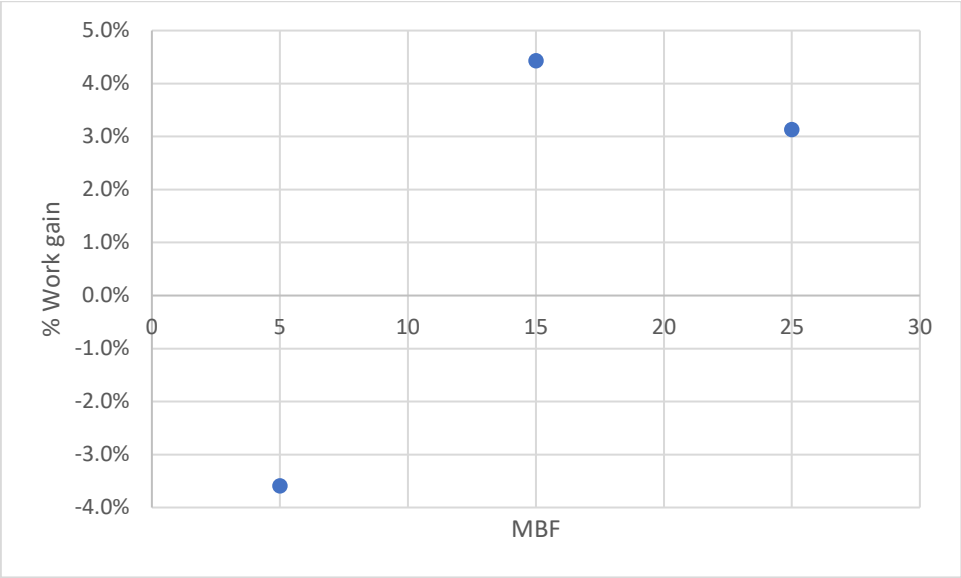

Figure 5.14: Relative work gain obtained with water injection with respect to the case without water injection (axial injector, injection conditions B).

5.5 Open nozzle injector

The different injector geometry leads to a slightly different in-chamber turbulence level and flow field, especially close to the injector. Since the ignition spot is close to the injector, the different turbulence level will have a significant effect on the numerical combustion. Therefore, the combustion model parameters have been adjusted in order to match experimental data. The EDC model constants C_ξ and C_τ have been set to 9.1 and 2.2 respectively. Figure 5.15 compares experimental and numerical pressure trace (A) and the heat release rate (B).

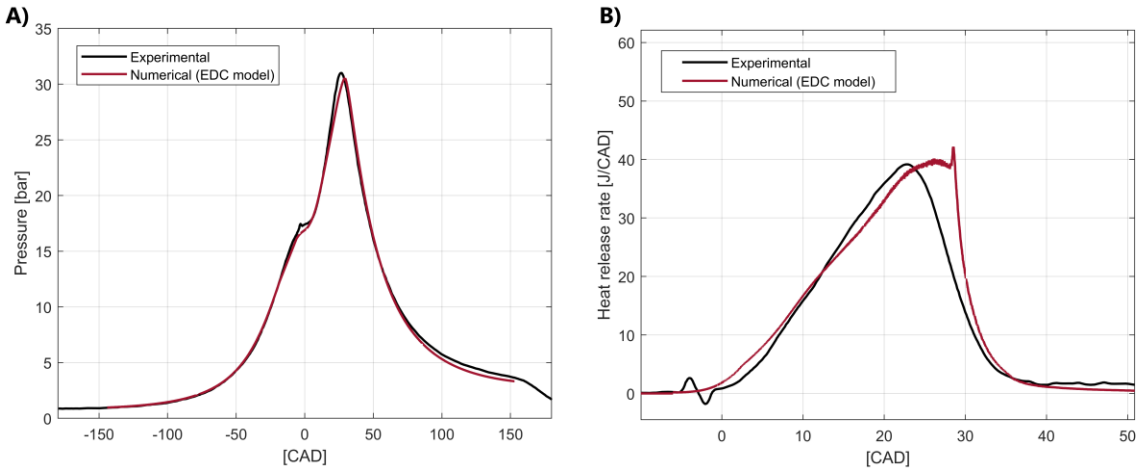

Figure 5.15: A) In chamber pressure vs CAD: Experimental [29] vs CFD model (EDC); B) Heat release rate vs CAD: Experimental [29] vs CFD model (open nozzle injector geometry).

Since the simulations of the axial injector architecture suggest that injection conditions A performs better in terms of work gain obtained, for the open nozzle injector architecture only these injection conditions have been addressed.

Table 5.6 shows the WID, the SOI and the mass flow rate for the open nozzle injector. Respect to the axial injector, the open nozzle injector returns a lower mass flow rate, which results in a longer WID in order to inject the same amount of water. The results presented in chapter 3 show how a longer WID results in a lower work and efficiency gain. Nonetheless, the quasi-dimensional model used did not take into account water injection-combustion interaction and the enhanced wall heat transfer. Therefore, in order to have a higher efficiency gain with the open nozzle injector, it should lead to a lower wall heat transfer and/or a faster combustion process with respect to the axial injector.

Table 5.6. Water Injection Duration (WID) and Start of Injection (SOI) for injection conditions A (open nozzle injector).

	MBF5	MBF15	MBF25
WID [CAD]	7.2	7.2	7.2
SOI [CAD ATDC]	7.5	13.0	16.5
Mass flow rate [kg/s]	0.0531	0.0531	0.0531

Figure 5.16 shows the engine working cycles without water injection and with water injection at different MBFs. A higher in-chamber pressure peak is reached when water injection is applied, for all the MBFs tested. This follows the same behavior seen with the axial injector architecture, but in this case a higher pressure-peak is reached even at MBF5. This is due to the lower mass flow rate, which delays the water jet-flame front interaction at a given MBF. For all the three MBFs tested, water injection results in a benefit in terms of work gain, as shown in Figure 5.17. In particular the optimal configuration is found at MBF5, with a work gain of 6.6% with respect to the case without water injection. It should be also pointed out that a higher work gain could be achieved advancing the SOI beyond MBF5.

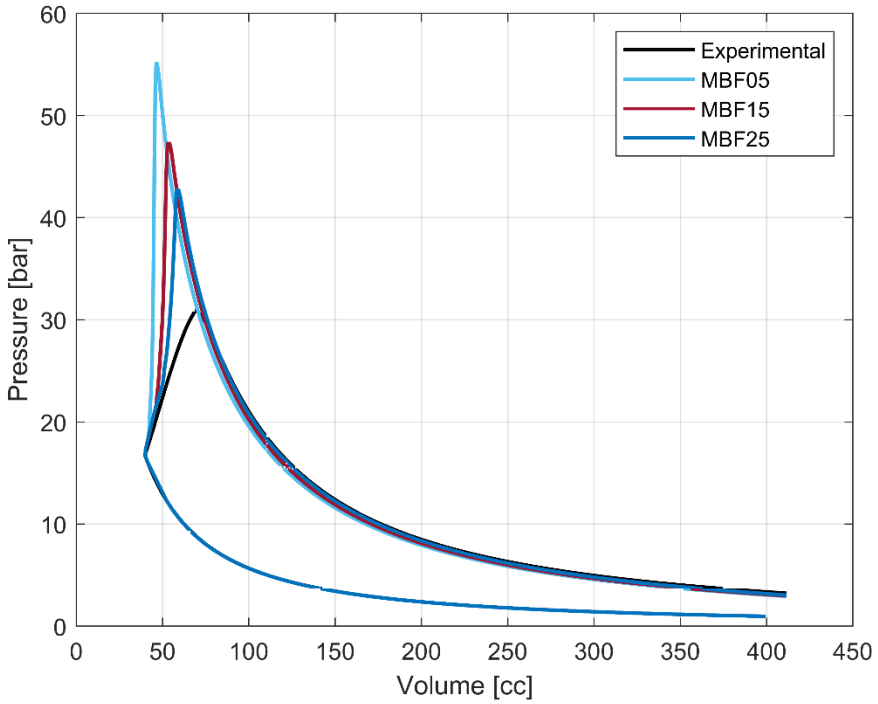

Figure 5.16: In-chamber pressure versus engine volume without water injection and for different MBFs with the open nozzle injector architecture with injection conditions A.

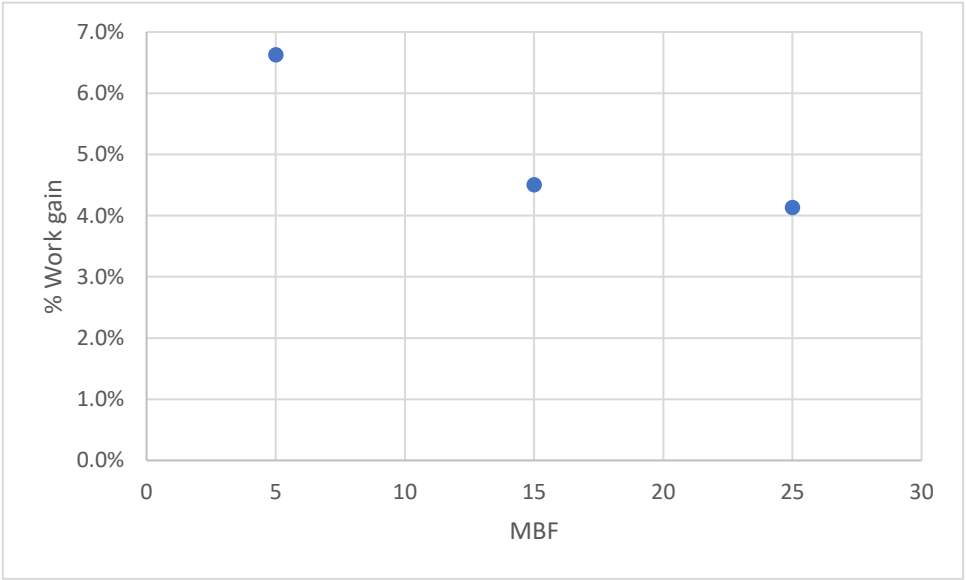

Figure 5.17: Relative work gain obtained with water injection with respect to the case without water injection (open nozzle injector, injection conditions A).

As already seen for the axial injector, also with the open nozzle injector a higher wall heat transfer is found, as shown by Figure 5.18. Nonetheless, the wall heat transfer gain is sensibly lower than what obtained with the axial injector architecture. Specifically, at MBF15 with the axial injector architecture we have a +130% wall heat transfer gain with respect to the case without water injection, while the wall heat transfer gain is equal to +71% with the open nozzle injector in the same injection conditions. Another difference between the two architectures is that, while with the axial injector the highest wall heat

transfer gain is experienced by the piston, with the open nozzle injector it is experienced by the head surface. This is due to the different jet structure, which in the case of the open nozzle architecture follows the head surface, as visible in Figure 5.19.

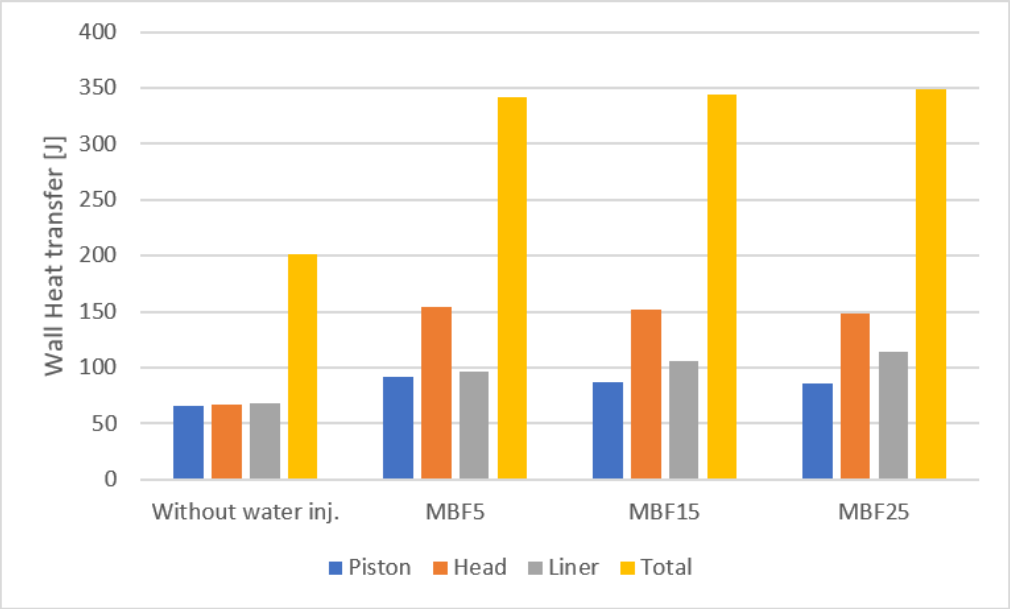

Figure 5.18: Total wall heat transfer without water injection and with water injection at different MBFs (Open nozzle injector, injection conditions A).

Figure 5.19 shows the water injection transient in terms of in-chamber temperature and water mass fraction, with SOI at MBF5. Once the water jet reaches the combustion chamber, it follows the head surface moving in radial direction. The flame front is being stretched by the water jet, which increases the flame surface, enhancing combustion. Particularly, the combustion enhancement can be seen as the combination of two effects: one is the increased flame speed, since the water jet pushes the flame front, the other is the increased flame surface. The result of the combustion enhancement is a higher in-chamber pressure, which leads to a higher engine work.

Finally, Table 5.7 summarizes the results obtained with the open nozzle injector architecture, using the injection conditions A, in terms of work gain and wall heat transfer.

Table 5.7. Effects of water injection on engine work gain and wall heat transfer (Open nozzle injector architecture, injection conditions A).

	Without water injection	MBF5	MBF15	MBF25
Work [J]	269.3 (-)	287.1 (+6.6%)	281.4 (+4.5%)	280.4 (+4.1%)

Wall heat transfer [J]	201.1 (-)	342.3 (+70%)	343.7 (+71%)	349.1 (+74%)

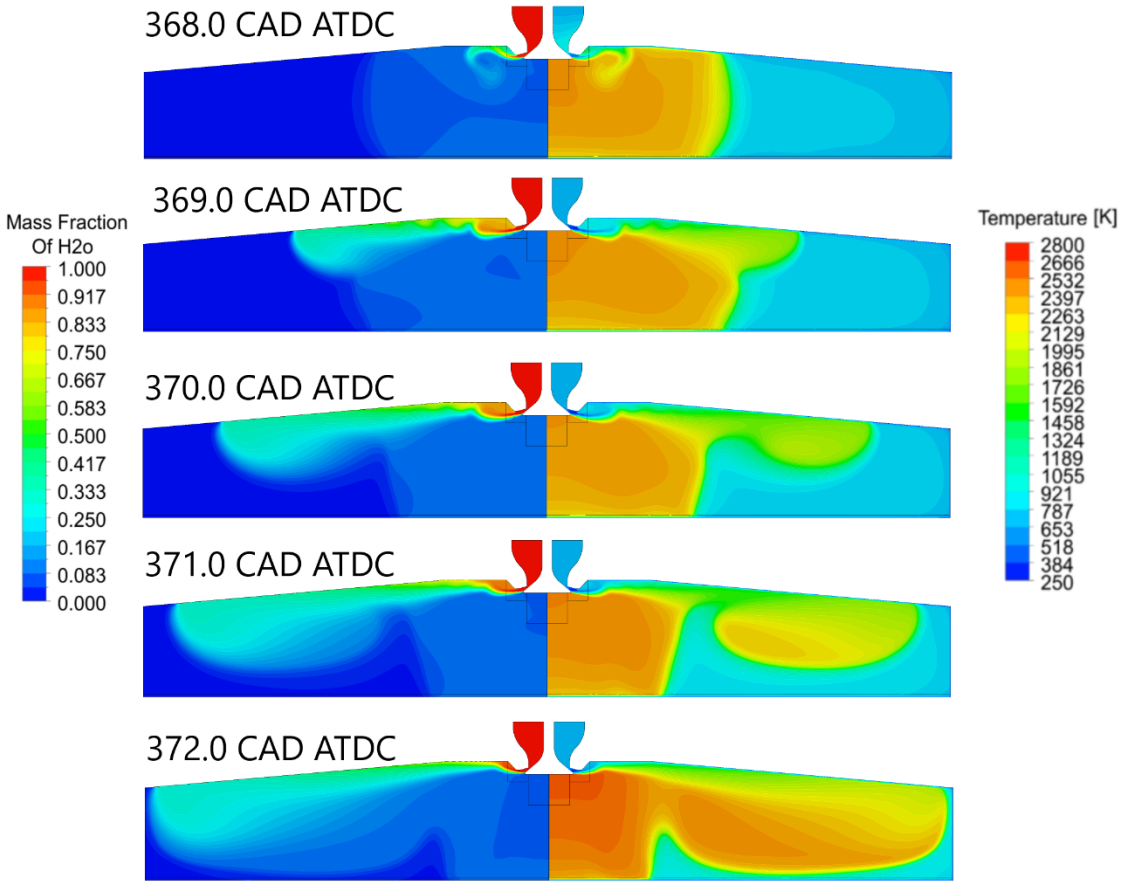

Figure 5.19. Water injection-combustion interaction transient for condition A at MBF5 (Open Nozzle injector): water mass fraction (left) and temperature (right) contour plot.

5.6 Effects on pollutant emissions

The combustion model used in the present chapter utilizes a chemical kinetic mechanism which determines the chemical composition of combustion products based on the instantaneous thermodynamic and chemical composition of the mixture. When injecting an amount of water equal to 4 times the amount of fuel present into the combustion chamber, a substantial difference in terms of chemical composition and temperature distribution is found. This may lead to different results in terms of pollutant formation.

In order to fairly compare the pollutant emissions with and without water injection, since with water injection the engine has a higher power output, the pollutant emissions

will be normalized with respect to the engine work obtained by each configuration. In other words, the pollutants mass per unit of work will be given. Figure 5.20 shows the mass per unit of work of some pollutants at the Exhaust Valve Start Opening (EVSO). Without water injection a lower amount of CO_2 is found. On the other hand, a higher amount of hydrocarbon radicals (HCO and CH) and carbon monoxide (CO) are present. Therefore, the lower production of CO_2 without water injection is mainly due to the less complete combustion process, which leads to a higher production of the highly undesirable hydrocarbons and carbon monoxide. The only exception is found with the axial injector at the injection conditions B, which produce a substantially higher amount of CO and HCO respect to the case without water injection and to all other water injection configurations. The axial injector architecture at the injection conditions B also returns a lower work gain, making it the overall worst of all analyzed configurations in terms of pollutant emissions. Leaving out the axial injector with injection conditions B, water injection either do not affect or lowers pollutant emissions. In particular, the amount of NO_2 and N_2O produced per unit of work is not significantly affected by water injection, while the amount of CO, CH, HCO and NO produced are about 1 order of magnitude lower.

Figure 5.20. Pollutants inside the combustion chamber at EVSO. The mass of each pollutant is referred to the work obtained by the engine.

Nomenclature

ORCs: Organic Rankine Cycles

IBC: Inverted Brayton Cycle

RC: Rankine Cycle

ORC: Organic Rankine Cycle

CAD: Crank Angle Degree

IMEP: Indicated Mean Effective Pressure

EGR: Exhaust Gases Recirculation

CFD: Computational Fluid Dynamics

WISE: Water Injection Spark Engine

PFI: Port Fuel Injection

SI: Spark Ignition

W/F: Water/Fuel ratio

SOI: Start Of Injection

ODE: Ordinary Differential Equation

WID: Water Injection Duration

IVSO: Intake Valve Start Opening

IVFO: Intake Valve Full Opening

IVSC: Intake Valve Start Closing

IVFC: Intake Valve Full Closing

ICE: Internal Combustion Engine

SA: Spark Advance

BTDC: Before Top Dead Center

GA: Genetic Algorithm

ECFM: Extended Coherent Flamelet Model

EDC: Eddy-Dissipation-Concept

MBF: Mass Fraction Burned

EVSO: Exhaust Valve Start Opening

References

[1] Kalghatgi, G. (2018). Is it really the end of internal combustion engines and petroleum in transport?. Applied energy, 225, 965-974, Doi: 10.1016/j.apenergy.2018.05.076.

[2] EIA, International energy outlook 2019 with projections to 2050, U.S. Energy Information Administration, Washington, DC, [Online; accessed 18-february-2020] (2019). URL https://www.eia.gov/outlooks/ieo/pdf/ieo2019.pdf

[3] Heywood, J. B. 1988, Internal Combustion Engines Fundamentals, McGraw-Hill.

[4] Watson, N. (1988). Turbocharged Engines. In *Internal Combustion Engines* (pp. 157-212). Academic Press.

[5] Gheorghiu, V. (2015). *Ultra-downsizing of internal combustion engines* (No. 2015-01-1252). SAE Technical Paper. Doi: 10.4271/2015-01-1252

[6] Teng, H., Regner, G., & Cowland, C. (2007). *Waste heat recovery of heavy-duty diesel engines by organic Rankine cycle part I: hybrid energy system of diesel and Rankine engines* (No. 2007-01-0537). SAE Technical Paper. Doi: 10.4271/2007-01-0537

[7] Di Battista, D., Fatigati, F., Carapellucci, R., & Cipollone, R. (2019). Inverted Brayton Cycle for waste heat recovery in reciprocating internal combustion engines. Applied Energy, 253, 113565. Doi: 10.1016/j.apenergy.2019.113565

[8] Zorbas, K. T., Hatzikraniotis, E., & Paraskevopoulos, K. M. (2007, September). Power and efficiency calculation in commercial TEG and application in wasted heat recovery in automobile. In *Proc. of 5th European Conference on Thermoelectrics* (Vol. 8, p. 2007).

[9] Haidar, J. G., & Ghojel, J. I. (2001, June). Waste heat recovery from the exhaust of low-power diesel engine using thermoelectric generators. In *Proceedings ICT2001. 20 International Conference on Thermoelectrics (Cat. No. 01TH8589)* (pp. 413-418). IEEE. Doi: 10.1109/ICT.2001.979919

[10] Bombarda, P., Invernizzi, C. M., & Pietra, C. (2010). Heat recovery from Diesel engines: A thermodynamic comparison between Kalina and ORC cycles. *Applied thermal engineering*, *30*(2-3), 212-219. Doi: 10.1016/j.applthermaleng.2009.08.006

[11] Vaja, I., & Gambarotta, A. (2010). Internal combustion engine (ICE) bottoming with organic Rankine cycles (ORCs). *Energy*, *35*(2), 1084-1093. Doi: 10.1016/j.energy.2009.06.001

[12] Uusitalo, A., Honkatukia, J., Turunen-Saaresti, T., & Larjola, J. (2014). A thermodynamic analysis of waste heat recovery from reciprocating engine power plants by means of Organic Rankine Cycles. *Applied thermal engineering*, *70*(1), 33-41. Doi: 10.1016/j.applthermaleng.2014.04.073

[13] Colonna, P., Casati, E., Trapp, C., Mathijssen, T., Larjola, J., Turunen-Saaresti, T., & Uusitalo, A. (2015). Organic Rankine cycle power systems: from the concept to current technology, applications, and an outlook to the future. *Journal of Engineering for Gas Turbines and Power*, *137*(10). Doi: 10.1115/1.4029884

[14] Rowe, M. R., & Ladd, G. T. (1946). Water injection for aircraft engines. *SAE Transactions*, 26-44. Doi: 10.4271/460192

[15] Berni, F., Breda, S., Lugli, M., & Cantore, G. (2015). A numerical investigation on the potentials of water injection to increase knock resistance and reduce fuel consumption in highly downsized GDI engines. *Energy Procedia*, *81*, 826-835. Doi: 10.1016/j.egypro.2015.12.091

[16] Hunger, M., Böcking, T., Walther, U., Günther, M., Freisinger, N., & Karl, G. (2017, December). Potential of direct water injection to reduce knocking and increase the efficiency of gasoline engines. In *International Conference on Knocking in Gasoline Engines* (pp. 338-359). Springer, Cham. Doi: 10.1007/978-3-319-69760-4_20

[17] Hoppe, F., Thewes, M., Seibel, J., Balazs, A., & Scharf, J. (2017). Evaluation of the potential of water injection for gasoline engines. *SAE International Journal of Engines*, *10*(5), 2500-2512. Doi: 10.4271/2017-24-0149

[18] Wang, C., Zhang, F., Wang, E., Yu, C., Gao, H., Liu, B., ... & Zhao, C. (2019). Experimental study on knock suppression of spark-ignition engine fuelled with kerosene via water injection. *Applied energy*, *242*, 248-259. Doi: 10.1016/j.apenergy.2019.03.123

[19] Tesfa, B., Mishra, R., Gu, F., & Ball, A. D. (2012). Water injection effects on the performance and emission characteristics of a CI engine operating with biodiesel. *Renewable Energy*, *37*(1), 333-344. Doi: 10.1016/j.renene.2011.06.035

[20] Ayhan, V., & Ece, Y. M. (2020). New application to reduce NOx emissions of diesel engines: Electronically controlled direct water injection at compression stroke. *Applied Energy*, *260*, 114328. Doi: 10.1016/j.apenergy.2019.114328

[21] Wang, Z., Shi, S., Huang, S., Tang, J., Du, T., Cheng, X., ... & Chen, J. Y. (2018). Effects of water content on evaporation and combustion characteristics of water emulsified diesel spray. *Applied energy*, *226*, 397-407. Doi: 10.1016/j.apenergy.2018.06.023

[22] Şahin, Z., Tuti, M., & Durgun, O. (2014). Experimental investigation of the effects of water adding to the intake air on the engine performance and exhaust emissions in a DI automotive diesel engine. *Fuel*, *115*, 884-895. Doi: 10.1016/j.fuel.2012.10.080

[23] Serrano, J., Jiménez-Espadafor, F. J., Lora, A., Modesto-López, L., Gañán-Calvo, A., & López-Serrano, J. (2019). Experimental analysis of NOx reduction through water addition and comparison with exhaust gas recycling. *Energy*, *168*, 737-752. Doi: 10.1016/j.energy.2018.11.136

[24] Zhang, Z., & Li, L. (2018). Investigation of in-cylinder steam injection in a turbocharged diesel engine for waste heat recovery and NOx emission control. *Energies*, *11*(4), 936. Doi: 10.3390/en11040936

[25] Li, L., & Zhang, Z. (2019). Investigation on steam direct injection in a natural gas engine for fuel savings. *Energy*, *183*, 958-970. Doi: 10.1016/j.energy.2019.06.182

[26] Liu, Q., Xie, M., Fu, J., Liu, J., & Deng, B. (2021). Cylinder steam injection (CSI) for internal combustion (IC) engine waste heat recovery (WHR) and its application on natural gas (NG) engine. *Energy*, *214*, 118892. Doi: 10.1016/j.energy.2020.118892

[27] Chase, M. W., Davies, C. A., Downey Jr, J. R., Frurip, D. J., McDonald, R. A., & Syverud, A. N. (1985). NIST JANAF Thermochemical Tables ver. 1.0. US Dept. of Commerce. Doi: 10.18434/T42S31

[28] Bell, I. H., Wronski, J., Quoilin, S., & Lemort, V. (2014). Pure and pseudo-pure fluid thermophysical property evaluation and the open-source thermophysical property library CoolProp. Industrial & engineering chemistry research, 53(6), 2498-2508. Doi: 10.1021/ie4033999

[29] D'Errico, G., Lucchini, T., Onorati, A., Mehl, M., Faravelli, T., Ranzi, E., ... & Vaglieco, B. M. (2007). *Development and experimental validation of a combustion model with detailed chemistry for knock predictions* (No. 2007-01-0938). SAE Technical Paper. Doi: 10.4271/2007-01-0938

[30] Dittus, F. W., & Boelter, L. M. K. (1985). Heat transfer in automobile radiators of the tubular type. *International communications in heat and mass transfer*, *12*(1), 3-22.

[31] Winterton, R. H. (1998). Where did the Dittus and Boelter equation come from?. *International journal of heat and mass transfer*, *41*(4-5), 809-810.

[32] Heat Transmission, (1942). by WH McAdams. *McGraw-Hill Book Co., New York*, *214*.

[33] B. Petukhov, A. Senin, S. Kovalev, Heat transfer in nuclear power plants, Energoatom-izdat (1986) (in Russian).

[34] Taler, D. (2013). Experimental determination of correlations for average heat transfer coefficients in heat exchangers on both fluid sides. *Heat and Mass Transfer*, *49*(8), 1125-1139. Doi: 10.1007/s00231-013-1148-5

[35] Cantiani, A., Viggiano, A., & Magi, V. (2019). *How to Improve SI Engine Performances by Means of Supercritical Water Injection* (No. 2019-24-0235). SAE Technical Paper. Doi: 10.4271/2019-24-0235

[36] Andruskiewicz, P., Najt, P., Durrett, R., Biesboer, S., Schaedler, T., & Payri, R. (2018). Analysis of the effects of wall temperature swing on reciprocating internal combustion engine processes. *International Journal of Engine Research*, *19*(4), 461-473. Doi: 10.1177/1468087417717903

[37] Kosaka, H., Wakisaka, Y., Nomura, Y., Hotta, Y., Koike, M., Nakakita, K., & Kawaguchi, A. (2013). Concept of "temperature swing heat insulation" in combustion chamber walls, and appropriate thermo-physical properties for heat insulation coat. *SAE International Journal of Engines*, *6*(1), 142-149. Doi: 10.4271/2013-01-0274

[38] Kogo, T., Hamamura, Y., Nakatani, K., Toda, T., Kawaguchi, A., & Shoji, A. (2016). *High Efficiency Diesel Engine with Low Heat Loss Combustion Concept-Toyota's Inline 4-Cylinder 2.8-Liter ESTEC 1GD-FTV Engine* (No. 2016-01-0658). SAE Technical Paper. Doi: 10.4271/2016-01-0658

[39] Wakisaka, Y., Inayoshi, M., Fukui, K., Kosaka, H., Hotta, Y., Kawaguchi, A., & Takada, N. (2016). Reduction of heat loss and improvement of thermal efficiency by application of "temperature swing" insulation to direct-injection diesel engines. *SAE International Journal of Engines*, *9*(3), 1449-1459. Doi: 10.4271/2016-01-0661

[40] Kumar, C. R., & Nagarajan, G. (2012). Performance and emission characteristics of a low heat rejection spark ignited engine fuelled with E20. *Journal of mechanical science and technology*, *26*(4), 1241-1250. Doi: 10.1007/s12206-012-0206-0

[41] Hoffman, M. A., Lawler, B. J., Güralp, O. A., Najt, P. M., & Filipi, Z. S. (2015). The impact of a magnesium zirconate thermal barrier coating on homogeneous charge compression ignition operational variability and the formation of combustion chamber deposits. *International Journal of Engine Research*, *16*(8), 968-981. Doi: 10.1177/1468087414561274

[42] Launder, B. E., & Spalding, D. B. (1983). The numerical computation of turbulent flows. In *Numerical prediction of flow, heat transfer, turbulence and combustion* (pp. 96-116). Pergamon. Doi: 10.1016/B978-0-08-030937-8.50016-7

[43] Ansys® Fluent, release 19.2, Theory Guide 19.2 ANSYS, Inc.

[44] Poinsot, T. and Veynante, D., "Theoretical and Numerical Combustion, 2nd edition" (New Yoork, McGraw-Hill, 2005), ISBN: 978-1930217102

[45] Wang, H., Yao, M., & Reitz, R. D. (2013). Development of a reduced primary reference fuel mechanism for internal combustion engine combustion simulations. *Energy & Fuels*, *27*(12), 7843-7853. Doi: 10.1021/ef401992e

[46] Saxena, P., & Williams, F. A. (2007). Numerical and experimental studies of ethanol flames. *Proceedings of the Combustion Institute*, *31*(1), 1149-1156. Doi: 10.1016/j.proci.2006.08.097

[47] Metghalchi, M., & Keck, J. C. (1982). Burning velocities of mixtures of air with methanol, isooctane, and indolene at high pressure and temperature. *Combustion and flame*, *48*, 191-210. Doi: 10.1016/0010-2180(82)90127-4

[48] Hayder, M. E., Varma, A. K., & Bracco, F. V. (1985). A limit to TDC turbulence intensity in internal combustion engines. *Journal of Propulsion and Power*, *1*(4), 300-308. Doi: 10.2514/3.22797

[49] Zuckerman, N., & Lior, N. (2006). Jet impingement heat transfer: physics, correlations, and numerical modeling. *Advances in heat transfer*, *39*, 565-631. Doi: 10.1016/S0065-2717(06)39006-5

[50] Craft, T. J., Graham, L. J. W., & Launder, B. E. (1993). Impinging jet studies for turbulence model assessment—II. An examination of the performance of four turbulence models. *International Journal of Heat and Mass Transfer*, *36*(10), 2685-2697. Doi: 10.1016/S0017-9310(05)80205-4

[51] Behnia, M., Parneix, S., & Durbin, P. (1997). Accurate modeling of impinging jet heat transfer. Center for Turbulence Research, Annual Research Briefs, 149-164.

[52] Bonelli, F., Viggiano, A., & Magi, V. (2012, May). A numerical analysis of hydrogen underexpanded jets. In *Internal Combustion Engine Division Spring Technical Conference* (Vol. 44663, pp. 681-690). American Society of Mechanical Engineers. Doi: 10.1115/ICES2012-81068

[53] Maté, B., Graur, I. A., Elizarova, T., Chirokov, I., Tejeda, G., Fernandez, J. M., & Montero, S. (2001). Experimental and numerical investigation of an axisymmetric supersonic jet. *Journal of Fluid Mechanics*, *426*, 177-197. Doi: 10.1017/S0022112000002329

[54] Yu, J., Vuorinen, V., Kaario, O., Sarjovaara, T., & Larmi, M. (2013). Visualization and analysis of the characteristics of transitional underexpanded jets. *International Journal of Heat and Fluid Flow*, *44*, 140-154. Doi: 10.1016/j.ijheatfluidflow.2013.05.015

[55] Magnussen, B. (1981, January). On the structure of turbulence and a generalized eddy dissipation concept for chemical reaction in turbulent flow. In *19th aerospace sciences meeting* (p. 42). Doi: 10.2514/6.1981-42

Part II

Organic Rankine Cycle

Among low-enthalpy energy recovery systems, Organic Rankine Cycles (ORCs) are widely used. An ORC follows the same working principles of a steam Rankine Cycle, but exploits the low boiling point of organic fluids to work with substantially lower temperature energy sources. Therefore, ORCs can be used as energy recovery devices in many applications, such as in steel, cement and glass production plants, in Oil&Gas sector, or in fluid machinery, such as internal combustion engines. In this chapter a quasi-dimensional model of an ORC unit is presented, with a particular focus on the expander. The model is then used to estimate the potential energy recovery achievable by coupling an ORC unit to an internal combustion engine.

Chapter 7
Organic Rankine Cycle modelling

7.1 Organic Rankine Cycle as a tool for waste heat recovery

A relatively large amount of energy can be recovered from waste heat of internal combustion engines, gas turbines and various industrial processes, such as cement, steel, glass production, oil and gas sector [1-4], etc. For low-enthalpy energy recovery, Organic Rankine Cycles (ORCs) are commonly used since they provide better performances when compared with other available technologies, such as Stirling engines, thermo-electric generators, and inverted Brayton cycles [5]. Campana et al. [1] estimated that up to 20 TWh per year of thermal energy could be recovered by means of Organic Rankine Cycles from a relatively few industrial plants selected in Europe, leading to a 7.6 Mton reduction in terms of CO2 emissions.

The ideal cycle of an ORC is shown in Figure 7.1. It includes an isentropic compression (1-2), an isobaric heat addition (2-3), an isentropic expansion (3-4) and an isobaric heat rejection (4-1). The components needed to realize this basic thermodynamic cycle are: a pump to pressurize the liquid (1-2), a heat exchanger (boiler) to transfer heat to the working fluid (2-3), an expander (3-4), and a condenser (4-1). The components and their connection are displayed in Figure 7.2.

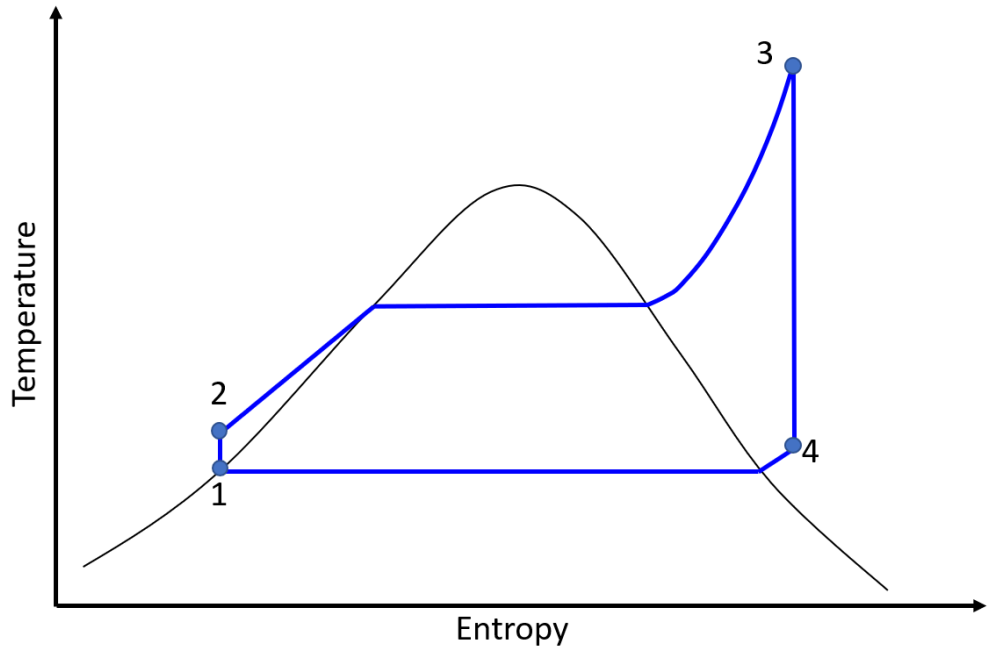

Figure 7.1: Organic Rankine Cycle ideal cycle (1-2 isentropic compression 2-3 heat addition, 3-4 isentropic expansion, 4-1 isobaric heat rejection)

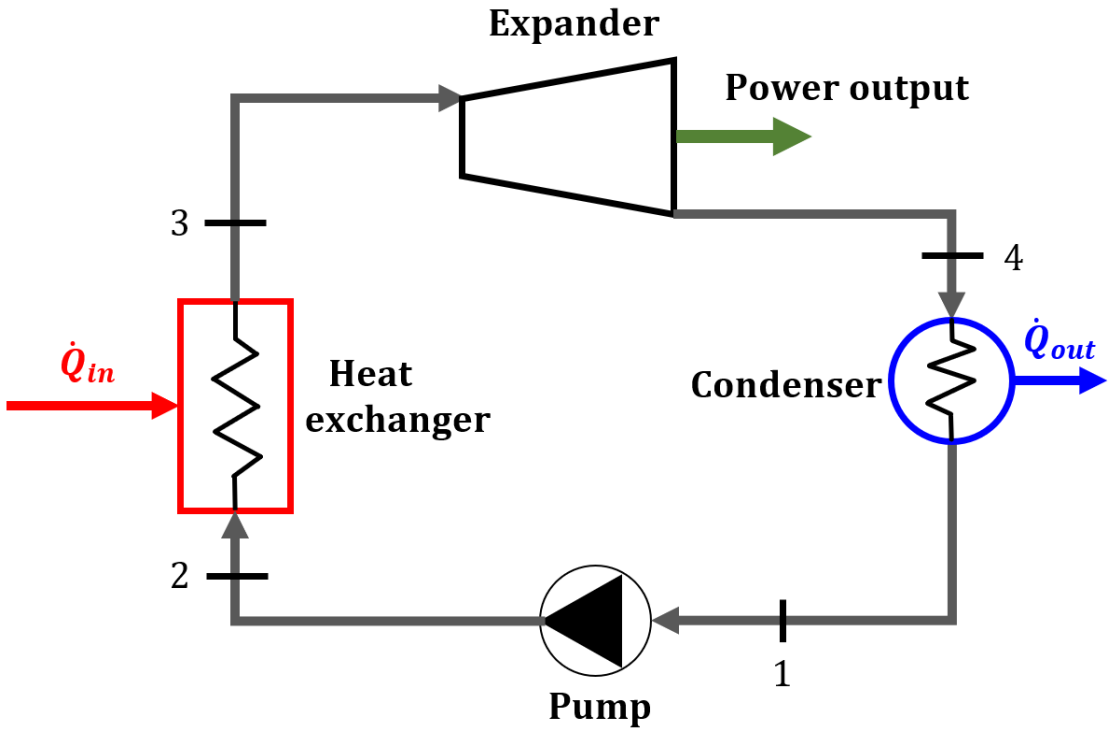

Figure 7.2: Organic Rankine cycle unit layout.

In this chapter the various components of an ORC unit will be described with appropriate mathematical models, then the ORC unit will be coupled with the internal combustion engine quasi-dimensional code (WISE) presented in Chapter 3, in order to evaluate the potential waste heat energy recovery. The results will be compared with the supercritical water direct injection energy recovery system described in Part I.

7.2 The scroll expander

One of the ORCs key components is the expander, since it converts energy into useful work. For ORCs with a mechanical power output above 50 kW, radial inflow turbines give the best performances, whereas, for small and micro ORC units, volumetric expanders are preferred [6-8]. Among volumetric expanders, scroll expanders are widely used in such units, thanks to their high efficiency, simple manufacturing, lightweight, low noise and low vibrations [8-9]. In recent years, the research has focused on the development of mathematical models that help to predict the scroll expander performances under different operating conditions. Ma et al. [10] developed a scroll expander model that takes into account the friction between stator and rotor during their relative motion. With such a model, it is possible to determine the expander rotating speed and mass flow rate for specific load conditions. Yang et al. [11] have used a quasi-dimensional model to compare the performances of a scroll expander operating with different working fluids. In particular, their work focuses on the performances obtained by employing R1233zd(e) fluid, which may replace the common working fluid R245fa. The results have shown a similar behavior for the two working fluids, with a slightly better isentropic efficiency obtained with R245fa. Hence, 245fa can be considered as a valid alternative working fluid. Zhang et al. [12] have studied the effects of specific operating conditions (inlet pressure and temperature) and geometric parameters (clearance and vanes height to pitch ratio) on the expander performances. Their study found that, for a given speed, the volumetric efficiency is the same, whereas scroll expander mass flow rate and power output increase with the inlet pressure. The vanes to height pitch ratio also has a great impact on the expander performances.

7.2.1 The scroll expander geometry

In this work, the geometry of the scroll expander consists of two identical circle involute profiles for both stator and rotor. The circle involute parametric equations are:

$$x = a(\cos\varphi + \varphi \sin\varphi), \tag{7.1}$$

$$y = a(\sin\varphi - \varphi \cos\varphi), \tag{7.2}$$

where ϕ is the involute angle and a is the involute basic circle radius. Since the scroll wraps walls have a certain thickness, Eq. (7.1) and Eq. (7.2) need to be modified in order to describe the inner involute and the outer involute profile. The inner involute profile is given by Eq. (7.3) and Eq. (7.4), while the outer involute profile by Eq. (7.5) and Eq. (7.6). The parameter α determines the involute thickness s. The correlation between α and s can be easily derived from equations Eq. (7.3) and Eq. (7.4) and is given by Eq. (7.7).

$$x_i = a[\cos\varphi + (\varphi - \alpha)\sin\varphi], \quad (7.3)$$

$$y_i = a[\sin\varphi - (\varphi - \alpha)\cos\varphi], \quad (7.4)$$

$$x_o = a[\cos\varphi + (\varphi + \alpha)\sin\varphi], \quad (7.5)$$

$$y_o = a[\sin\varphi - (\varphi + \alpha)\cos\varphi], \quad (7.6)$$

$$s = 2a\alpha, \quad (7.7)$$

The involute starts at $\varphi = 0$ and ends at $\varphi = (2ns + \frac{1}{2})\pi$, where *ns* is the number of chamber pairs. In order to have a functioning scroll expander, the rotor must be rotated by π respect to the stator. This can be achieved by simply multiplying by minus 1 Eq. (7.3) to Eq. (7.6). Furthermore, since the rotor follows an orbiting path, its equations must take into account the instantaneous position. The resulting inner and outer rotor involute profiles equations are:

$$x_{ri} = x_{0r} - a[\cos\varphi + (\varphi - \alpha)\sin\varphi], \quad (7.8)$$

$$y_{ri} = y_{0r} - a[\sin\varphi - (\varphi - \alpha)\cos\varphi], \quad (7.9)$$

$$x_{ro} = x_{0r} - a[\cos\varphi + (\varphi + \alpha)\sin\varphi], \quad (7.10)$$

$$y_{ro} = y_{0r} - a[\sin\varphi - (\varphi + \alpha)\cos\varphi], \quad (7.11)$$

The rotor trajectory radius can be determined by Eq. (7.12), where c_r is the radial clearance between stator and rotor at each point:

$$r_{trj} = \pi a - 2a\alpha - c_r. \quad (7.12)$$

Hence, the rotor position at any orbiting angle θ can be determined by:

$$x_{0r} = r_{trj}\cos\theta, \quad (7.13)$$

$$y_{0r} = r_{trj}\sin\theta. \quad (7.14)$$

In order to get properly operating conditions, the involute profile of the scroll wraps needs a modified starting segment. The two modifications implemented in the model are presented in the following section. A detailed derivation of the equations can be found in [10].

Starting segment modification: circular cutter

If the stator and the rotor purely consist of circle involutes, an interference between the wraps tip will result during the rotor orbiting motion. Therefore, a modification of the starting segment is needed.

One option to avoid such an interference is to cut the first part of both involutes profile by means of a circular cutter. The circular cutter must be centered on the intersection between the left side of the involute basic circle and the x-axis to design the stator starting segment, whereas it must be centered on the intersection of the right side of the involute basic circle and the x-axis to design the rotor starting segment.

The circular cutter radius is given by:

$$r_{cc} = a(\pi - a). \tag{7.15}$$

Figure 7.3a shows the stator and rotor profiles before the modification and the circular cutter position and radius for the stator modification, whereas Figure 7.3b shows the rotor and stator profiles after the circular cutter modification.

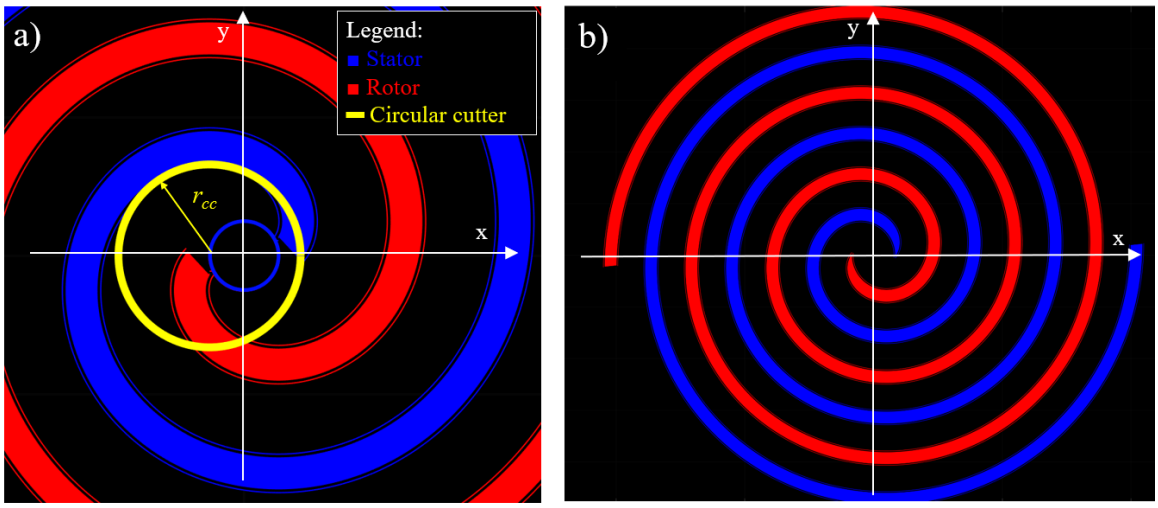

Figure 7.3: a) circular cutter position and radius for the stator modification and b) resulting scroll wraps geometries after the circular cutter modification.

The starting orbiting angle θ_{start} provides the expander starting position, which is defined as the position of the rotor that disconnects a new chamber. This angle is computed from Eq. (7.16) and Eq. (7.17):

$$\theta_{start} = \varphi_p + \frac{\pi}{2}, \tag{7.16}$$

$$(\varphi_p + \alpha)^2 + 2\cos\varphi_p + 2(\varphi_p + \alpha)\sin\varphi_p = (\pi - \alpha)^2 - 2. \tag{7.17}$$

Figure 7.4 shows the rotor starting position. It should be pointed out that, with the circular cutter geometry modification, the first chamber does not start with zero volume, but with a given initial volume.

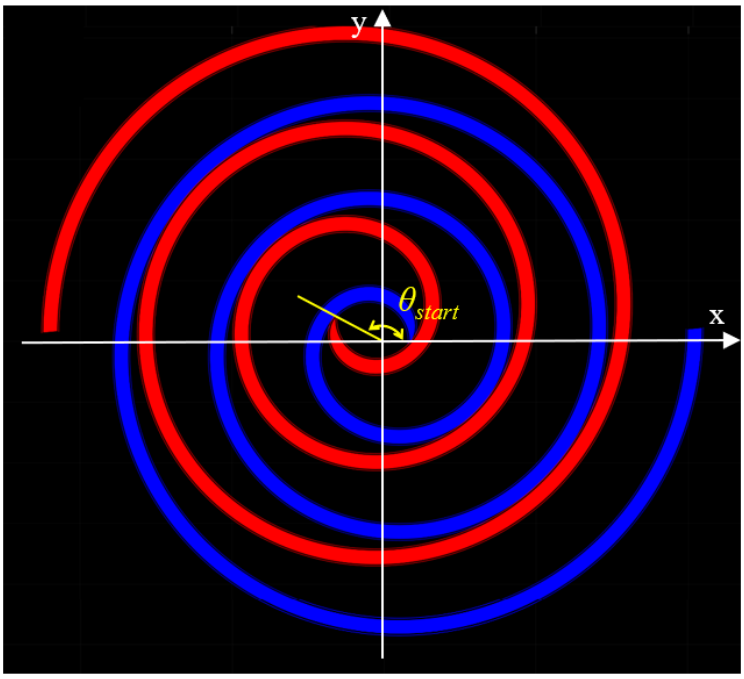

Figure 7.4: Rotor starting position with circular cutter modification.

Starting segment modification: Perfect Mesh Profile (PMP)

The PMP approach is more complex with respect to the circular cutter approach, from both manufacturing and geometrical points of view. Specifically, from a manufacturing point of view, an ad-hoc tool path is required, while the circular cutter modification just needs a cutter with a specific diameter. However, the resulting profile has no sharp edges and the first chamber volume starts from zero and continuously increases. From a geometrical point of view, the first portion of the circle involute is replaced by two circles with different radius, as shown in Figure 7.5a.

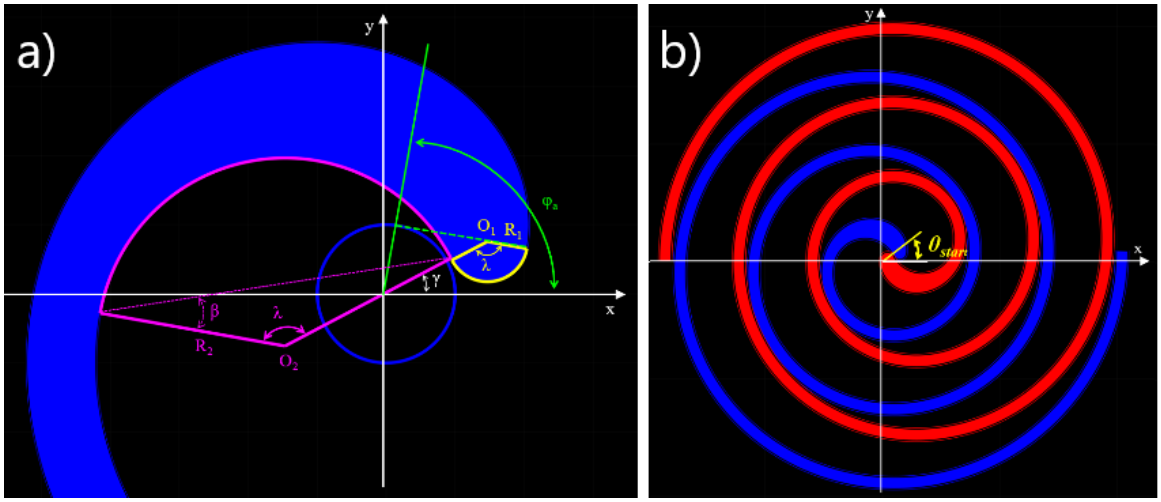

Figure 7.5: Stator with PMP modification geometry details (a) and geometry at the starting position (b).

The angle φ_a is given as an input parameter. Then, the angles β, λ and γ can be determined by the following equations:

$$\cot\beta = \varphi_a + \frac{\pi}{2}, \tag{7.18}$$

$$\lambda = \pi - 2\beta, \tag{3.19}$$

$$\gamma = \frac{\pi}{2} - \lambda. \tag{7.20}$$

The angle γ also defines the starting position for this geometry modification (Figure 7.5b).

The radius and the center of the two circles for the PMP modification are given by:

$$R_1 = a\left(\frac{1}{\sin\lambda} + \alpha - \frac{\pi}{2}\right), \tag{7.21}$$

$$R_2 = a\left(\frac{1}{\sin\lambda} - \alpha + \frac{\pi}{2}\right), \tag{7.22}$$

$$O_{1x} = \frac{a}{\sin(\pi-\lambda)}\cos\gamma, \tag{7.23}$$

$$O_{1y} = \frac{a}{\sin(\pi-\lambda)}\sin\gamma, \tag{7.24}$$

$$O_{2x} = -\frac{a}{\sin(\pi-\lambda)}\cos\gamma, \tag{7.25}$$

$$O_{2y} = -\frac{a}{\sin(\pi-\lambda)}\sin\gamma. \tag{7.26}$$

Chambers geometry

Both geometry modifications result in two sets of symmetrical chambers. Therefore, only one set of chambers is taken into account for the evaluation of the chamber volumes. Figure 7.6a shows one set of chambers of a scroll expander based on the circular cutter approach. In order to make the computations suitable for both scroll geometries, the chamber volume is evaluated by means of an analytical equation when this chamber is fully bounded within circle involute segments (yellow bounded chambers in Figure 7.6a). This chamber volume is determined by:

$$V = 2\pi a^2(\pi - 2\alpha)(\theta - 3\pi + 2\pi j)z. \tag{7.27}$$

This equation comes from the circle involute integral between the meshing points of the chamber j at the orbiting angle θ. In the equation, z is the expander height. This equation is applied from chamber 2 to chamber n-2, where n is the number of chambers. The volume of chamber n-1 is obtained from Eq. (7.27) with $\theta_{start} \leq \theta \leq 2\pi$, since at $\theta = 2\pi$ the discharge port starts to open and the chamber volume is determined as the last chamber, which is described later.

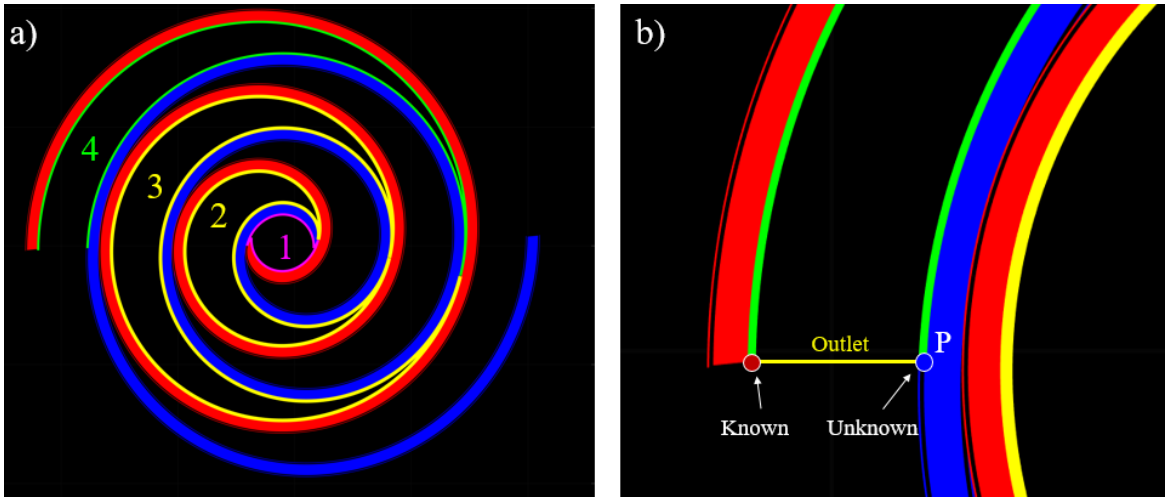

Figure 7.6: Scroll expander with circular cutter modification (stator in blue, rotor in red). One set of chambers is highlighted (a) and a detailed view of the discharge port is shown (b).

As the starting segments create the first chamber, i.e. magenta bounded chamber in Figure 7.6a, its volume is numerically determined by using the trapezium rule with an involute angle step $\Delta\varphi$ ten times lower than the orbiting angle step $\Delta\theta$, in order to avoid numerical instabilities along the chamber volume computation.

As regards the last chamber volume, i.e. green bounded chamber in Figure 7.6a, as well as the n-1 chamber for $\theta > 2\pi$, its evaluation must take into account the discharge port opening. The outlet section is assumed to be horizontal to the rotor tip, as shown in Figure 7.6b. The involute angle φ of the point P in Figure 7.6b is unknown. This angle is obtained by Eq. (7.6) by means of a Newton-Raphson method, giving as an input the y coordinate of the rotor tip. Then, the chamber volume is evaluated by employing the trapezium rule. The outlet section area is computed by multiplying the distance between the two points at the outlet by the expander height *z*. The chambers volume calculation for the PMP approach follows the same process, therefore it is not given here. The outlet area vs crank angle is shown in Figure 7.8 and Figure 7.9 for the two geometries, respectively.

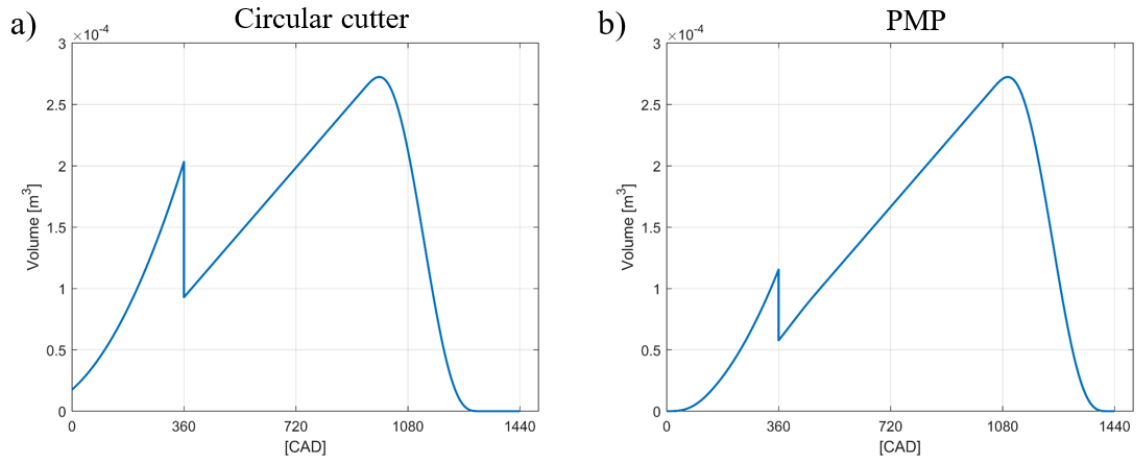

Figure 7.7: Chamber volume vs crank angle for the circular cutter (a) and PMP (b) geometries.

Figure 7.7 shows the chamber volume vs crank angle for circular cutter (Figure 7.7a) and PMP (Figure 7.7b) approaches when the number of chamber pairs is equal to 3 (Figure 7.6a). It is noticed that the circular cutter approach gives a non-zero initial volume, as opposed to the PMP approach. Moreover, the circular cutter approach returns a larger first chamber final volume at 360 CAD with respect to that based on the PMP approach. After one complete rotor rotation, i.e. 360 CAD, the first chamber splits into three chambers with the circular cutter approach and into two chambers for the PMP approach, which is represented by the discontinuities in Figure 7.7a and Figure 7.7b, respectively.

Inlet port

One of the main advantages of scroll expanders is the avoidance of moving parts, such as intake or exhaust valves. The intake consists of an inlet port on the stator base plate. During the rotor orbiting motion, the inlet port is fully opened, partially opened or fully closed. In case of partially opening, a reduction of the inlet mass flow rate and an increase of in-chamber pressure drop occur. Therefore, the influence of the inlet port shape and position on the scroll expander performances needs to be carefully addressed. In this work, the inlet port is assumed to be circular and its overlapping area with the chambers is computed at each time-step.

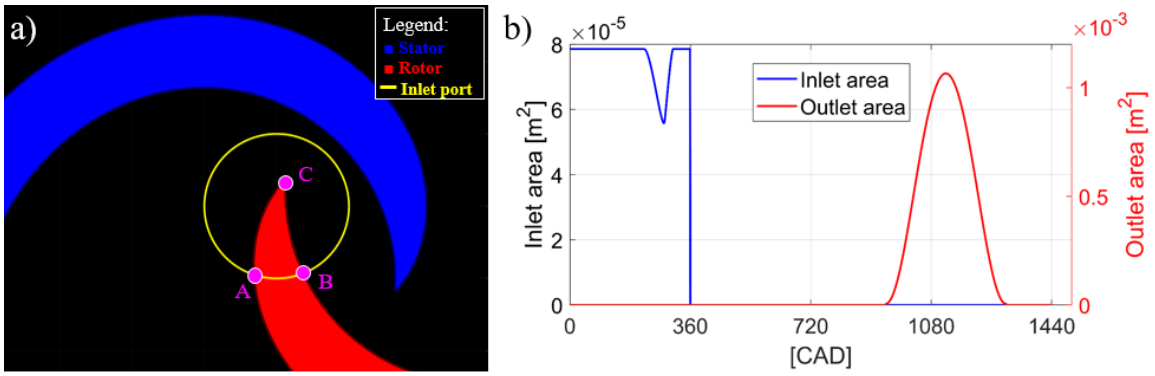

Figure 7.8: Influence of the rotor motion on the intake port area (circular cutter geometry approach): intake port partially covered by the rotor (a) and inlet and outlet area vs CAD (b).

Figure 7.8a shows a rotor position where the inlet port is partially covered by the rotor (circular cutter approach). The covered (by the rotor) inlet area is numerically determined as the integral of the closed loop A-B-C, by using the trapezium rule. Figure 7.8b shows the inlet port area vs the rotor angle. It is noted that, after one complete rotation, the inlet port area is equal to zero since there is no overlap between the chamber and the inlet port. Since the circular cutter approach returns a non-zero starting volume for the first chamber, the inlet port can be located such that the minimum overlapping area is zero, i.e. fully enclosed. Based on this configuration, each chambers pair has the same thermodynamic properties, thus the computations can be limited to only one chamber set, which results in a lower computational time. On the other hand, with the PMP approach, the initial volume of the first chamber is zero and a fraction of the inlet port area may overlap with only one of the two new starting chambers. This leads to different thermodynamic conditions for the two sets of

chambers, and the computations are performed for both chambers sets. Figure 7.9a shows a configuration where the inlet port discharges fresh gas into both the first and the second chamber, and Figure 7.9b shows the inlet port area vs crank angle. It should be noticed that the inlet area is non-zero even after one complete rotation, since a fraction of the intake port overlaps the second chamber.

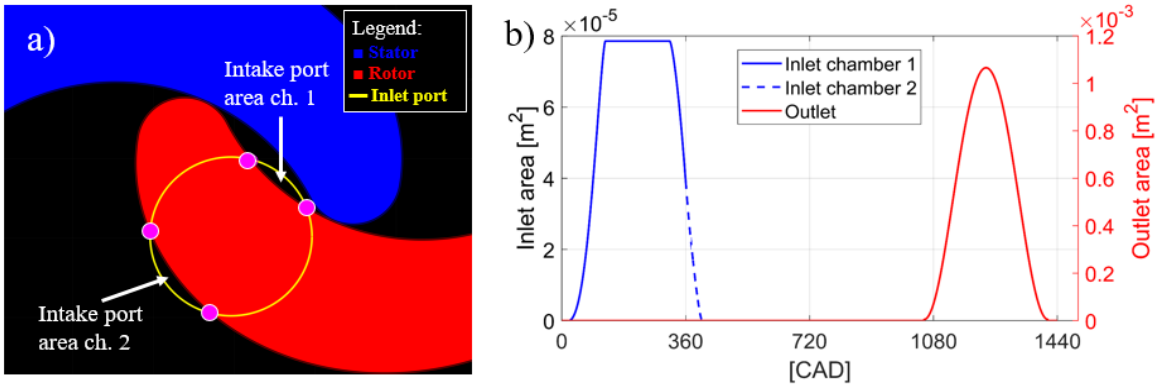

Figure 7.9: Influence of the rotor motion on the intake port area (PMP geometry approach): intake port covered by the rotor (a) and inlet and outlet area vs CAD (b).

Side walls

Side walls surface needs to be evaluated due to wall heat transfer and axial tolerance leakages. Such a surface consists of the length of the scroll wrap segment multiplied by the expander height *z*. In this work, for both geometries, the scroll wrap can be formed by a circle arc and/or a circle involute arc. The circle involute arc length l is given by:

$$l = a\left[\frac{1}{2}(\varphi_2^2 - \varphi_1^2) \pm \alpha(\varphi_2 - \varphi_1)\right], \tag{7.28}$$

where φ_1 and φ_2 represent the initial and final involute angles of the involute segment, respectively, with +α for the outer involute and -α for the inner involute.

7.3 The quasi-dimensional model for the expander

A quasi-dimensional model has been developed to analyze the performance of the expander. The model solves a system of ODE's which consists of the mass conservation equation, Eq. (7.29), and the energy conservation equation, Eq. (7.30), for each chamber:

$$\frac{dm}{dt} = \frac{dm_{inlet}}{dt} + \frac{dm_{rl}}{dt} + \frac{dm_{al}}{dt} + \frac{dm_{outlet}}{dt}, \tag{7.29}$$

$$\frac{dE}{dt} = \frac{dm_{inlet}}{dt}H_{inlet} + \frac{dm_{rl}}{dt}H_{rl} + \frac{dm_{al}}{dt}H_{al} + \\ + \frac{dm_{outlet}}{dt}H_{outlet} - pdV + \frac{dQ_w}{dt}. \tag{7.30}$$

In Eq. (7.29), m is the chamber mass, m_{inlet} is the inlet mass flow rate, m_{rl} is the radial leaks mass flow rate, m_{al} is the axial leaks mass flow rate, m_{outlet} is the outlet mass flow rate. In Eq. (7.30), E is the total internal energy, H_{inlet} is the inlet flow mass specific enthalpy, H_{rl} is the radial leaks flow mass specific enthalpy, H_{al} is the axial leaks flow mass specific enthalpy, H_{outlet} is the outlet flow mass specific enthalpy, p is the chamber pressure, V is the chamber volume and Q_w is the chamber heat transfer.

The working fluid thermodynamic properties are evaluated by using the CoolProp libraries [14]. The use of the CoolProp libraries allows an accurate determination of all the thermodynamic properties for any specific thermodynamic condition. In addition, the computations can be easily performed with a large variety of working fluids.

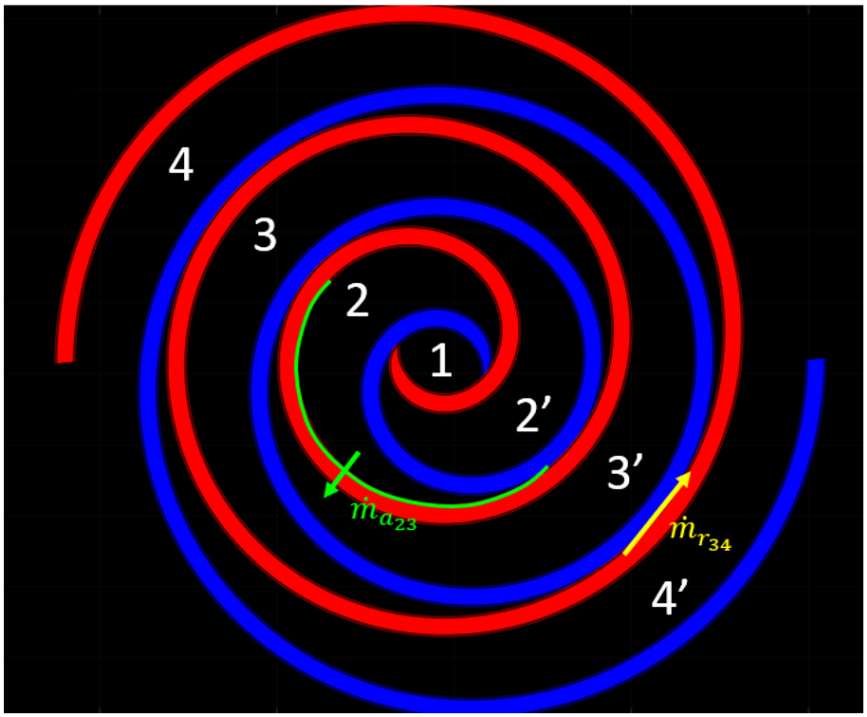

Figure 7.10: Schematization of axial leaks between chamber 2 and chamber 3' ($\dot{m}_{a_{23}}$) and radial leak between chamber 3 and chamber 4 ($\dot{m}_{r_{34}}$).

The radial leakage and axial leakage mass flow rates (Figure 7.10) are determined considering the thermodynamic state of the fluid in the two chambers involved. The mass flow model accounts for backflow and limits the mass flow rate to choking conditions. Both the intake and discharge processes consider the instantaneous intake/exhaust port area and pressure ratio to determine the respective mass flow rates. In particular, the intake port model considers at each time-step the actual position of the rotor, which may partially cover the intake port.

As regards the heat transfer model, it has been assumed that the wall temperature distribution does not change with time, regardless of the heat flux. This means that the stator and rotor heat capacity is considerably higher than the working fluid heat capacity. The experimental measurements of Jang et al. [15] found that the temperature

profile along a scroll wrap is almost linear with respect to the involute angle. Based on their results, the scroll wrap temperature Tw has been determined according to:

$$T_w = (T_{in} - T_a) - \frac{T_{in} - T_{out} - T_b}{\varphi_{end}} \varphi, \tag{7.31}$$

where T_{in} is the working fluid inlet temperature, T_{out} is the outlet fluid temperature, φ_{end} is the wrap last point angle and T_a and T_b are model parameters, equal to 10 and 20 respectively.

As regards the convective heat transfer coefficient h, the empirical correlation proposed by Jang et al. [15] has been used. This correlation has been specifically developed to determine the heat transfer in a scroll compressor and it takes into account the total chamber mass flow, the rotor speed and the scroll geometry.

For a given chamber, the heat transfer Q_w is determined by:

$$Q_w = h\left[A_s(T_{ws} - T) + A_r(T_{wr} - T) + A_p\left(T_p - T\right)\right], \tag{7.32}$$

where *T* is the in-chamber fluid temperature, A_s is the stator side wall area, T_{ws} is the stator side wall average temperature. The variables with subscript *r* refer to the rotor side wall, while subscript *p* refers to top and bottom walls. In particular, the top and bottom wall temperature T_p is computed as the area-weighted average temperature of the stator and rotor side wall.

The system of ODE represented by Eq. (7.29) and Eq. (7.30) is time integrated with a first-order accurate Euler method. A time step of 0.001 CAD (which corresponds to 1.67×10^{-7} s at 1000 rpm) has been selected. The initial thermodynamic conditions of the fluid are set to the value of the inlet fluid temperature and pressure. For all cases, six complete rotations ensure the cyclic convergence.

7.3.1 Model validation

The numerical model has been validated by comparing the results in terms of mechanical power output and average intake mass flow rate with experimental data available in the literature [16]. The expander specifications are listed in Table 7.1. Figure 7.11a compares the experimental measurements with the numerical results. The figure shows a very good matching between numerical and experimental results with an almost linear increase of mass flow rate and mechanical power with rpm. Figure 7.11b highlights the influence of the partial overlap between the intake port and the rotor on the chamber pressure for different rotating speeds. The figure shows that this influence is higher as the rotating speed increases, suggesting that the inlet port location has a greater impact on performances as the scroll expander speed increases.

Table 7.1. Scroll expander specifications

Geometry parameters	
a	3.66 mm
s	4.6 mm
Number of chamber pairs	3
Chamber height	40 mm
Radial clearance	0.015 mm
Axial clearance	0.04 mm
Inlet radius	6.5 mm
Inlet center position (x,y)	(-2.17 mm, 2.17 mm)

Thermodynamic parameters	
Fluid	air
Inlet pressure	3.4 bar
Inlet temperature	292.15 K
Outlet pressure	1.013 bar
Outlet temperature	288.2 K

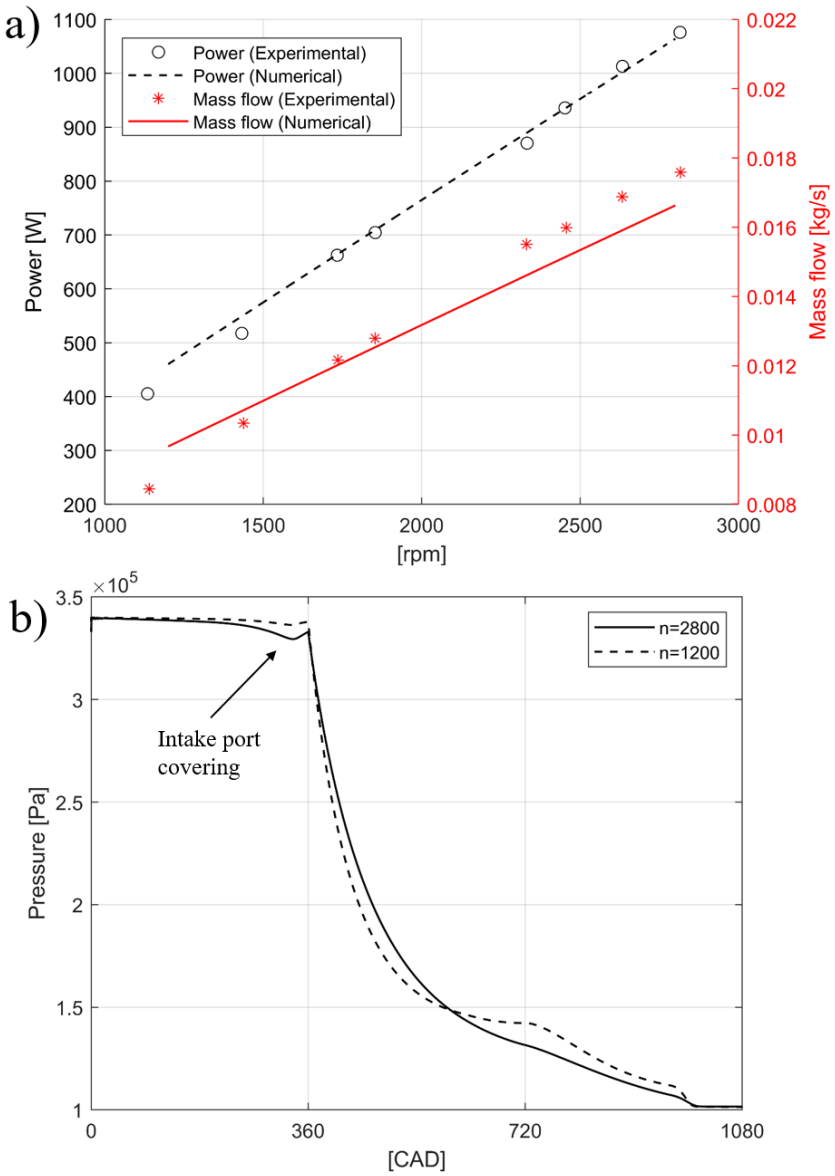

Figure 7.11: Experimental measurements [16] vs numerical results at different rotating speeds (a) and effect of the intake port overlapping on chamber pressure at different speeds (b).

7.4 Influence of the scroll geometry

In order to analyze the influence of the scroll geometry on its performances, the model has been employed to simulate a scroll expander with the geometry specified in Table 7.1 and starting segments obtained with both circular cutter and PMP approaches, setting $\varphi_a = 90°$. Figure 7.12a compares the output mechanical power obtained from the scroll expander and the average mass flow rate as a function of the rotor speed for the two geometries. The figure shows that a higher power and mass flow rate are obtained for the circular cutter geometry with respect to the PMP. In order to compare

the efficiency of the two geometries, the specific work obtained from the expander should be computed. Figure 7.12b compares the specific work of the two geometries, calculated as the ratio between the power output and the mass flow rate at a given rotating speed. The PMP geometry shows a slightly better energy conversion performance at low rotating speeds (below 1500 rpm), while the circular cutter geometry performs better at higher rotating speeds. It should be pointed out that the simulation for the PMP modification has been performed with the same geometry parameters of the circular cutter modification. In particular, the inlet port position and shape may play a significant role on the performances of an expander with PMP geometry, since it determines the inlet mass flow that discharges directly into the second chamber. An appropriate optimization process could improve the performances of an expander with such a modification. In addition, some considerations on the effect of the φ_a angle on the scroll expander with PMP geometry performances have been addressed. This parameter affects the expander performances, not only in terms of output power and mass flow rate (Fig. 3.13a) but also in terms of specific work (Fig. 3.13b). A global optimization of all geometric parameters, including the inlet port shape and location, may significantly improve the expander performances for both geometries.

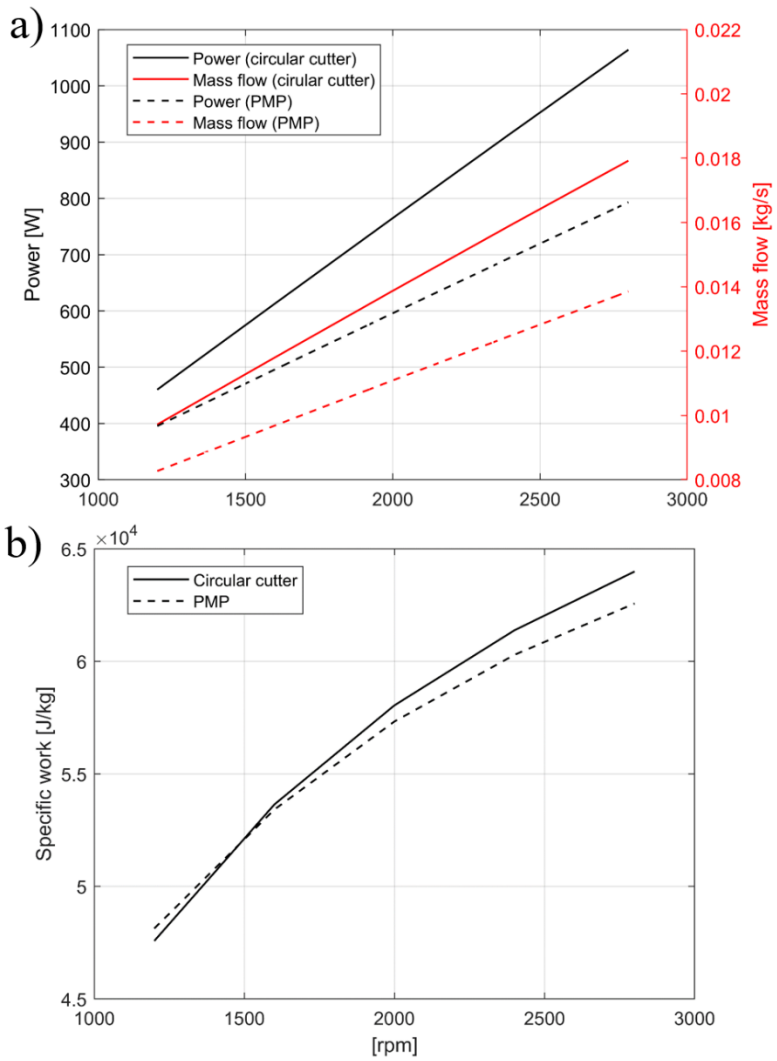

Figure 7.12: Circular cutter vs PMP geometry comparison: power and mass flow vs rotating speed (a) and specific work vs rotating speed (b).

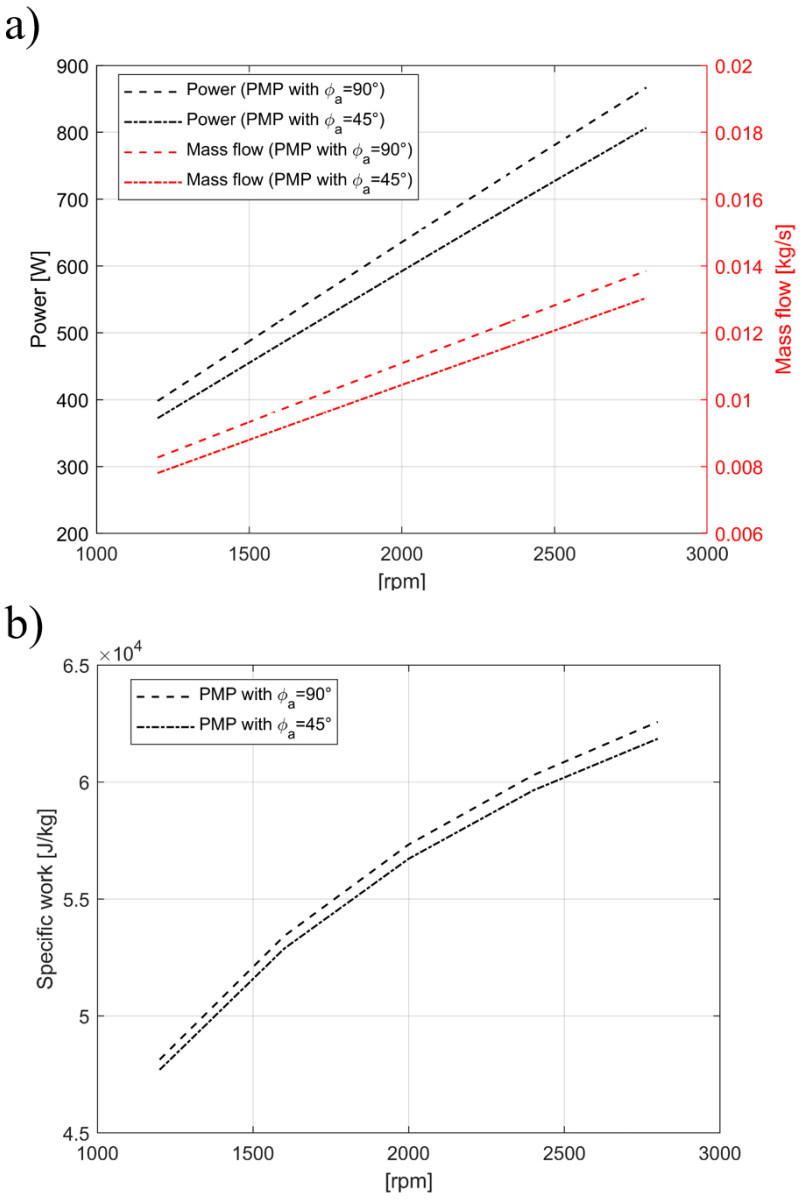

Figure 7.13: Effect of the φ_a angle on expander performances: power and mass flow vs rotating speed (a) and specific work vs rotating speed (b).

7.5 ORC unit modelling

As mentioned in section 7.1, an ORC unit is formed by a pump, a boiler, an expander and a condenser. A model for each component is needed in order to simulate the whole unit.

For the purpose of this work it is not needed to build an accurate model of the pump used in an ORC unit, but only an estimation of the required power is needed, in order to determine the ORC unit thermal efficiency. The power needed by the pump P_p is estimated as:

$$P_p = \dot{m}_f \frac{(h_{2is} - h_1)}{\eta_p}, \tag{7.33}$$

where $\dot{m}_f$ is the working fluid mass flow rate, h_{2is} is the isentropic outlet enthalpy, h_1 is the pump inlet enthalpy and η_p is the pump isentropic efficiency. The input parameters needed by the pump model are:

- Pump inlet pressure (p_1);
- Pump inlet temperature (T_1);
- Pump isentropic efficiency (η_p);
- Pump outlet pressure (p_2).

The pump outlet temperature T_2 is computed using the CoolProp libraires, using as inputs the pump outlet pressure and the pump outlet enthalpy, derived from the pump isentropic efficiency as:

$$h_2 = h_1 + \frac{(h_{2s} - h_1)}{\eta_p}. \tag{7.34}$$

As regards the boiler, the heat exchanger model presented in Chapter 3 will be used. The model assumes that the minimum temperature difference between the hot and cold fluid occurs at the hot side inlet/cold side outlet side. Therefore, the model computes the cold side outlet temperature equal to the hot side inlet temperature minus the user defined ΔT_{pinch}. Then the heat exchanger is divided into 1000 elemental components, in each of which Eqs. (7.17) are solved. If the temperature difference between hot and cold side falls below the defined ΔT_{pinch} in any of the heat exchanger elemental components, the model starts over increasing the temperature difference between the hot side inlet/cold side outlet. This process is repeated until through the whole heat exchanger the temperature difference between hot and cold side is always higher than the defined ΔT_{pinch}. The model has been slightly improved with respect to what presented in Chapter 3 in order to include a pressure drop through the heat exchanger, since in this case the heat exchanger outlet pressure has a greater impact on results.

The scroll expander model, already presented in detail in section 7.2, needs as inputs the inlet temperature and pressure. If properly calibrated, the model is able to predict the mass flow rate and the outlet temperature and pressure.

The condenser will not be modelled, since it is assumed that the heat transfer surface and the cooling fluid mass flow rate is always sufficient to take the working fluid to the pump inlet temperature.

7.5.1 Model validation

The experimental results obtained by *Feng et al* [17] have been taken as reference to calibrate the ORC unit model. The experimental setup has a nominal power of 10 kW

and uses the R245fa as working fluid. The working fluid is pressurized by a centrifugal pump, while the thermal energy is provided by a conductive oil, which receives energy from three electric heaters and transfers it to the working fluid through a plate heat exchanger. The scroll expander used was modified from a commercial oil-free scroll type air compressor, and its geometric parameters are listed in Table 7.2.

Table 7.2. Scroll expander specifications

Scroll Expander Geometry	
a	4.456 mm
s	4.6 mm
Number of chamber pairs	3
Built-in volumes ratio	2.95
Chamber height	48.2 mm

Feng et al. have provided the experimental measurements of a few working points of the ORC unit at different loads and speeds, which are listed in Table 7.3.

Table 7.3. ORC unit experimental data [17].

	Working points				
	1	2	3	4	5
Mass flow rate [kg/s]	0.1534	0.1931	0.2354	0.2689	0.1012
Expander power output [kW]	1.796	2.369	2.918	3.258	0.998
Expander speed [rpm]	2321	2526	2700	2799	1935
Pump shaft power [kW]	0.414	0.547	0.643	0.720	0.271
P1 [bar]	1.88	1.94	2.01	2.09	2.03
P2 [bar]	6.21	7.54	8.78	9.73	4.82
P3 [bar]	5.80	6.99	8.25	9.11	4.56
P4 [bar]	1.93	2.08	2.26	2.41	2.02
T1 [K]	294.0	295.1	296.1	297.6	296.1
T2 [K]	296.0	297.1	298.1	299.5	298.1
T3 [K]	347.3	355.1	362.6	366.0	337.4
T4 [K]	326.6	332.5	338.6	341.2	321.0

Hot fluid inlet temperature [K]	353.2	362.5	371.5	377.4	341.7

From the experimental data it has been possible to estimate an average value for the ΔT at the heat exchanger hot side inlet/cold side outlet, which has been set to 6 K, and the pump isentropic efficiency η_p as a function of the pump mass flow rate, which, as shown in Figure 7.14 can be approximated by a quadratic equation as follows:

$$\eta_p = -1.313\dot{m}_f{}^2 + 1.263\dot{m}_f - 0.040 \,. \tag{7.35}$$

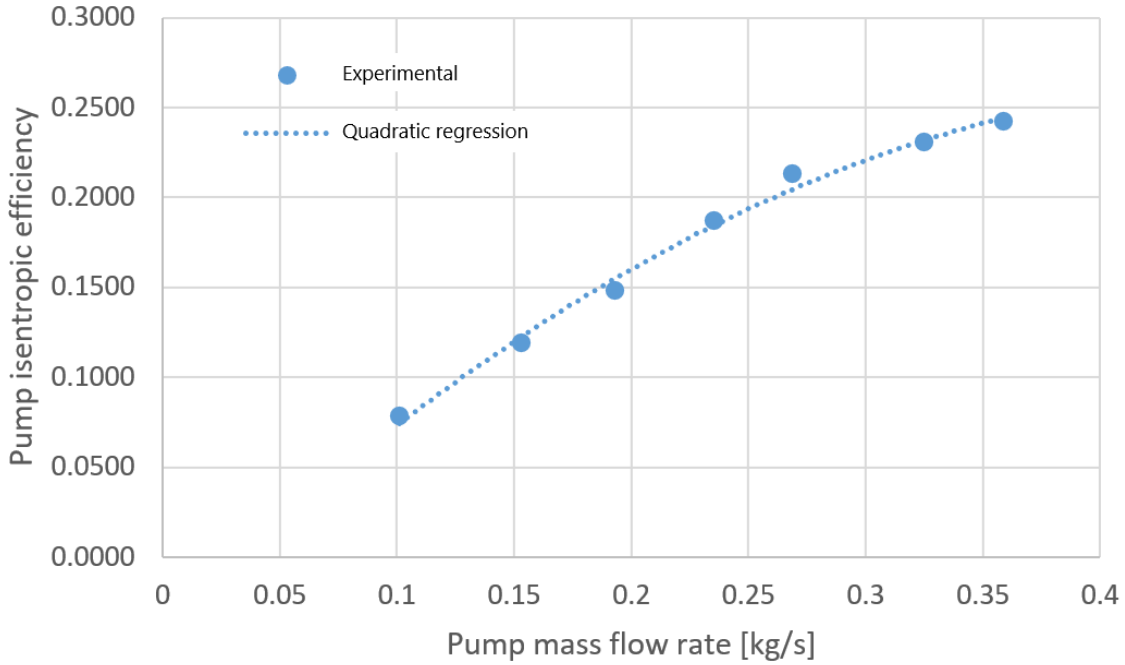

Figure 7.14: Pump isentropic efficiency as a function of mass flow rate: experimental [17] vs quadratic regression.

The other parameters needed by the model are represented by the inlet diameter and position, and the axial and radial clearance. After a parametric analysis, the inlet diameter has been set to 5 mm, while the axial and radial clearance have been set to 0.14 mm and 0.2 mm respectively.

Regarding the scroll expander wall heat transfer model, during the model calibration process it has been necessary to modify the parameters T_a and T_b in Eq. (7.31). Both have been set equal to 5.

As shown in Table 7.4, the numerical model provides a very accurate approximation of the experimental data at all working points tested. The highest discrepancies are found on the mass flow rate, where the relative error is as high as 14.78%. Considering the low absolute value of the mass flow rate, we can consider the relative error satisfactory.

Table 7.4. ORC unit experimental data [17] versus numerical model outputs.

	Working points

	1	2	3	4	5
Experimental mass flow rate [kg/s]	**0.153**	**0.193**	**0.235**	**0.269**	**0.101**
Numerical mass flow rate [kg/s]	0.154 (+0.24%)	0.188 (-2.66%)	0.219 (-6.86%)	0.243 (-9.66%)	0.116 (-14.78%)
Experimental expander power output [kW]	**1.796**	**2.369**	**2.918**	**3.258**	**0.998**
Numerical expander power output [kW]	1.771 (-1.40%)	2.415 (+1.93%)	3.005 (+2.96%)	3.442 (+5.64%)	0.951 (-4.71%)
Experimental pump shaft power [kW]	**0.414**	**0.547**	**0.643**	**0.720**	**0.271**
Numerical pump shaft power [kW]	0.398 (-3.9%)	0.517 (-5.48%)	0.639 (-0.62%)	0.748 (+3.80%)	0.283 (+4.43%)
P3 experimental [bar]	**5.80**	**6.99**	**8.25**	**9.11**	**4.56**
P3 numerical [bar]	5.84 (+0.58%)	7.09 (+1.35%)	8.25 (+0.03%)	9.15 (+0.34%)	4.53 (-0.74%)
T2 experimental [K]	**296.0**	**297.1**	**298.1**	**299.5**	**298.2**
T2 numerical [K]	295.9 (-0.03%)	297.0 (-0.03%)	298.0 (-0.02%)	299.5 (+0.01%)	298.4 (+0.04%)
T3 experimental [K]	**347.3**	**355.1**	**362.6**	**366.0**	**337.4**
T3 numerical [K]	347.2 (-0.02%)	356.5 (+0.39%)	365.5 (+0.79%)	371.4 (+1.47%)	335.7 (-0.51%)
T4 experimental [K]	**326.6**	**332.5**	**338.6**	**341.2**	**321.0**
T4 numerical [K]	327.0 (+0.12%)	328.18 (-1.29%)	329.7 (-2.61%)	330.7 (-3.07%)	326.02 (+1.57%)

The in-chamber pressure and temperature through the scroll expander for working point 1 are reported in Figure 7.15 and Figure 7.16, respectively. It can be noticed that both the in-chamber pressure and the temperature in the scroll expander final chamber match the experimental expander outlet pressure and temperature. Figure 7.17 shows the heat exchanger temperature profiles and the computed heat transfer area, which is equal to 16.74 m^2 and closely matches the value of 16.18 m^2 of the experimental setup.

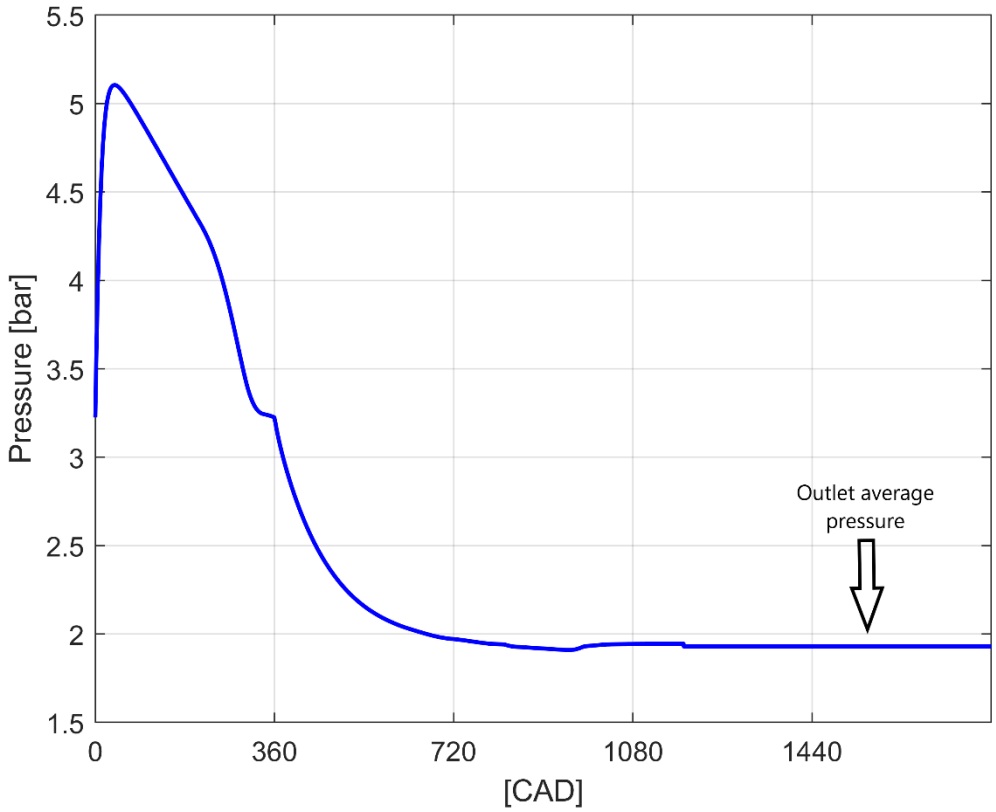

Figure 7.15: Working point 1 scroll expander in-chamber pressure.

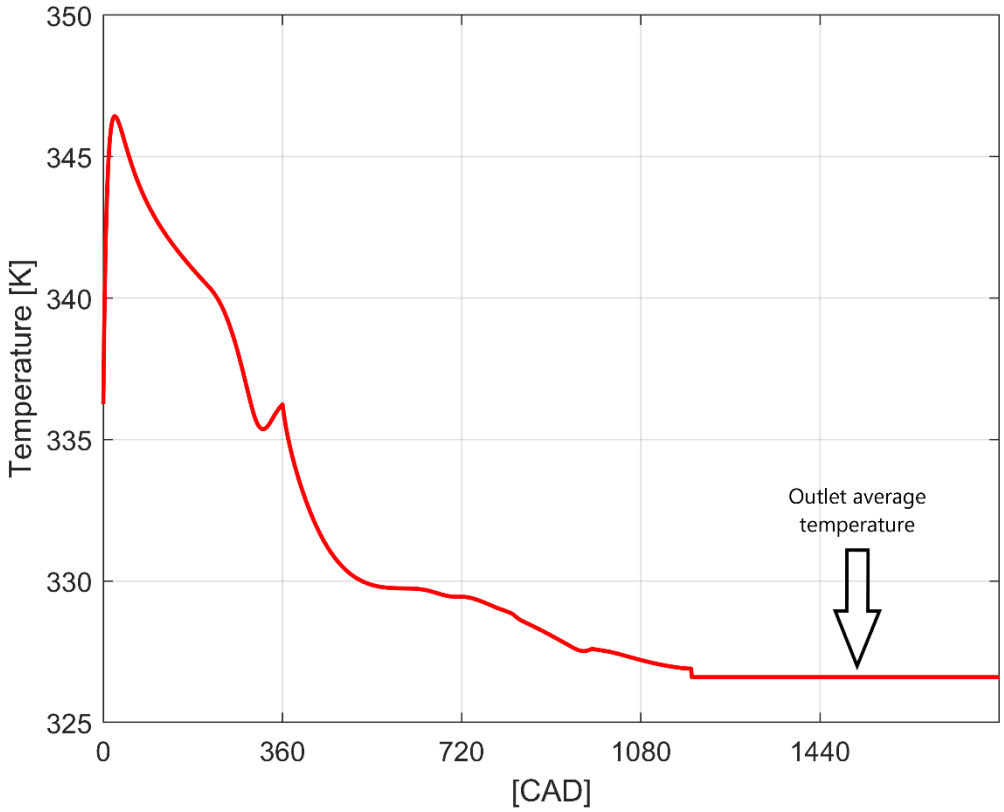

Figure 7.16: Working point 1 scroll expander in-chamber temperature.

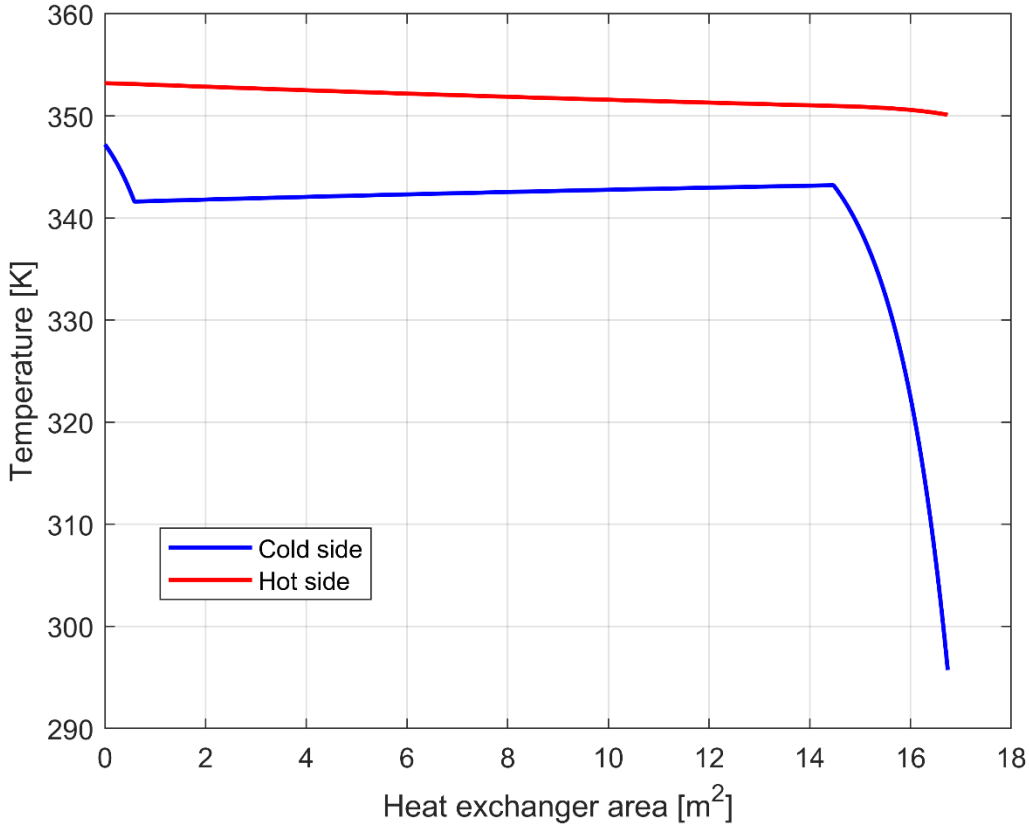

Figure 7.17: Working point 1 heat exchanger temperature profiles (left side = cold fluid outlet / hot fluid inlet).

7.6 Internal combustion engine–ORC coupling

The ORC model presented has been used to determine the amount of exhaust energy recoverable from an internal combustion engine. As regards the internal combustion engine, the same engine used for the quasi-dimensional simulations in chapter 3 will be used as reference. The internal combustion engine 0-D model has already been calibrated on experimental data [18], therefore the exhaust gases mass flow rate and energy can be used as input for the ORC quasi-dimensional model. In particular, the mean exhaust mass flow rate is equal to 2.94×10^{-3} kg/s, while the overall exhaust energy has been decreased by 20%, which represents the thermal losses through the manifolds between the exhaust port and the heat exchanger inlet and the energy losses through the heat exchanger. The exhaust gases temperature has been computed through the first law of thermodynamics, considering the exhaust gases chemical composition and energy. The resulting temperature is equal to 977 K. The exhaust gases composition is reported in Table 7.5.

The ORC heat exchanger model, with the provided exhaust gases data, is able to compute the working fluid temperature at the scroll expander inlet, which allows to calculate the heat extracted from the exhaust gases. The scroll expander model will then be used to determine the power output and, consequently, the ORC efficiency, ε_{ORC}, defined as:

$$\varepsilon_{ORC} = \frac{P_{exp} - P_p}{\dot{Q}_{in}}, \tag{7.36}$$

where P_{exp} is the expander power output, P_p is the power required by the pump and $\dot{Q}_{in}$ is the heat recovered from the exhaust gases.

Table 7.5. Reference engine [18] exhaust gases thermodynamic properties and composition (data from WISE code, Chapter 3).

ICE exhaust gases thermodynamic properties	
Exhaust gases temperature [K]	977
Exhaust gases pressure [bar]	1.05
Exhaust gases mass flow rate [kg/s]	2.94e-3
N_2 mass fraction	0.796
CO_2 mass fraction	0.140
H_2O mass fraction	0.064

The ORC unit used for the model validation [17] is designed for a nominal power of 10 kW. The reference engine [18] exhaust gases provide a much lower power input. Particularly, bringing the exhaust gases temperature to ambient temperature (i.e. 298 K) it is possible to extract about 2.75 kW per engine cylinder. From experimental data, in order to obtain a power output of 1.8 kW from the scroll expander, a power input of 34 kW was necessary (working point 1). Therefore, it is clear that the heat input provided by a single engine cylinder is not sufficient to the ORC unit. In order to overcome this issue, it has been assumed that the exhaust gases of several cylinders working in parallel are provided to the ORC unit. In particular acceptable working conditions are achieved with a 8-cylinders setup. This means that the heat exchanger hot-side mass flow rate is 8 times higher than what listed in Table 7.5, while the exhaust gases temperature, pressure and mass fractions remain unchanged.

The working fluid mass flow rate has been set to the value of 0.04 kg/s in order to maximize the heat transfer with exhaust gases. The pump outlet pressure has then been adjusted in order to have the same mass flow rate of 0.04 kg/s through the scroll expander. The ORC model input parameters and outputs are listed in Table 7.6.

Table 7.6. ORC unit-ICE coupling (8-cylinders engine) inputs and outputs.

Input parameters	
Exhaust gases mass flow rate [kg/s]	2.352×10^{-2}
Exhaust gases temperature [K]	977
Exhaust gases pressure [bar]	1.05
Working fluid mass flow rate [kg/s]	0.04
Pump inlet pressure [bar]	1.89
Pump inlet temperature [K]	294
Pump outlet pressure [bar]	2.9
Scroll outlet temperature [K]	450.6
Scroll outlet pressure [bar]	1.98
Scroll speed [rpm]	1000
Outputs	
Pump outlet temperature [K]	294.8
Scroll expander inlet temperature [K]	500
Expander power output [kW]	0.33
Pump shaft power [kW]	0.02
Heat input [kW]	18
ε_{ORC}	0.02

Figure 7.18 shows the temperature profile into the heat exchanger for the hot and cold fluid. A heat exchanger surface of 15.7 m^2 is needed, which is in line with the experimental setup. Figures 7.19 and 7.20 show the scroll expander in-chamber pressure and temperature respectively. Due to the low speed of the scroll expander, the effect of the inlet port covering is clearly visible in the pressure profile.

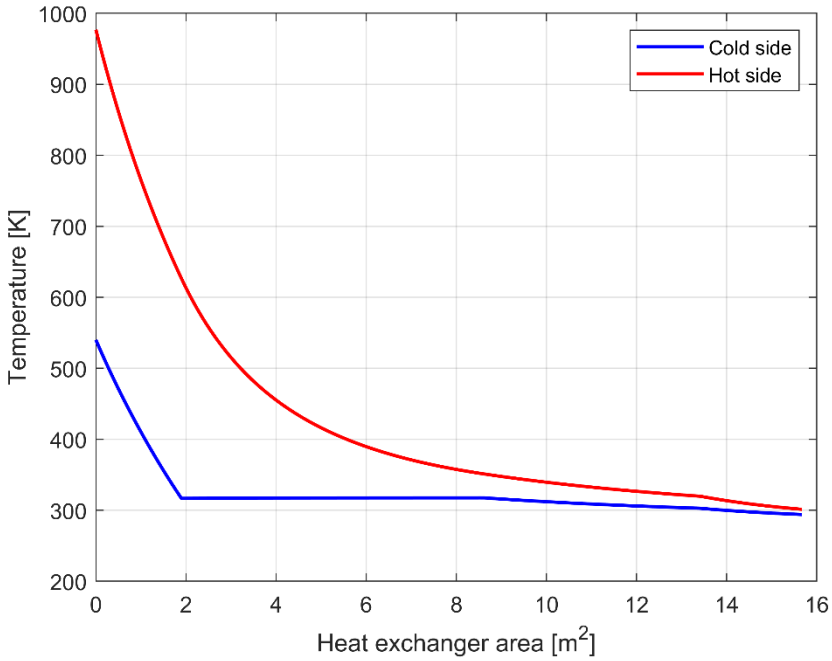

Figure 7.18: 8-cylinders engine heat exchanger temperature profiles (left side = cold fluid outlet / hot fluid inlet).

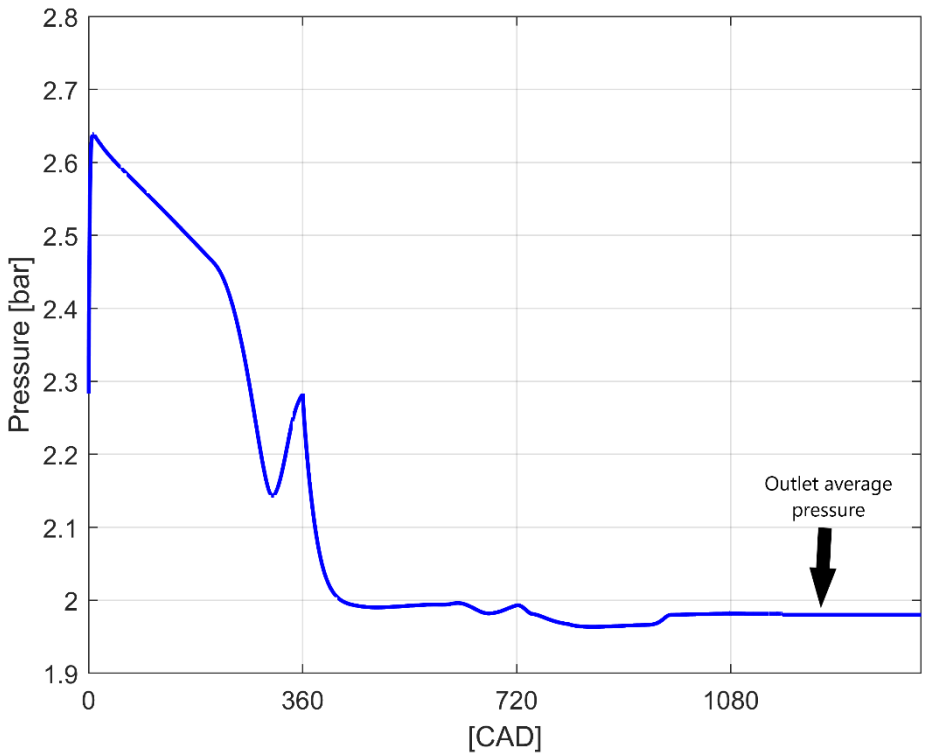

Figure 7.19: 8-cylinders engine scroll expander in-chamber pressure.

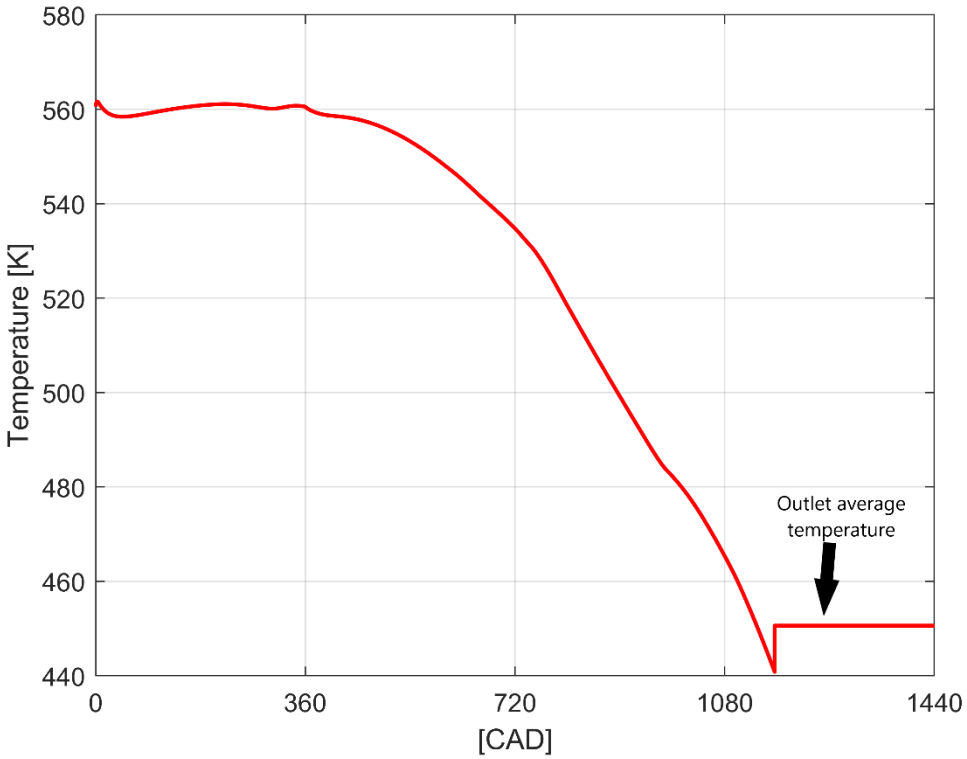

Figure 7.20: 8-cylinders engine scroll expander in-chamber temperature.

From Table 7.6 stands out the very low ORC energy conversion efficiency, equal to 0.02, meaning that only 2% of the input heat is converted into useful work. Waste heat recovery is characterized by a low efficiency, as a consequence of the second law of thermodynamics, but in this case the efficiency is particularly low due to the low exhaust gases mass flow rate, which makes impossible to increase the scroll expander input pressure, in order to limit the working fluid mass flow rate through the ORC unit. As stated before, the low efficiency is caused by the size of the ORC unit, which is designed to work with higher energy inputs.

In order to check the performances of the ORC unit with a more appropriate power input, a further simulation has been performed assuming the use of a 16 cylinders engine. Table 7.7 shows the inputs provided to the ORC model and the outputs obtained. The higher heat input improves the ORC efficiency by 50%. Therefore, it is clear that, in order to improve the ORC efficiency, it is crucial to provide an appropriate heat input, which makes the ORC energy recovery applied to internal combustion engines particularly suitable for stationary applications.

Table 7.7. ORC unit-ICE coupling (16-cylinders engine) inputs and outputs.

Input parameters	
Exhaust gases mass flow rate [kg/s]	4.704e-2
Exhaust gases temperature [K]	977
Exhaust gases pressure [bar]	1.05
Working fluid mass flow rate [kg/s]	0.09
Pump inlet pressure [bar]	1.89
Pump inlet temperature [K]	294
Pump outlet pressure [bar]	1.98
Scroll outlet temperature [K]	460
Scroll outlet pressure [bar]	1.98
Scroll speed [rpm]	1800
Outputs	
Pump outlet temperature [K]	295.1
Scroll expander inlet temperature [K]	500
Expander power output [kW]	1.22
Pump shaft power [kW]	0.135
Heat input [kW]	36.4
ε_{ORC}	0.03

Nomenclature

ORCs: Organic Rankine Cycles

CAD: Crank Angle Degree

WISE: Water Injection Spark Engine

ICE: Internal Combustion Engine

References

[1] F. Campana, M. Bianchi, L. Branchini, A. De Pascale, A. Peretto, M. Baresi, A. Fermi, N. Rossetti, R. Vescovo. "ORC waste heat recovery in European energy intensive industries: Energy and GHG savings." Energy Conversion and Management 76, (2013): 244-252, doi: 10.1016/j.enconman.2013.07.041

[2] A. Mahmoudi, M. Fazli, M. R. Morad. "A recent review of waste heat recovery by Organic Rankine Cycle." Applied Thermal Engineering 143 (2018): 660-675, doi: 10.1016/j.applthermaleng.2018.07.136

[3] A. Auld, A. Berson, S. Hogg. "Organic Rankine cycles in waste heat recovery: a comparative study." International journal of low-carbon technologies 8 .suppl_1 (2013): i9-i18, doi: 10.1093/ijlct/ctt033

[4] Z. Varga, I. Rabi, C. Farkas. "Waste heat recovery with organic Rankine cycle in the petroleum industry." Chem Eng 29 (2012), doi: 10.3303/CET1229051

[5] M. Bianchi, A. De Pascale. "Bottoming cycles for electric energy generation: parametric investigation of available and innovative solutions for the exploitation of low and medium temperature heat sources." Applied Energy 88.5 (2011): 1500-1509, doi: 10.1016/j.apenergy.2010.11.013

[6] F. Alshammari, M. Usman, A. Pesyridis. "Expanders for Organic Rankine Cycle Technology." Organic Rankine Cycle Technology for Heat Recovery (2018): 41, doi: 10.5772/intechopen.78720

[7] S. Emhardt, G. Tian, J. Chew. "A review of scroll expander geometries and their performance." Applied Thermal Engineering 141 (2018): 1020-1034, doi: 10.1016/j.applthermaleng.2018.06.045

[8] J. Bao, L. Zhao. "A review of working fluid and expander selections for organic Rankine cycle." Renewable and sustainable energy reviews 24 (2013): 325-342, doi: 10.1016/j.rser.2013.03.040

[9] Z. Jiang, D. K. Harrison, K. Cheng. "Computer-aided design and manufacturing of scroll compressors." Journal of Materials Processing Technology 138.1-3 (2003): 145-151, doi: 10.1016/S0924-0136(03)00063-3

[10] Z. Ma, H. Bao, A. P. Roskilly. "Dynamic modelling and experimental validation of scroll expander for small scale power generation system." Applied energy 186 (2017): 262-281, doi: 10.1016/j.apenergy.2016.08.025

[11] J. Yang, Z. Sun, B. Yu, J. Chen, "Modeling and optimization criteria of scroll expander integrated into organic Rankine cycle for comparison of R1233zd (E) as an alternative to R245fa." Applied Thermal Engineering 141 (2018): 386-393, doi: 10.1016/j.applthermaleng.2018.06.001

[12] X. Zhang, Y. Xu, J. Xu, Y. Sheng, Z. Zuo, J. Liu, H. Chen, Y. Wang, Y. Huang, "Study on the performance and optimization of a scroll expander driven by compressed air." Applied Energy 186 (2017): 347-358, doi: 10.1016/j.apenergy.2016.06.004

[13] K. Jang, S. Jeong. "Experimental investigation on convective heat transfer mechanism in a scroll compressor." International Journal of Refrigeration 29.5 (2006): 744-753, doi: 10.1016/j.ijrefrig.2005.12.002

[14] I. H. Bell, J. Wronski, S. Quoilin, V. Lemort, "Pure and pseudo-pure fluid thermophysical property evaluation and the open-source thermophysical property library CoolProp." Industrial & engineering chemistry research 53.6 (2014): 2498-2508, doi: 10.1021/ie4033999

[15] K. Jang, S. Jeong. "Experimental investigation on convective heat transfer mechanism in a scroll compressor." International Journal of Refrigeration 29.5 (2006): 744-753, doi: 10.1016/j.ijrefrig.2005.12.002

[16] L. Guangbin, Z. Yuanyang, L. Liansheng, S. Pengcheng, "Simulation and experiment research on wide ranging working process of scroll expander driven by compressed air." Applied Thermal Engineering 30.14-15 (2010): 2073-2079, doi: 10.1016/j.applthermaleng.2010.05.015

[17] Feng, Yong-qiang, et al. "Experimental investigation of a R245fa-based organic Rankine cycle adapting two operation strategies: Stand alone and grid connect." Energy 141 (2017): 1239-1253, doi: 10.1016/j.energy.2017.09.119

[18] D'Errico, G., Lucchini, T., Onorati, A., Mehl, M., Faravelli, T., Ranzi, E., ... & Vaglieco, B. M. (2007). *Development and experimental validation of a combustion model with detailed chemistry for knock predictions* (No. 2007-01-0938). SAE Technical Paper. Doi: 10.4271/2007-01-0938

Part III

Conclusions

The application of energy recovery techniques on fluid machinery can have a significant influence on their efficiency, therefore reducing pollutant emissions and energy consumption. Finding a suitable technique for the specific machine working conditions is crucial to achieve an efficient and feasible energy recovery. Specifically, two main factors need to be taken into account: the amount and quality of recoverable waste heat and the size of the additional components needed to achieve energy recovery. As for the two energy recovery approaches described in this work, the internal combustion engine supercritical water direct injection technique is especially suited for on-vehicle applications, whereas fitting an Organic Rankine Cycle (ORC) plant may be challenging. On the contrary, for stationary applications and very large engines, the Organic Rankine Cycles may be preferred. It should also be mentioned that the two energy recovery approaches can be used jointly. This could further improve the energy recovery efficiency.

One of the main limits to waste heat recovery is the lack of viable options to use the recovered waste heat. The Organic Rankine Cycle approach converts the recovered energy in a mechanical power output, which is often converted in electrical energy. This approach is very appealing for large waste-heat and continuous processes, where the electrical power can be reused or fed into the public electrical grid (open loop energy recovery). On the other end, if the process is discontinuous and the power output is relatively low, it may be not practical to reuse the recovered energy in the form of electrical energy, or it may not even be possible to reuse it where the machine is, due to the lack of a connection to the public electrical grid or the lack of a device that needs electrical power. In this case the internal combustion engine supercritical water direct injection is a better approach, since it increases the machine efficiency without the need of any external user or connection (closed loop energy recovery).

The internal combustion engine supercritical water direct injection is an innovative energy recovery approach, which still requires an extensive experimental validation. The CFD analysis presented is meant to give a first understanding of the potential benefits obtainable and the relative importance of the various injection parameters. Nonetheless many technical challenges need to be addressed, such as the feasibility of the supercritical water injector, the size of the water tank, the heat exchanger and the condenser. Specifically, the supercritical water injector needs to be able to operate with

a fluid at a much higher temperature than conventional injectors. Furthermore, the supercritical water into the injector will unlikely provide a sufficient lubrication of the injector pintle. Regarding the heat exchanger, water tank, and condenser, their size is very important, particularly for on-vehicle applications, where the available space may limit their dimensions, leading to a lower achievable energy recovery. Besides these technical issues that need to be addressed, the supercritical water direct injection energy recovery approach may boost by more than 10% the internal combustion engines efficiency, resulting in both lower emissions and fuel consumption. In addition, the numerical model, in addition to the higher engine efficiency, also predicts lower emissions, which is a further benefit of this energy recovery technology. Finally, the injected water may also permit a higher engine compression ratio, due to the water anti-knocking properties.

The CFD modelling of supercritical water injection-flame front interaction, with proper injection timing, has consistently returned a higher combustion speed, which is often a desired characteristic. This approach could therefore be transferred to other applications, where a higher combustion speed is convenient. However, this aspect should be further investigated, with the help of experimental measurements.

One of the main drawbacks of the internal combustion engines supercritical water direct injection is the substantial increase of wall heat transfer, which increases the engine losses. This aspect needs to be further explored, with the help of an experimental campaign, in order to validate the RANS modelling of supersonic jets heat transfer. Furthermore, the injection parameters (i.e. injection pressure, temperature and duration) have a great effect on wall heat transfer, and a specific optimization should be performed in order to minimize these losses. In addition, the injector geometry together with the piston and head geometries also play a fundamental role in the overall wall heat transfer. Therefore, the optimization of the overall energy recovery technologies should also take these aspects into account.

As regards the Organic Rankine Cycle modelling, it is a well-known technology, which has been widely studied and optimized in recent years. In this work particular focus has been put on the scroll expander, which is one of the components that has the greatest impact on efficiency. The scroll expander model, together with the pumps, and heat exchanger model, has been used to estimate the ORC efficiency at different working points. Specifically, the ORC model returns an energy recovery efficiency of 2%, using as energy source the exhaust gases of an 8-cylinder internal combustion engine, while the energy recovery efficiency reaches 3% when using as energy source the exhaust gases of a 16-cylinder internal combustion engine. Nonetheless, the main characteristic of the scroll expander model is the possibility of detecting the inlet port covering by the rotor during its orbiting motion. In this way it is possible to calculate the real inlet port area at each crank angle. This characteristic can be exploited to perform an optimization of the inlet port geometry, which would increase the expander efficiency for a given inlet port area.